# Coupling by volume conduction as a wireless power transfer and communications method for threadlike biomedical implants

Marc Tudela Pi

TESI DOCTORAL UPF / 2022

Thesis supervisors

Dr. Antoni Ivorra Cano
Dra. Laura Becerra Fajardo

Department of Information and Communication Technologies

Universitat Pompeu Fabra Barcelona

The work presented within this thesis is part of a project that has received funding from the European Research Council (ERC) under the European Union's Horizon 2020 research and innovation programme (grant agreement No. 724244)

*Al meu padrí*

# Acknowledgements

This research has benefited from the direct and indirect contribution of great many people. I want to express here my gratitude to all the people whom without this work would have not been possible.

First and foremost, I would like to thank my supervisors Dr. Antoni Ivorra and Dr. Laura Becerra for all their guidance and advice with this Ph.D. Their deep knowledge and long-standing experience have encouraged me in all the time of my academic research. I am grateful for your intellectual guidance, suggestions, feedback, and criticism all along this professional path. I am equally grateful for being so supportive, encouraging, and empathic, both professionally and personally.

I would like to offer my special thanks to all my colleagues from the Biomedical Electronics Research Group (BERG), friends, lab mates and colleagues, Aracelys, Albert, Quim, Enric, Borja and Nerea. This work owes much to their interesting ideas and amusing talks. Additionally, I would like to express gratitude to Jesús Minguillon for his absolute support and for taking the time of discussing with me almost all my research questions.

This work has also allowed me to meet a lot of people who have influenced my professional and daily life. I am deeply grateful to Shahid and Ivano, who have both become my great friends. I would like to extend my sincere thanks to my friends Gisela and Oriol, who cheered me and shared happy moments with me.

Lastly, I would be remiss in not mentioning my family, especially my parents and grandparents. Their belief in me kept my motivation and strength during this process. I cannot express with words all my gratitude to my couple Aida, for her unwavering support and unconditional help from the very start.

# Abstract

Although the use of volumetric conduction to power wireless implants has been experimentally validated in recent years, a theoretical framework to determine the power and efficiency obtained by minimally invasive implants has not been established yet. This thesis aims to develop and validate these models. Firstly, an analytical model is presented to determine the maximum power an implant can locally obtain using volume conduction. It was expanded to model the complete transmission link by using a multiport network and was fitted using parameters obtained from human MRI images. Finally, the provided model is rearranged to model communications based on volume conduction. The results demonstrate that powers of mW can be obtained using submillimetric electrodes if they are spaced a few centimeters apart (> 2 cm). Therefore, this thesis contributes to establishing the theoretical framework of volume conduction and paved the development of new minimally invasive implants.

# Resum

Tot i que en els darrers anys l'ús de la conducció volumètrica per alimentar implants sense fils s'ha validat experimentalment, encara no s'ha establert un marc teòric que permeti determinar la potència i l'eficiència obtinguda en implants mínimament invasius. Per aquest motiu, en aquesta tesi es desenvolupen i es validen un conjunt de models teòrics que estableixen les bases del mètode descrit. En primer lloc, es parteix d'un model analític que permet determinar la potència màxima que un implant pot assolir mitjançant la conducció volumètrica quan un camp elèctric uniforme hi és present. Seguidament, aquest model s'amplia en modelar l'enllaç de transmissió comprés entre el sistema extern i els implants mitjançant una xarxa multiports. En aquesta tesi, també se'n descriu el procés de validació, així com el procediment seguit per obtenir els paràmetres de la xarxa multiports a partir d'imatges de ressonància magnètica i simulacions d'elements finits. Finalment, es presenta un circuit de comunicacions passiu i s'adapta el model introduït prèviament per descriure el comportament d'aquest nou circuit. Els resultats obtinguts mostren que a partir de l'ús d'elèctrodes submil·limètrics es poden obtenir potències de diversos mil·liwatts, sempre que aquests elèctrodes estiguin separats diversos centímetres (> 2 cm). Aquesta tesi contribueix a establir el marc teòric de l'ús de l'acoblament de la conducció volumètrica com a mètode per alimentar i comunicar-se amb implants mínimament invasius.

# Contents

# Acronyms and abbreviations

| | |
|---|---|
| ac | Alternating current |
| AIMD | Active implantable medical device |
| ASK | Amplitude-shift keying |
| dc | Direct current |
| EMG | Electromyography |
| HF | High frequency |
| IBC | Intrabody communication |
| ICNIRP | International commission on non-ionizing radiation protection |
| IEEE | Institute of electrical and electronics engineers |
| FEM | Finite element methods |
| MPE | Maximum permissible exposure |
| MRI | Magnetic resonance imaging |
| NFIC | Near field inductive coupling |
| NFCC | Near field capacitive coupling |
| PCB | Printed circuit board |
| PDL | Power delivered to the load |
| PTE | Power transmission efficiency |
| RF | Radiofrequency |
| RMS | Root mean square |
| RX | Receiver |
| SAR | Specific absorption rate |
| TX | Transmitter |
| WPT | Wireless power transfer |

# List of figures

# List of tables

# CHAPTER 1

## INTRODUCTION

## 1.1 Introduction

From the appearance of the first fully implantable pacemaker in 1958 [1] until the last years, the evolution of active implantable medical devices (AIMDs) has been closely related to the evolution of electronics. Advances in recent decades have allowed the integration of most of the implant electronics into tiny silicon chips [2]. This size reduction has favored the development of a multitude of biomedical implants such as deep brain stimulators [3], cochlear and retinal implants [4], [5], drug infusion pumps [6], implantable pressure sensors [7], and peripheral nerve stimulators [8]. Despite the reduction in size over the last decades, most of the current AIMDs remain bulky [9]. This implies, on the one hand, that their implantation requires long and complex surgical operations. On the other hand, the risk of suffering complications associated with having an external device implanted inside the body is closely related to the size of the AIMD. Bulky devices are more likely to trigger an adverse immune response and are also more prone to infection [10], [11]. In order to reduce the possible adverse side effects and risks associated with implanting the current AIMDs, it has been suggested to continue reducing their size to develop what has been referred to as active injectable medical devices [12], [13]. Unlike most current AIMDs, these devices would not require open surgery but would be deployed employing percutaneous injections [9]. Nowadays, the main factor hindering the miniaturization of AIMDs is the size of the powering components of the AIMDs, since these parts are bulkier than the electronics they feed [14].

The power consumption of biomedical implants can vary in many orders of magnitude depending on their application and functionality. For example, while state-of-the-art pacemakers have one of the lowest consumptions, around 5-10 μW [15], a retinal prosthesis requires approximately 45 mW [16], and to produce muscle stimulation powers of 1-10 mW are required [17]. Submillimetric implants cannot obtain these powers based on conventional powering technologies, i.e., using batteries or wireless power transfer (WPT) by inductive coupling [2]. This can be explained as, in the former,

modern battery technologies offer too low energy densities [18], and in the later, inductive coupling requires wide and rigid coils. Theoretically, it is challenging to conceive scenarios, where a submillimeter coil placed several millimeters inside the tissues may obtain powers of milliwatts [19].

In recent years, novel WPT and energy scavenging or harvesting methods have been proposed to overcome the limitations of current powering technologies. One of these methods that can become more suitable to feed networks of microimplants due to its inherent characteristics is volume conduction. Although we have recently shown *in vivo* that coupling based on volume conduction can be an effective power transfer method for injectable AIMDs [20], the use of volume conduction for powering deeply implanted devices has remained almost inexistent until the last years, and the theoretical basis that sustains its use has not yet been established.

## 1.2 Research goal

The main goal of this thesis is to establish and validate a theoretical framework for coupling based on volume conduction as a WPT method and communications method, particularly for threadlike biomedical implants. To do so, this thesis aims to develop a set of analytical and numerical models to describe this method.

This thesis also aims to describe in detail the procedure required to obtain the model parameters.

Finally, the last objective is to analytically model communications based on load modulation and coupling by volume conduction and study the feasibility of using this method for both powering and communicating with biomedical implants.

It is expected that the obtained models will precisely identify the main parameters involved with volume conduction. This would facilitate the design and sizing of new threadlike biomedical implants.

## 1.3 Dissertation outline

Chapter 2 describes the main WPT methods for powering biomedical implants and introduces and describes coupling by volume conduction.

Chapter 3 presents a set of reception analytical models capable of determining the maximum ac and dc power a thin and elongated implant can receive by using volume conduction as a WPT method. This chapter also includes the *in vitro* validation of the obtained models.

Chapter 4 extends the previous model by introducing a multiport model for the entire transmission link (i.e., the external electrodes, the implant electrodes, and the tissues encompassed between them). This model is numerically validated by using a parametric analysis.

Chapter 5 describes the procedure for determining the values of the multiport model using MRI images obtained from human participants and compares the numerical results with experimental data. It also describes the validation of volume conduction as a WPT method to power digital implants in humans.

Chapter 6 analytically studies the use of a passive communication method, the load modulation, based on volume conduction for thin and elongated implants. The proposed method is validated using a demonstrative communication circuit.

Finally, Chapter 7 summarizes the main conclusions that can be extracted from this thesis and discusses the future directions concerning the research done.

# CHAPTER 2

## BACKGROUND

## 2.1 Power methods

Due to the heterogeny of biomedical implant applications, there are several implant powering system methods. For instance, the primary power method for critical applications (e.g., pacemakers) is still the use of batteries. To minimize the size of the implants in non-critical applications and avoid the use of bulky batteries, energy scavengers or WPT methods are used. Therefore, the selection of a particular powering method depends on different parameters related to the application (e.g., maximum power requirements, implantation depth, or power transmission efficiency). The following subsection describes the most used methods for powering biomedical implants. This section has been sorted into intrinsic methods (batteries and energy scavengers) and WPT methods (inductive coupling, ultrasonic coupling, and coupling based on volume conduction).

### 2.1.1 *Intrinsic methods*

#### *2.1.1.1 Batteries*

Batteries are a reliable and autonomous method to power AIMDs with low power requirements. Due to these characteristics, batteries are still the most used method to power life-critical applications (e.g., pacemakers).

The first electrochemical batteries introduced in the 1960s to power supply pacemakers were mercury-zinc batteries. Unfortunately, they had a limited duration of approximately two years [1] and an energy density close to 0.2 $Wh/cm^3$ [21]. Therefore, patients had to undergo surgical interventions regularly to replace the batteries.

Nuclear batteries were introduced to expand the lifetime of the batteries in the 1970s [22]. However, in the early 1980s, these radioactive batteries were discontinued due to the potential risks [23].

In 1972, the first lithium/iodine battery was patented [24]. This technology is used today as it has a higher energy density than other commercial technologies [25]. The volumetric energy density of the lithium/iodine batteries is one of the highest, near 1 $Wh/cm^3$ [26].

Considering a 1 $cm^3$ battery, its stored energy can be enough to feed a state-of-the-art pacemaker for several years. Nevertheless, for applications that require at least 1 mWh, the battery will run out in less than six weeks, so the patient should undergo another intervention. Therefore, with current battery technologies, developing submillimetric AIMDs is not feasible.

For applications with a high energy use rate, rechargeable lithium-ion batteries can become a reliable and appropriate solution since the possibility of recharging the battery allows it to obtain high power without compromising its lifetime [27]. Using batteries as an energy storage buffer implies that it is necessary to transfer energy to the implant externally. Nowadays, the most common method to recharge the AIMDs batteries is through inductive coupling (this method is detailed in 2.1.2.1).

Examples of commercial AIMDs powered by batteries are given below (Fig. 2.1). The Medtronic Micra™ is a pacemaker that can be deployed percutaneously. It has a mass of 1.75 g and a volume of 0.8 $cm^3$. Its battery is non-rechargeable and has expected longevity of 8-13 years. The Medtronic ActicaTM RC is a deep brain stimulation system that in includes a rechargeable battery. It has a weight of 40 g, a height of 54 mm, and a length of also 54 mm.


**Fig. 2.1.** Examples of AIMDs powered by batteries. **Left**: Medtronic Micra™. **Right:** Medtronic Activa™ RC.

#### *2.1.1.2 Energy scavengers*

In recent years, several energy-scavenging methods have been proposed to avoid using batteries and external energy sources and thus obtain more autonomous and robust systems. These methods get electrical energy by converting the inherent energy present in the medium where implants are located [14]. However, nowadays, the power densities obtained by these approaches are well below 10 $\mu W/mm^2$. For this reason, it is difficult to conceive a scenario where the powers of mW are obtained using energy scavengers. To the best of our knowledge, no energy scavenger is in use in actual clinical implant. Nevertheless, these methods can become an appropriate way to power supply devices with low power requirements, e.g., nerve stimulators. Below, some of the most representative energy scavengers' methods are briefly described.

The operating principle of thermoelectric harvesters is the Seebeck effect (i.e., a voltage is produced over a conductive or semiconductive bar whenever both ends are at different temperatures). Since the generated voltages due to the Seebeck effect are too low to feed an electronic implant, thermoelectric scavengers connect several thermocouples in series to increase the harvested voltage (i.e., to form a thermopile).

In [28], Strasser and his colleagues could obtain a power of 1 μW considering a thermopile with an area of 1 $cm^2$, having a temperature difference between both terminals of 5 °C. Since the voltage harvested depends on the temperature gradient, and the inner body temperatures vary just a few degrees, this method can only obtain powers of a few μW [29]. Thus, thermoelectric scavenging only is recommended for ultra-low power applications.

Piezoelectric scavengers get electric energy from the kinetic energy produced by body movements. Its use for wearable devices has been broadly studied. For example, Zhao et al. obtained powers of mW placing piezoelectric transducers in the sole of shoes [30]. In the case of natural contractions of the body, powers obtained are still too low to feed most of current AIMDs. As an example, Rogers et al. investigated the use of the natural contractions and relaxations of the heart, lungs, and diaphragm to power supply biomedical implants

[31]. Although they proposed the use of a flexible and technically impressive circuit, their results show that power densities of just hundreds of nW can be scavenged using these natural movements. Along the same line, Dong et al. [32] designed an implantable cantilever to be attached in a pacemaker lead, and in this way produce electrical energy from the natural movements of the heart. The authors of this study concluded that using their method, tens of nW can be scavenged.

A fuel cell generates powers by catalyzing complementary electrochemical reactions at a pair of corresponding electrodes. Recently, the use of glucose as a biofuel has been proposed to allow the development of autonomous AIMDs [33]. In a glucose-based biofuel cell, the electrochemical reactions consist, on one hand, in oxidizing glucose at the anode, and on the other hand, in reducing oxygen to water at the cathode. The *in silico* results presented in [33] show that a glucose-based fuel cell surrounded by cerebrospinal fluid can obtain power densities of 3.4 $\mu W/cm^2$. In a more recent study, Zebda et al. presented a glucose-based fuel cell based on carbon nanotube/enzyme electrodes [34]. The developed cell was implanted in the abdominal cavity of a rat, and it obtained a power density of 193.5 $\mu W/cm^2$.

### 2.1.2 *WPT methods*

#### *2.1.2.1 Inductive coupling*

Schuder et al. [35] first proposed using inductive coupling to power biomedical implants in 1961 to power supply an artificial heart. Nowadays, near-field inductive coupling (NFIC) is the most used wireless power method [36], especially in the case of cochlear implants [37].

NFIC works on the principle of electromagnetic (EM) induction [38]. A time-varying magnetic field is produced by a transmitting coil (TX) which usually is placed close to the skin. Part of this field produces an electromotive force in the receiving coil (RX), which is implanted inside the body (Fig. 2.2). In most cases, the NFIC links are conceived to get high power transmission efficiencies. Consequently, these systems are designed to operate under resonance conditions to minimize transmission losses. Because of the biological

properties of the tissues, part of the coupled energy is dissipated by the tissues due to Joule effect. Therefore, the maximum applied power must be limited to avoid tissue overheating [39].

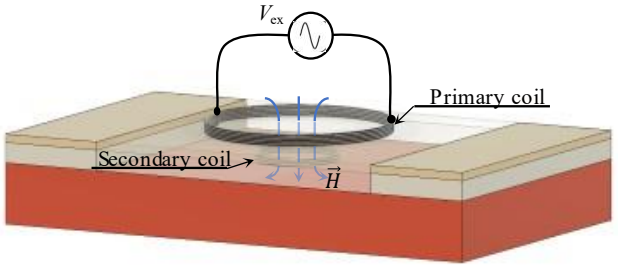


**Fig. 2.2.** Schematic representation of inductive coupling

The maximum power received in the implant is closely related to the RX coil diameter and the separation distance between TX and RX coils. Therefore, the reported results vary depending on these parameters. As an example, powers of 100 mW were reported by RamRakhyani et al. [40], considering an RX coil with a diameter of 20 mm, and a separation distance between coils of 20 mm. In [41], Feng et al. obtained a power of 160 µW considering a 4 mm in-CMOS coil, while Ahn et al. reported powers of just 224 µW using an RX coil with a diameter of 1 mm, and a separation distance of 12 mm [42].

Inductive coupling can achieve efficiencies above 90%. However, its performance can be severely reduced due to multiple factors, e.g., coil misalignment because of tissue movements (since the implants are placed in a moving frame) or detuning because of coil-flexion. Furthermore, NFIC links suffer from performance degration if RX is much smaller than TX or if the distance between both coils is greater than the RX coil size [43]. Because of these dependencies and the obtained results [44], it is difficult to conceive scenarios where powers of mW could be transmitted to sub-millimetric, deep-seated implants using inductive coupling [19].

To overcome this limitation and power deeply seated implants, the use of intermediate coils [45] and Helmholtz coils [46] have been proposed. However, in the former, although the use of intermediate coils favors the reduction in the size of the AIMD, the system still

requires the implantation of a bulky intermediate coil between the external one and the AIMDs. In the later, by using a Helmholtz coil is possible to couple a broadly uniform magnetic field several centimeters inside the tissues. Nevertheless, the implant must include a cylindrical coil that can hardly be submillimetric shaped [46].

To maximize the efficiency and the obtained power when the implant is spaced several millimeters from the source, Poon et al. proposed the use of the so-called midfield WPT as an alternative to near field inductive coupling [44]. In their analysis, Poon et al. concluded that for a separation distance above one centimeter between the TX and RX coils, the power received on the implant is maximized if the wavelength of the applied field matches this separation distance. Therefore, they propose using frequencies in the sub-GHz or GHz region for these cases. Furthermore, instead of using coils, they suggest the use of metasurfaces. These surfaces, through phase changes, allow the focusing of the applied field to the desired area [47].

Using the midfield WPT method, Poon et al. obtained powers of 2.2 mW in a microimplant (2 × 3.5 mm) placed in the lower cortex region of a porcine brain [2]. In the same way, Agrawal et al. use the midfield to feed a self-custom pacemaker (1.5 × 3 mm) [48]. This pacemaker was placed 4 cm inside the thoracic cavity of a pig. Under these conditions, the device obtained power of 600 μW, which was enough to pace the pig's heart.

#### *2.1.2.2 Ultrasonic acoustic coupling*

Using ultrasonic waves as a WPT method was suggested by Rosen et al. in [49]. In this method, the energy is transferred between the external source and the implant through mechanical waves. First, mechanical waves (which have a frequency above > 20 kHz) are produced and coupled into tissues by an ultrasonic TX. Then, these waves propagate through the tissues, and part of them are collected by an implanted piezoelectric RX, which converts the acoustic energy into electrical energy to feed an AIMD (Fig. 2.3).

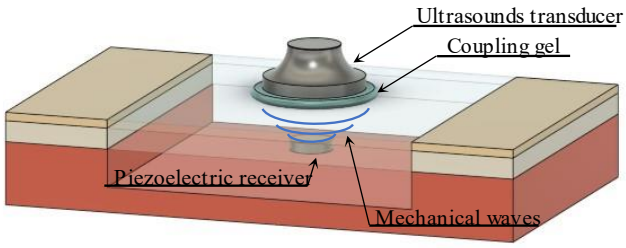


**Fig. 2.3.** Schematic representation of coupling based on ultrasonic coupling.

Like in the NFIC case, the received power using ultrasounds is closely related to both the RX size and the separation distance between the source and the receptor element. For example, in [50], Ozeri and Shmilovitz describe the optimization process they performed to maximize the power transferred through 3 cm of swine tissue and using a 15 mm diameter piezoelectric transducer, the implant received 28 mW. On the other hand, the work done by Mazzilli et al. in [51] was focused on transferring powers of tens of mW considering distances greater than 10 cm. The results show that using ultrasounds as a WPT method, it is possible to transfer 20 mW over 10.5 cm, using an RX with dimensions of $10 \times 5$ mm$^2$. Ibrahim et al. studied the possibility of optimizing the TX transducer to focus the acoustic beam at the desired point when this point is located several centimeters from the source [43]. Their results show the feasibility of the proposed method since they obtained powers of 2.1 mW, considering a separation distance of 3 cm, and having a millimetric RX (1.1 mm$^3$). Following, Kashani et al. [52] obtained a power of 6 mW considering a separation distance of 30 mm and a millimetric RX (~1 mm$^3$).

Several publications have suggested that this method requires long-term tests to confirm that the acoustic intensities applied do not cause tissue damage [36]. As there is a lack of regulations for using ultrasounds as WPT, nowadays, ultrasonic WPT applications are applying the safety limit that is used in ultrasonic diagnostic applications, i.e., 720 mW/cm$^2$ [53]. Apart from the damage that acoustic waves can cause, it is also important to study potential adverse effects derived from long-time exposure to the gel used to couple the acoustic waves into the tissues.

#### *2.1.2.3 Coupling by volume conduction*

Volume conduction is a term used in bioelectromagnetism to define the transmission of electric fields through biological tissues. Volume conduction is physical phenomenon found in several biomedical technologies. For instance, in bioimpedance applications [54], in transcutaneous electrical nerve stimulation [55], in short-wave diathermy [56], and more recently in the use of the tissues as a transmission channel for intra-body communications. This method usually is referred in the literature as capacitive coupling [57].

Although, volume conduction coupling for intrabody communications has been studied lately by different research groups [57]–[59]. Its use to power implants has remained almost inexistent until the last years. We conjecture that such neglect is due to a failure to recognize that, first, large magnitude HF currents can be safely coupled to the tissues if they are applied as short bursts. Second, to get a sufficient voltage in the implant, its electrodes must be separated by a few centimeters. However, the implant can be shaped as an elongated body, whereby the implant may be minimally invasive. During the last years, the use of volume conduction has been proposed by different groups independently. Although these groups use the same operating principle to transfer energy to implants, considerable differences between the proposed approaches can be observed.

Zhide et al. in 2006 [60] and Sodagar and Amiri in 2009 [61] proposed the use of coupling based on volume conduction to supply tens or hundreds of milliwatts through the skin to power implants in an efficient way.

In 2011, Ivorra proposed the coupling based in volume conduction to produce neuromuscular stimulation [62]. In 2013, the use of this method for powering these stimulators was proposed [63]. During the last years, this technology has been developed until obtaining addressable microstimulators with a diameter below 1 mm [64].

In 2018 Chen et al. also proposed the use of coupling based in volume conduction for transmitting power to AIMDs [65].

Coarsely the described approaches can be sorted into two different configurations that can be labeled as 1) planar configuration and 2) threadlike configuration.

### *2.1.2.4 Planar configuration*

The planar configuration was initially proposed in [60] and [61]. This configuration consists of placing four planar electrodes (two external and two internal) in pairs sandwiching the tissue, as illustrated in Fig. 2.4. This method applies an AC voltage between the two external electrodes. Due to the mutual impedance between the external and internal electrodes, the implant draws current from the source.

Although this method usually is referred to in the literature as Near-Field Capacitive Coupling (NFCC) [66], in our opinion, the use of this name is not accurate, since the flowing currents between the electrodes are mostly ohmic. For this reason, NFCC has been considered as a particular case of volume conduction.

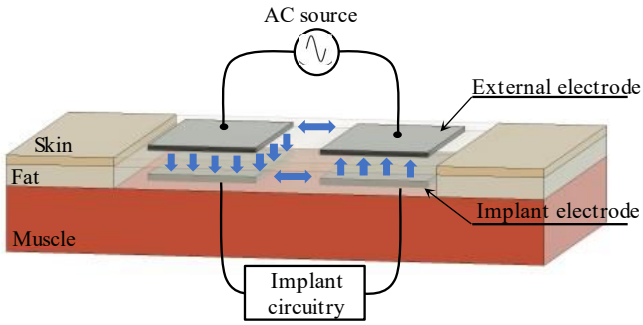


**Fig. 2.4.** Schematic representation of volume conduction in its planar approach.

In volume conduction, the biological tissue dissipates energy in the form of heat due to the Joule effect. To minimize these losses, the so-called planar approach tries to form two planar capacitors between the external and the implanted electrodes. This configuration aims to increase the displacement currents. And consequently reduce the losses due to the Joule effect [66]. However, like in the inductive coupling method, the transmission efficiency of this link is very sensitive to the separation distance between the superficial and the

implanted electrodes. For this reason, this approach is used only for shallow applications, i.e., with separations between external and internal electrodes below 10 mm.

The first detailed study of volume conduction in its planar approach was realized by Jegadessan et al. in 2017 [66]. In this original analysis, it was demonstrated that powers above 100 mW can be transferred using volume conduction. These results were obtained in *ex vivo* studies in non-human primates.

This method can become an appropriate alternative to the use of NFIC for two main reasons. First, the NFCC links are not resonance based. Hence, its performance is less sensitive to occasional alternations that the system can suffer, unlike the NFIC. Second, the electrodes can be manufactured using flexible materials allowing the tissue bending.

#### *2.1.2.5 Threadlike configuration*

In [63], Ivorra et al. described that coupling based on volume conduction could flavor the development of thin and elongated implants (i.e., threadlike implants). This configuration is highly beneficial in terms of minimal invasiveness as it allows percutaneous deployment.

The principle of operation of this approach consists in applying ac voltage between two external electrodes to produce an electric field inside the tissues, like in the planar configuration. This electric field produces a voltage gradient within the tissues, and these potentials can be picked-up by thin, elongated implants with one electrode at each end. This scenario is illustrated in Fig. 2.5.

Remarkably, the inherent property of the volume conduction that causes the electric field to be distributed through the tissues, combined with the fact that the implants are minimally invasive, allows these implants to be placed into deep tissues. Moreover, the same electric field that is applied to power a single implant can be used to power a swarm of implants (as long as they are located in the area where the electric field is applied), without having to increase the applied power of the external system or its complexity.

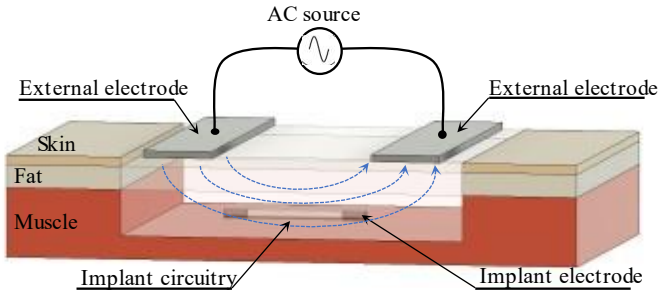


**Fig. 2.5.** Schematic representation of volume conduction in its threadlike approach.

To obtain a considerable electric potential, the separation distance between the implant electrodes must be a few centimeters. Therefore, the implants can be shaped as thin and flexible elongated bodies.

Previous work done in our group has highlighted that neuromuscular stimulation can be obtained by means of local rectification of the applied external currents [20], [62], [64], [67]–[69]. Moreover, in their study Becerra-Fajardo et al. demonstrated that volume conduction can also be used for powering active injectable medical devices [20]. In this work, a 2 mm thick, semi-flexible, injectable stimulator was developed. This stimulator had a complex electronic circuitry based only on off-the-shelf components, that was controlled by a commercial microcontroller (Attiny20, 1.555×1.403 mm). Since the energy obtained to feed this electronic circuit was obtained using volume conductions as a WPT method, this work provided clear evidence to support this method to power supply active biomedical devices. Moreover, a more advanced circuity that includes electromyography acquisition and bidirectional communications, and which is aimed for acute studies in humans, has been recently demonstrated in animal models [70].

### 2.1.3 *Wireless power transfer method comparison*

Table 2.1 summarizes the WPT methods for powering AIMDs described in the previous sections. In this table, *depth* refers to the distance between the implant location and the medium surface. The *volume* parameter includes only the element used to obtain energy.

The parameter *max. dimension* is the maximum length of the element used to obtain energy in one dimension. Other parameters included in the comparison table are: *PDL*, power delivered to the load; $P_{\text{Total}}$, the applied power, and *PTE* the power transmission efficiency (i.e., *PDL* divided by $P_{\text{Total}}$). To compare the capability to obtain powers with minimally invasive implants, the Figure of Merit 1 ($FoM_1$) (2.1) has been determined as the ratio of the PDL by the maximum dimension.

$$FoM_1 = \frac{PDL}{max.\,dimension}. \tag{2.1}$$

Figure of Merit 2 ($FoM_2$) (2.2) highlights the potential of the method to transfer powers when implants are deeply placed. It is calculated as the PDL multiplied by the square of the depth.

$$FoM_2 = PDL \cdot depth^2. \tag{2.2}$$

Finally, the Figure of Merit 3 (FoM3) (2.3) is the power density of the harvester component. It is calculated as the ratio of the PDL by the harvester volume.

$$FoM_3 = \frac{PDL}{volume}. \tag{2.3}$$

Table 2.1 highlights that powers of mW cannot be obtained by inductive coupling using coils with diameters of less than one millimeter. These experimental results are in concordance with a theoretical analysis done by Heetderks [19]. Regarding the volume conduction on its threadlike approach [71], this method stands out in terms of the power density ($FoM_3$). Furthermore, using the threadlike approach, powers of mW can be transferred to implants several centimeters away from the transmitter ($FoM_2$). Nevertheless, [71] obtained the lowest $FoM_1$. This result can be explained as, although the pick-up electrodes can be sub-millimetric, to obtain powers of mW the inter-electrode distance must be of a few centimeters. However, this fact is not problematic since these implants can be shaped as a thin and flexible elongated body, which is a configuration

TABLE 2.1
COMPARISON OF THE WPT METHODS

| Parameter | [71] | [66] | [72] | [43] | [73] | [48] | [74] | [75] | [42] | [40] | [76] | [46] |
|---|---|---|---|---|---|---|---|---|---|---|---|---|
| WPT method | VC | VC | VC | US | US | MF | MF | MF | NFIC | NFIC | NFIC | NFIC |
| Medium | NaCl solut. | Tissue | NaCl solut. | Castor Oil | Tissue | Tissue | Tissue | Tissue | Tissue | Air | Tissue | NaCl solut. |
| Depth (cm) | 3 | 0.25 | 2.75 | 3 | 2.15 | 4 | 4 | 5 | 1.2 | 2 | 2.5 | 5 |
| Volume ($mm^3$) | 1* | 1600 | 314 | 1.1 | 0.42 | 5.3 | ~ 6.3 | 38 | 0.79 | ~950 | ~0.13 | 1150 |
| Max. dimension (mm) | 30.5** | 28.3 | 20 | 1.2 | 1.1 | 3.4 | 2 | 7.5 | 1.4 | 22 | 1 | 30 |
| SAR (W/kg) | 10 | 2 | 2 | † | † | 8.9 | 10 | - | 1.6 | - | 1.6 | 2 |
| PDL (mW) | 3.3 | 137.8 | 10 | 2.1 | 0.35 | 0.6 | 2.2 | 6.7 | 0.22 | 80 | 0.036 | 10 |
| $P_{Total}$ (W) | 3.1 | 0.25 | 2.2 | 0.08 | - | 0.8 | 0.5 | 1 | 0.04 | 0.4 | - | 2.5 |
| PTE (%) | 0.1 | 55.1 | 0.5 | 2.6 | - | 0.1 | 0.4 | 0.7 | 0.6 | 20 | - | 0.4 |
| $FoM_1$ (mW/mm) | 0.11 | 4.87 | 0.5 | 1.75 | 0.32 | 0.18 | 1.1 | 0.9 | 0.16 | 4.55 | 0.22 | 0.33 |
| $FoM_2$ ($mWcm^2$) | 29.7 | 8.6 | 75.6 | 18.9 | 1.6 | 9.6 | 35.2 | 167.5 | 0.3 | 320 | 0.036 | 250 |
| $FoM_3$ ($mW/mm^3$) | 3.1 | 0.086 | 0.032 | 1.91 | 0.83 | 0.11 | 0.35 | 0.18 | 0.28 | 0.084 | 0.28 | 0.01 |

VC: Volume conduction; US: Ultrasounds; MF: Midfield; NFIC: Near field inductive coupling.
PDL: power delivered at the load. PTE: Power transmission efficiency. $FoM_1$: PDL/Max. dimension; $FoM_2$: PDL·$Depth^2$; $FoM_3$: PDL/Volume.
†: The used acoustic intensity was 720 $mW/cm^2$. *Volume of two spheres (diameter = 0.5 mm). **Inter-electrode spacing of 30 mm.

highly suitable for minimally invasive deployment through injection or catheterization.

An additional parameter that has a crucial role in the development of AIMDs is the feasibility of hermetically packaging the devices [77]. From one side, to avoid a premature failure of the AIMD circuity, its package has to avoid the moisture entrance. And on the other side, the implant encapsulation has to be biocompatible. The current materials used nowadays that ensure both properties are metals, ceramics, and glasses [77].

Regarding encapsulation, coupling based on volume conduction has an advantage over radiated WPT methods because it allows the use of metallic materials. And since using metals allows for thinner encapsulations than those obtained with ceramic materials [78], the final implant size cam be reduced by using this material.

## 2.2 Safety considerations

The exposure of the human body to non-ionizing electric fields has associated risks that must be adequately addressed to use volume conduction as a WPT method. The Institute of Electrical and Electronics Engineers (IEEE) and the International Commission on Non-Ionizing Radiation Protection (ICNIRP) safety standards for human exposure to electromagnetic fields identify two general sources of risk regarding the passage of radiofrequency currents through the body [39], [79]. In terms of the WPT methods described above, the limitations affect both the inductive coupling method and the method based on volume conduction. The standards indicate the risk of thermal damage due to the Joule's effect, and recognize risks caused by unsought electrical stimulation of excitatory tissues with harmful effects ranging from mild perception to death by ventricular fibrillation.

While the risk due to thermal damage can be considered almost a frequency-independent risk, the risk of experimenting unwanted stimulation becomes especially relevant for electric fields with

frequencies below 100 kHz. Therefore, the IEEE safety standard [39] defines the maximum allowed induced *in situ* electric field ($MPE_{\mathrm{n}}$) to avoid the stimulation risk.

For pure-sinusoidal fields with a frequency $f_{\mathrm{n}}$, considering that the field is being applied in the extremities, the peak value of $MPE_{\mathrm{n}}$ is calculated as

$$MPE_{\mathrm{n}} = \begin{cases} \dfrac{2.1\sqrt{2}}{3350}, & f_{\mathrm{n}} < 3350 \\ \dfrac{2.1\sqrt{2}}{3350} f_{\mathrm{n}}, & f_{\mathrm{n}} \geq 3350 \end{cases}. \tag{2.4}$$

$MPE_{\mathrm{n}}$ is determined by averaging the electric field received over a straight-line segment of 5 mm length and considering a time interval of 0.2 s. However, for non-pure sinusoidal fields, the IEEE standard [39] indicates that the low-frequency harmonics must be checked, and it specifies

$$\sum_{0}^{5\ \mathrm{MHz}} \frac{E_{\mathrm{n}}}{MPE_{\mathrm{n}}} \leq 1, \tag{2.5}$$

where $E_{\mathrm{n}}$ is the magnitude of the nth Fourier component of the exposure electric field, and $MPE_{\mathrm{n}}$ is the maximum permissible exposure for *n* frequency calculated as (2.4).

When electric fields with frequencies above 5 MHz are applied, stimulation can hardly be produced [39], as the limit is above 4.4 kV (2.4). In this case, $E_{\mathrm{n}}$ must be limited to avoid tissue overheating. For frequencies between 100 kHz and 5 MHz both limitations must be considered.

Regarding the overheating, both IEEE and ICNIRP standards use the so-called Specific Absorption Rate (SAR) to limit the maximum power that can be dissipated by the tissues [39], [79]. The SAR is defined by time derivate of the incremental energy ($\partial W$) dissipated in an incremental mass ($\partial m$) corresponding to a tissue volume ($\partial V$) of a given mass density ($\rho$) as

$$SAR = \frac{\partial}{\partial t}\left(\frac{\partial W}{\partial m}\right) = \frac{\partial}{\partial t}\left(\frac{\partial W}{\rho \partial V}\right). \quad (2.6)$$

And can be calculated at any point of the tissue with the following expression

$$SAR = \frac{\sigma |E_{\text{rms}}|^2}{\rho}, \quad (2.7)$$

where $\sigma$ is the electric conductivity of the tissue (S/m), $\rho$ is the mass density of the tissue (kg/m$^3$) and $E_{\text{rms}}$ is the root mean square value of the electric field in the tissue (V/m).

Both the IEEE standard and the ICNIRP guidelines indicate the same SAR limitations averaged over 6 minutes for localized exposure in the frequency range from 100 kHz to 3 GHz. The tissue averaging mass for the peak spatial-average SAR is 10 g in the shape of a cube (approximately 10 cm$^3$). The standard [79] has increased the averaging mass from 1 g to 10 g since the results of extensive theoretical biophysical research quantifying RF energy penetration in biological tissue have shown that RF energy is incapable of causing significant local temperature increases in small tissue volumes.

For the general public, the SAR limit is set to 4 W/kg for extremities and pinnae, and it is set to 2 W/kg for the rest of the body locations. For occupational exposure or persons in controlled environments this limit is 10 W/kg, and it is further increased up to 20 W/kg if the localized exposure is at extremities [39], [79]. Since the final design will incorporate several sensors to monitor and ensure that the system operates in safe condition and that the protocols applied using the HF currents will be reviewed by physicians, this thesis considers the restrictions for persons in controlled environments.

The limitation of 10 W/kg pretends to avoid temperature increases above 1°C. This limitation is consistent with the results obtained by the WHO in [80], where they observed that a 1°C rise in temperature is not adverse, even in sensitive tissues.

The SAR limit entails the following limitation for continuous sinusoidal electric fields

$$E_{\text{peak}} \leq \sqrt{\frac{2\rho SAR}{\sigma}}, \tag{2.8}$$

If the field is applied using bursts,

$$E_{\text{peak}} \leq \sqrt{\frac{2\rho SAR}{\sigma FB}}, \tag{2.9}$$

where $F$ is the repetition frequency (Hz), and $B$ is the burst duration (s). For the same SAR restriction, the value of $E_{\text{peak}}$ can be considerably incremented if the field is applied using short burst.

Finally, the whole-body SAR should not exceed 0.4 W/kg to avoid core-body temperature increase. The energy dissipated by the body considering this whole-body SAR restriction is equivalent to about a third of the heat production over an average adult, and it is completely benign [39].

## 2.3 Volume conduction models

During the last years, several models have been proposed to describe the transmission of electric fields through the tissues for different applications, such as volume conduction in its planar approach, galvanic coupling for wireless body area networks, or to determine the superficial EMG produced by inner muscular fibers.

The following section describes the most representative models proposed throughout the years. These methods have been classified into three different categories: lumped models, analytical models, and finite element methods. Nevertheless, as the use of volume conduction in its threadlike approach has remained almost non-existent, in the literature, there is not yet a model capable of determining the power an implant can receive using this method.

### 2.3.1 *Lumped models*

The lumped models concentrate the spatial-distributed behavior of the real system into a discrete set of idealized components. These discrete elements are interconnected between them using idealized electric wires.

In [66], [81], [82] a lumped series equivalent circuit is proposed to model volume conduction in its planar approach. In these works, just a single layer of tissue was considered. The electrodes were planarly aligned with a separation distance between the external and internal electrodes of a few millimeters. They neglected the fringing fields, ignoring cross-interactions between electrodes. Additionally, the dielectric layer of tissue was modeled as the parallel of an ideal capacitor and a resistor (dielectric loss).

In [66], Jegadeesan et al. introduced a lumped model to describe the link for volume conduction in its planar approach. The results highlight a substantial discrepancy between the analytical results and the experimental measurements. From the point of view of the authors, these differences were attributed to the fact that the real electrodes were coated with a PDMS layer to be biocompatible, and this parameter was not modeled [81]. This was not the case for the work of Narayanamoorthi et al. They obtained an appropriate match between the analytical and the experimental results using a similar analytical model topology.

The initial lumped model has been extended by Erfani et al. to consider cross-interactions between electrodes [83]. The proposed lumped circuit models the tissue through six resistors and two capacitors (Fig. 2.6). Although it was not clearly reported how the impedance values were obtained, the analytical results matched the experimental measurements. In [72], the same topology was recently adapted to model the power transmission to implants deeply placed in the torso. Remarkably, this circuit topology was proposed several years ago to model galvanic coupling for intrabody communications in [84], [85].

Lumped models have also been proposed to model multi-layered tissues [85], [86]. However, these works suffer from conceptual and methodological weaknesses. For instance, in [85], the authors found

a discrepancy between the analytical and the experimental results of one order of magnitude. Similarly, in [86], the authors apply a correction factor of one order of magnitude to match the analytical and experimental results properly. Moreover, it is not clearly explained how this correction factor was determined. For these reasons, these models cannot be considered validated models.

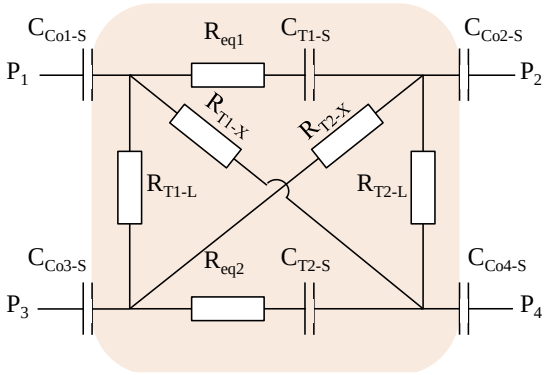


**Fig. 2.6.** Lumped model proposed by Erfani in [83]. Adapted from [83].

### 2.3.2 *Analytical models*

The analytical models pretend to reflect the physical behavior of the transmission system using mathematical expressions.

For the volume conduction case, this model has to mathematically describe the relationship between the applied current and its consequent electric field distribution inside the tissues. In most cases, obtaining this analytical expression implies the solution of a mixed boundary problem for a multi-layered tissue.

The electric field distribution that will be produced by the current generated by a muscle fiber has been widely investigated. Among these studies, one of the most relevant to the volume conduction case is the work done by Farina et al. in [87]. In this study, the authors present an analytical model to determine the electric field distribution produced by a muscular fiber (modeled as a tripole) placed inside a concentric multi-layered tissue. Furthermore, their analytical model can numerically simulate surface electromyography signals for

different electric sources placed inside the tissues. However, the application of this model is limited to ideal scenarios (concentric cylindrical tissues), and to scenarios where the external electrodes are punctual.

In recent years, the use of analytical models to model galvanic coupling communications has also been proposed. For example, in [88], the authors simplified the body geometry using multi-layered ellipsoids. Using this simplification and considering dimensionless electrodes, the authors developed an analytical model that describes the voltage distribution within the tissue for a determined applied current. However, the validation of the model was done using a homogeneous saline solution. Thus, the validity of this model for multi-layered scenarios is unclear.

Pun et al. proposed an analytical model for galvanic coupling communications, where all the electrodes were attached over the skin [89]. Their study simplified the arm geometry into a multi-layered concentric cylinder. They compared the analytical results with a multi-layered agar phantom and with *in vivo* studies in humans. Although the error between the analytical and the *in vitro* results was lower than 10%, for the *in vivo* case, the experimental results differ significantly from the analytical results.

The analytical models have the advantage of describing the physical reality in a concise and mathematical way. For this reason, in many cases the analytical models are useful to identify the relevant factors of the system and its iterations. Also, the computational cost of solving these models is usually low. However, the obtention of a closed analytical solution is usually constrained to simple geometries. Therefore, it is difficult to conceive analytical models capable of modeling realistic systems accurately.

### 2.3.3 *FEM models*

To describe the distribution of the electric field within an anatomically and geometrically complex body such as the human body, several groups have proposed the use of finite element methods (FEM) [55].

Ruiz et al. initially proposed the use of FEM analysis to model a capacitive coupling channel for wireless body area networks [90]. In this work, the authors simplified the body's geometry, considering the extremities and the torso as concentric cylinders. Their simulated results were validated using *in vivo* measurements, and the comparison between both results highlights the validity of the FEM model. Finally, they presented an original method to model the FEM results using a lumped model.

This study was extended by Callejón et al. in [91] to consider galvanic coupling for intrabody communications. The study models the galvanic coupling system as a four ports network and uses the Cole-Cole model to consider the frequency-dependent behavior of the biological tissues. The same procedure was done in [92], but considering the brain instead of the arm.

FEM models are the counterpart of the analytical models. These models allow the solution of realistic problems with complex geometries. Nevertheless, the physical interpretation of the numerical results becomes challenging. In addition, as the complexity of the model increases, the computational cost also increases and may become a problematic factor.

# CHAPTER 3

## RECEPTION ANALYTICAL MODELS

**Abstract** —Galvanic coupling, or more precisely volume conduction, has been recently studied by different research groups as a method for intrabody communications. However, only in a very few occasions its use for powering implants has been proposed and proper analyses of such capability are still lacking. We present the development and the *in vitro* validation of a set of analytical expressions able to estimate the maximum ac and dc powers attainable in elongated implants when surrounded by a uniform electric field coupled with volume conduction. In particular, the expressions do not describe the complete power transfer channel but the behavior of the implants when the presence of an electric field is assumed. The expressions and the *in vitro* models indicate that time-averaged powers above 1 mW can be readily obtained in very thin (diameter < 1 mm) and short (length < 15 mm) implants when ac fields that comply with safety standards are present in the tissues where the implants are located. The expressions and the *in vitro* models also indicate that the obtained dc power is maximized by delivering the ac field in the form of short bursts rather than continuously. The study results support the use of volume conduction as a safe option to power implants.

Part of the contents of this chapter are adapted from the following publication:

M. Tudela-Pi, L. Becerra-Fajardo, A. García-Moreno, J. Minguillon and A. Ivorra, "Power Transfer by Volume Conduction: *In Vitro* Validated Analytical Models Predict DC Powers Above 1 mW in Injectable Implants," in IEEE Access, vol. 8, pp. 37808-37820, 2020, doi: 10.1109/ACCESS.2020.2975597.

## 3.1 Introduction

The use of volume conduction as a WPT method to power threadlike AIMDs was validated in [20], [68], [69]. Furthermore, although relevant properties of this method were already identified in [62] (e.g., the power of the implant increases with the distance between the implant electrodes), these works were mainly experimental and thus, do not describe the proposed method analytically. Moreover, as described in Chapter 2, the analytical models used for other volume conduction applications cannot be directly rearranged to describe the method described here. As stated in Chapter 1, to consolidate the described method, it is necessary to have an analytical model, which allows to identify the main parameters involved in the method and to determine the power an implant can obtain.

This chapter presents the development and validation of a set of analytical expressions able to estimate the maximum ac and dc powers attainable in elongated AIMDs, where a uniform electric field is applied. In particular, the expressions estimate the maximum ac and dc powers implants can obtain when ac fields that comply with safety standards are present in the tissues where the implants are located.

## 3.2 Methods: Models

### 3.2.1 *General features of the models*

The expressions developed in this chapter model the presence of an elongated implant within a tissue where an electric field exists due to delivery of current through two external electrodes. The modeled implant consists of two pick-up electrodes and an electric load (i.e., the electronics to be powered). This setup would represent hypothetical scenarios of use for the proposed WPT method such as the scenario depicted Fig. 3.1.

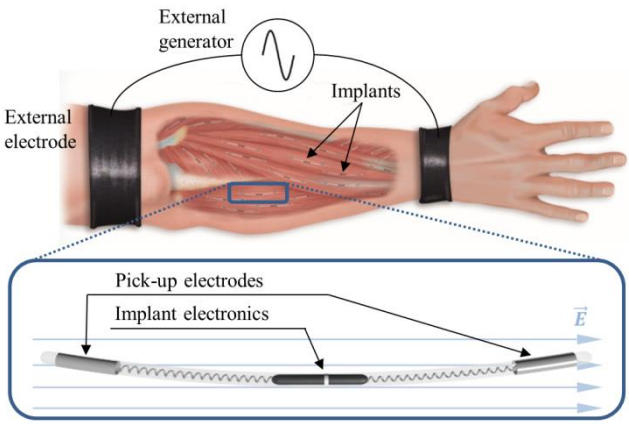


**Fig. 3.1.** Hypothetical scenario of use for the proposed WPT method. An ac electric field is generated in the forearm tissues across a pair of external electrodes. The implants draw electrical power using two electrodes located at their opposite ends. The devices could be used, for instance, as electrical stimulators or sensors.

The electric field is modeled as homogeneous at the location of the implant, and it consists in a sinusoidal waveform of frequency $f$ and amplitude $E_{peak}$ that can be applied continuously or in the form of bursts with duration $B$ and repetition frequency $F$ (Fig. 3.2).

Unless otherwise stated, $f = 5$ MHz. The angle formed by the field and the implant (i.e., direction defined by the two electrodes of the implant) is $\alpha$. Unless otherwise stated, $\alpha = 0$. To develop concise analytical expressions, the following assumptions and simplifications were made (most of them illustrated in Fig. 3.3):

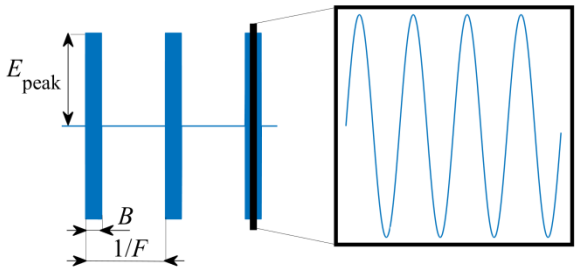


**Fig. 3.2.** The delivered electric field consists in a sinusoidal waveform of frequency f and amplitude $E_{peak}$ that can be applied continuously or in the form of bursts with duration B and repetition frequency F.

1. The implant is modeled as two conductive spheres, representing its pick-up electrodes (diameter $D$ and inter-center separation $L$) and a resistance $R_{Load}$ across these two electrodes that accounts for the electronics of the device (Fig. 3.3a).
2. The volume of homogeneous medium surrounding the implant is infinite relative to the dimensions of the implant.
3. The medium surrounding the implant (i.e., body tissue) is resistive. That is, rather than modeling the tissue surrounding the implant with, for instance, a Cole impedance model as it would be appropriate in a multi-frequency study, the tissue is modeled with a single resistance. This assumption is supported by the fact that at a single sinusoidal frequency the passive electrical properties of any material are appropriately modeled by a RC circuit (see Fig. 3.3b) and, at the frequencies considered here (1 MHz < $f$ < 20 MHz), soft tissues are predominately resistive, and the capacitive component can be neglected [93]. In particular, the phase of the admittivity of muscle tissue is only 11.5° at 1 MHz, 8.7° at 10 MHz and 10.8° at 20 MHz [94].
4. The passive electrical properties of the medium (i.e., body tissue) surrounding the implant are isotropic. This assumption is supported by the fact that when HF current is applied through the tissues, the capacitive membranes of the cells are virtually short-circuited, thus making the tissue isotropic [95]. Even in the case of muscle tissue, which is highly anisotropic at low frequencies, it can be considered isotropic for frequencies above 1 MHz [96].
5. The skin effect is considered negligible. The skin effect causes ac current density to concentrate near the surface of the conductors and hinders electric field penetration. However, in human tissues, because their relatively poor conductivity, the skin effect only becomes significant at frequencies well above 10 MHz [97]. As latter discussed, for WPT by volume conduction, we recommend the use of field frequencies below 20 MHz because of the skin effect.
6. The electrode-electrolyte interface impedance is considered negligible. This assumption is supported by the fact that the interface impedance of metal electrodes is roughly equivalent to a capacitance above 0.1 F/m$^2$ [98] that, for the electrode dimensions and the frequencies considered here, translates into an impedance magnitude in the order of tenths of ohm or a few ohms (e.g., 0.4 Ω for a spherical electrode with a diameter $D$ of

0.5 mm and at a frequency *f* of 5 MHz). Therefore, the electrode-electrolyte impedance is negligible to the equivalent resistance across the implant electrodes (see subsection 3.2.3).

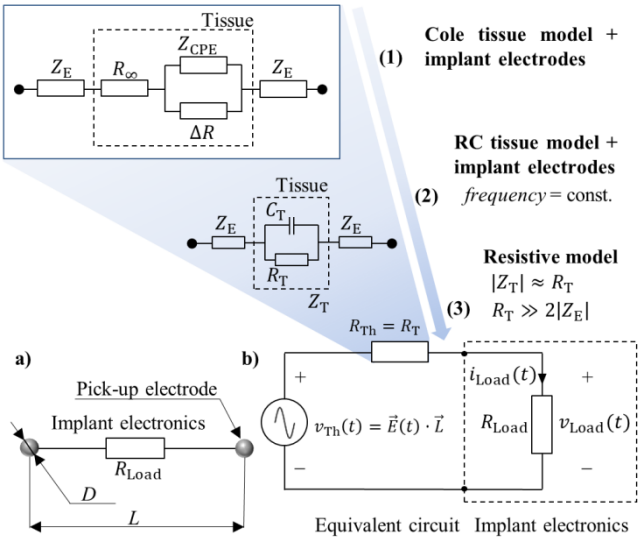


**Fig. 3.3.** a) The implant is modeled as two conductive spheres, representing its pick-up electrodes, and a resistance across these two electrodes that accounts for the electronics of the device. b) The tissue surrounding the implant, the implant electrodes and the presence of an electric field are modeled with a Thévenin equivalent circuit. To obtain closed analytical expressions, the combined impedance of the tissue and the electrodes is simply modeled with a resistance (see subsection 3.2.1). This approximation can be understood as a three-step process: first, the accepted Cole impedance model for living tissues is simplified to an RC circuit considering that the frequency of the field is constant. Second, as stated in the text, because of the high operating frequencies, the tissue is considered predominantly resistive, and $C_T$ is neglected. Third, since the impedance of the electrodes is much smaller than the impedance across them, the impedance of the electrodes is neglected.

### 3.2.2 *Limitations imposed by safety standards*

As explained in section 2.2, the safety standards developed by IEEE [39] and ICNIRP [79] implicitly limit the maximum value of $E_{peak}$.

These safety standards for human exposure to electromagnetic fields identify two general sources of risk regarding passage of radiofrequency (RF) currents through the body: 1) risk of thermal damage due to the Joule heating and 2) risks caused by unsought electrical stimulation of excitatory tissues with harmful effects ranging from mild perception to death by ventricular fibrillation. The limitations specified by the standards regarding heating are indicated as a limitation to the SAR. The SAR limit (2.7) entails the following limitation for continuous sinusoidal fields as in (2.8) and (2.9).

Unless otherwise stated, here the SAR limit of 10 W/kg averaged over 10 g of tissue has been considered. At 5 MHz and in muscle tissue ($\sigma$ = 0.59 S/m [94], $\rho \approx 1000$ kg/m$^3$ [99]), this field amplitude limit is roughly 180 V/m for FB = 1 and 580 V/m for $FB$ = 0.1. The standards indicate that above a specified frequency the risks caused by unsought electrical stimulation are negligible and only the SAR limitation applies. The IEEE standard rightfully indicates that the low frequency harmonics must be checked by using (2.5).

For persons in controlled environments and exposed tissues that are neither the brain nor the heart, the standard determines a *MPE* of $2.1\sqrt{2}$ V/m for frequencies below 3350 Hz. For frequencies above, the MPE is calculated as (2.4). This condition establishes another limit to $E_{\text{peak}}$ that can be lower than the threshold specified by the SAR limitation for low duty cycles (see appendix 3.7). For muscle tissue at 5 MHz ($\sigma$ = 0.59 S/m [94]), if $FB \geq 0.1$ then this second threshold is higher than that imposed by the SAR limitation and hence it can be neglected.

### 3.2.3 *Absolute maximum attainable power*

The implant is seen as a load by the tissues surrounding it. Therefore, since the passive electrical properties of tissues are linear, a Thévenin equivalent circuit can be implemented (Fig. 3.3b). This Thévenin model (circuit outside dashed square/box in Fig. 3.3b composed of $v_{\text{Th}}(t)$ and $R_{\text{Th}}$) locally models the tissues surrounding the implant, the implant electrodes and the presence of the electric field.

The Thévenin voltage is the open-circuit voltage. That is, the voltage across the implant electrodes when $R_{\text{Load}} = \infty$. If the electric field present at the location of the implant is sinusoidal, the Thévenin voltage ($v_{\text{Th}}(t)$) is also sinusoidal with amplitude [100]

$$V_{\text{Th peak}} = E_{\text{peak}} L \cos(\alpha) \tag{3.1}$$

or, in general, for any field waveform

$$V_{\text{Th rms}} = E_{\text{rms}} L \cos(\alpha). \tag{3.2}$$

The power drawn by the load is

$$\begin{aligned} P_{\text{Load}} &= \frac{V_{\text{Load}}^2}{R_{\text{Load}}} \\ &= \frac{\left(V_{\text{Th rms}} \frac{R_{\text{Load}}}{R_{\text{Load}} + R_{\text{Th}}}\right)^2}{R_{\text{Load}}}. \end{aligned} \tag{3.3}$$

For the circuit described in Fig. 3.3a, $P_{\text{Load}}$ is maximized when $R_{\text{Load}}$ matches $R_{\text{Th}}$. Hence the maximum power that the implant can draw is

$$\begin{aligned} \max(P_{\text{Load}}) &= P_{\text{Load}}\Big|_{R_{\text{Load}}=R_{\text{Th}}} \\ &= \frac{(\max(V_{\text{Th rms}}))^2}{4R_{\text{Th}}} \\ &= \frac{(\max(E_{\text{rms}})L)^2}{4R_{\text{Th}}} \\ &= \frac{\max(SAR)\,\rho L^2}{4R_{\text{Th}}\sigma}. \end{aligned} \tag{3.4}$$

The Thévenin resistance, $R_{\text{Th}}$, is the equivalent resistance across the implant electrodes as seen from the implant ($R_{\text{Load}} = \infty$). In an infinite volume, the resistance across two conductive spheres with a separation distance much larger than their diameter ($L \gg D$) can be approximated by [101]

$$R_{\text{Th}} = \frac{1}{\sigma \pi D}. \tag{3.5}$$

Hence the absolute maximum power that the implant can draw is

$$\max(P_{\text{Load}}) = \frac{\pi}{4}\max(SAR)\rho DL^2. \tag{3.6}$$

### 3.2.4 *Maximum unregulated dc power*

Most AIMDs will require dc power for functioning. In Fig. 3.4 it is represented the most likely circuit topology to be employed in AIMDs for extracting a dc power: a diode bridge full-wave rectifier combined with a smoothing capacitor.

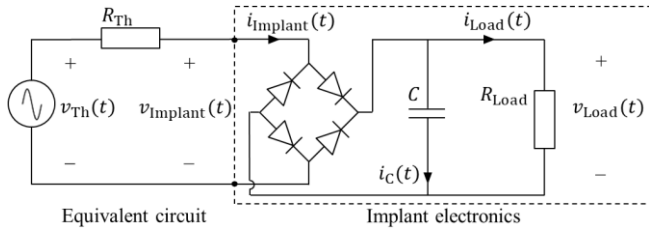


**Fig. 3.4.** Basic circuit topology for extracting dc power, consisting of a diode bridge full-wave rectifier combined with a smoothing capacitor, connected to the Thévenin equivalent. The Thévenin equivalent models the tissue surrounding the implant and the presence of the electric field.

For analyzing the behavior of this system, a procedure similar to that described in [102] is followed. Two assumptions are made. First, it is assumed that the ripple factor of the rectifier is almost zero. That is, the load voltage, $v_{\text{Load}}(t)$, is assumed to be constant (i.e., $v_{\text{Load}}(t) = V_{\text{Load}}$) once the circuit has reached steady-state. Second, the diodes of the full-wave rectifier are modeled by the series combination of an ideal diode, an ideal voltage source ($V_{\text{Diode}}$) which accounts for the forward voltage and a resistance ($R_{\text{Diode}}$). Initially, it is also assumed that the electric field at the location of the implant is a continuous sinusoidal field. Fig. 3.5 illustrates the main waveforms of the circuit under the previous assumptions. The constant load voltage, $V_{\text{Load}}$, can be expressed as being equal to the value of the Thévenin voltage at specific time points

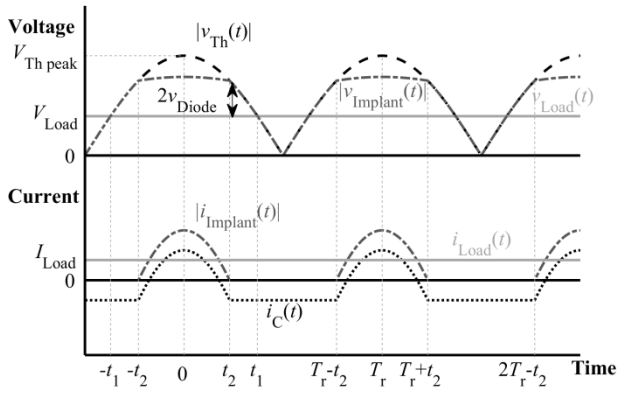


**Fig. 3.5**. Schematic representation of the main waveforms of the circuit represented in Fig. 3.4.

$$\begin{aligned} V_{\text{Load}} &= |v_{\text{Th}}(kT_{\text{r}} \pm t_1)| \\ &= \left|V_{\text{Th peak}} \cos(kT_{\text{r}}\omega \pm \varphi)\right| \end{aligned} \tag{3.7}$$

where $k$ is an integer, $T_r$ is the period of the rectified signal, $\omega$ is the angular frequency of the field and $\varphi$ is a phase angle that relates both voltages. In particular, for $k = 0$

$$V_{\text{Load}} = V_{\text{Th peak}} \cos(\varphi). \tag{3.8}$$

On the other hand, $i_{\text{Load}}(t)$ can be expressed as

$$i_{\text{Load}}(t) = \left|i_{\text{Implant}}(t)\right| - i_{\text{C}}(t). \tag{3.9}$$

Since $v_{\text{Load}}(t)$ is constant, $i_{\text{Load}}(t)$ is also constant

$$\begin{aligned} I_{\text{Load}} &= \frac{1}{T_{\text{r}}}\int_0^{T_{\text{r}}} i_{\text{Load}}(t)\, dt \\ &= \frac{1}{T_{\text{r}}}\int_0^{T_{\text{r}}} \left|i_{\text{Implant}}(t)\right| - i_{\text{C}}(t)\, dt\,. \end{aligned} \tag{3.10}$$

And since the average of $i_{\text{C}}(t)$ must be zero

$$I_{\text{Load}} = \frac{1}{T_r}\int_0^{T_r} \left|i_{\text{Implant}}(t)\right| dt. \tag{3.11}$$

The diode bridge only conduces when $|v_{\mathrm{Th}}(t)| > v_{\mathrm{Load}}(t) + 2V_{\mathrm{Diode}}$. Therefore

$$|i_{\mathrm{Implant}}(t)| = \begin{cases} \dfrac{V_{\mathrm{Th\ peak}}(\cos\omega t - \cos\varphi) - 2V_{\mathrm{Diode}}}{R_{\mathrm{Th}} + 2R_{\mathrm{Diode}}}, |v_{\mathrm{Th}}(t)| > v_{\mathrm{Load}}(t) + 2V_{\mathrm{Diode}} \\ 0, |v_{\mathrm{Th}}(t)| \le v_{\mathrm{Load}}(t) + 2V_{\mathrm{Diode}} \end{cases} \quad (3.12)$$

As indicated in Fig. 3.5, $i_{\mathrm{Implant}}$ flows between $kT_r - t_2$ and $kT_r + t_2$. These time points can be related to the phase of $v_{\mathrm{Th}}(t)$ defining a new phase angle

$$\theta = \omega_r t_2 = cos^{-1}\left(\frac{V_{Load} + 2V_{Diode}}{V_{Th\ peak}}\right). \quad (3.13)$$

Then $I_{\mathrm{Load}}$ can be calculated using (3.11) and (3.12) as follows

$$\begin{aligned} I_{\mathrm{Load}} &= \frac{1}{T_{\mathrm{r}}}\left[\int_0^{t_2} \frac{V_{\mathrm{Th\ peak}}(\cos\omega t - \cos\varphi) - 2V_{\mathrm{Diode}}}{2R_{\mathrm{Diode}} + R_{\mathrm{Th}}} dt + \int_{T_{\mathrm{r}}-t_2}^{T_{\mathrm{r}}} \frac{V_{\mathrm{Th\ peak}}(\cos\omega t - \cos\varphi) - 2V_{\mathrm{Diode}}}{2R_{\mathrm{Diode}} + R_{\mathrm{Th}}} dt\right] \\ &= \frac{2}{\pi}\frac{V_{\mathrm{Th\ peak}}\sin\theta - \theta(V_{\mathrm{Load}} + 2V_{\mathrm{Diode}})}{2R_{\mathrm{Diode}} + R_{\mathrm{Th}}}. \end{aligned} \quad (3.14)$$

From (3.8) and (3.14), the power obtained at the load is

$$\begin{aligned} P_{\mathrm{Load\ dc}} &= V_{\mathrm{Load}} I_{\mathrm{Load}} \\ &= \frac{2V_{\mathrm{Th\ peak}}}{\pi(2R_{\mathrm{Diode}} + R_{\mathrm{Th}})}\cos\varphi\left[V_{\mathrm{Th\ peak}}\sin\theta - \theta(V_{\mathrm{Load}} + 2V_{\mathrm{Diode}})\right]. \end{aligned} \quad (3.15)$$

It can be numerically verified that for a given $V_{\mathrm{Th\ peak}}$ and a given $V_{\mathrm{Diode}}$ there is an optimum value of $V_{\mathrm{Load}}$ that maximizes the obtained dc power.

The absolute maximum possible dc power will be obtained in the case of no loses, that is, in the case of ideal diodes (i.e., $V_{\mathrm{Diode}} = 0$ and $R_{\mathrm{Diode}} = 0$). In this case (3.13) can be rearranged as

$$V_{\mathrm{Load}} = V_{\mathrm{Th\ peak}}\cos(\theta). \quad (3.16)$$

Comparing (3.8) with (3.16), we can assert that, for this case, $\theta$ is equal to $\varphi$. Thus (3.15) becomes

$$P_{\mathrm{Load\ dc\ ideal}} = \frac{2V_{\mathrm{Th\ peak}}{}^2}{\pi R_{\mathrm{Th}}}\cos\varphi\,(\sin\varphi - \varphi\cos\varphi). \quad (3.17)$$

And it can be numerically determined that $P_{\text{Load dc ideal}}$ is maximum when $\varphi \approx 1.166 = \varphi_{\text{opt}}$ ($V_{\text{Load}} \approx 0.394\, V_{\text{Th peak}}$ and $R_{\text{Load}} \approx 1.35\, R_{\text{Th}}$). Substituting (3.1) into (3.17), and noticing that $E_{\text{peak}}$ has to fulfill (2.8), the maximum dc power that the implant can draw is

$$\max(P_{\text{Load dc ideal}}) = \frac{4\max(SAR)\,\rho L^2}{\pi R_{\text{Th}}\sigma}\cos\varphi_{\text{opt}}\left(\sin\varphi_{\text{opt}} - \varphi_{\text{opt}}\cos\varphi_{\text{opt}}\right). \quad (3.18)$$

For conductive spherical electrodes $R_{\text{Th}}$ is calculated as (3.5), and in this case (3.18) becomes

$$\max(P_{\text{Load dc ideal}}) = 4\max(SAR)\,\rho DL^2\cos\varphi_{\text{opt}}\left(\sin\varphi_{\text{opt}} - \varphi_{\text{opt}}\cos\varphi_{\text{opt}}\right). \quad (3.19)$$

The ratio between the maximum dc power that the implants can draw (3.19) and the absolute maximum attainable power (3.6) is

$$\begin{aligned}\eta &= \frac{\max(P_{\text{Load dc ideal}})}{\max(P_{\text{Load}})}\\ &= \frac{16}{\pi}\cos\varphi_{\text{opt}}\left(\sin\varphi_{\text{opt}} - \varphi_{\text{opt}}\cos\varphi_{\text{opt}}\right)\\ &\approx 0.9226.\end{aligned} \quad (3.20)$$

The above expressions were found under the assumption of a continuous sinusoidal field. For fields in the form of sinusoidal bursts with duration $B$ and repetition frequency $F$,

$$I_{\text{Load FB}} = \frac{2FB}{\pi}\frac{V_{\text{Th peak}}\sin\theta - \theta(V_{\text{Load}} + 2V_{\text{Diode}})}{2R_{\text{Diode}} + R_{\text{Th}}} \quad (3.21)$$

where the product $FB$ is the duty cycle of the bursts and it is comprised between $FB_{\min}$ and 1, where $FB_{\min}$ is the minimum duty cycle to prevent unsought stimulation. Hence the obtained power is

$$\begin{aligned}P_{\text{Load dc FB}} &= V_{\text{Load}} I_{\text{Load FB}}\\ &= \frac{2FBV_{\text{Th peak}}}{\pi(2R_{\text{Diode}} + R_{Th})}\cos\varphi\left[V_{\text{Th peak}}\sin\theta - \theta(V_{\text{Load}} + 2V_{\text{Diode}})\right].\end{aligned} \quad (3.22)$$

If $V_{\text{Th peak}} \gg 2V_{\text{Diode}}$ the phase angle $\theta$ defined in (3.13) will be equal to $\varphi$, see (3.8). Therefore, replacing $\theta$ by $\varphi$, and substituting (3.8) into (3.22) lead to

$$P_{\text{Load dc FB}}\left(V_{\text{Th peak}} \gg 2V_{\text{Diode}}\right) = \frac{2FBV_{\text{Th peak}}}{\pi(2R_{\text{Diode}} + R_{\text{Th}})}\cos\varphi\,[\sin\varphi - \varphi\cos\varphi]. \tag{3.23}$$

### 3.2.5 *Maximum voltage-regulated dc current*

In most practical cases the dc voltage will have to be regulated at a specific magnitude (e.g., +3.3 V) for powering the circuitry of the AIMD. Although switching regulators may be an option, because of size limitations, low-dropout (LDO) linear regulators will probably be preferred. The circuit in Fig. 3.6 represents such scenario. Linear regulators provide a regulated dc voltage at their output ($V_{\text{Load}}$) if the dc voltage at their input satisfies $V_{\text{Reg}} \geq V_{\text{Load}} + V_{\text{Drop}}$, where $V_{\text{Drop}}$ is the so-called dropout voltage, and they waste a small portion ($I_{\text{Q}}$) of the input current ($I_{\text{Reg}}$) so that $I_{\text{Load}} = I_{\text{Reg}} - I_{\text{Q}}$. In this case, since $V_{\text{Load}}$ is fixed, the objective is not to determine which is the maximum dc power at the load ($V_{\text{Load}}I_{\text{Load}}$) but the maximum current that can be obtained. The load seen by the diode-bridge and the smoothing capacitor ($C_1$) is the combination of the actual load ($R_{\text{Load}}$) and the load of the LDO regulator. Hence, the power expressions obtained above must be equaled to

$$\begin{aligned} P_{\text{Load+Reg}} &= V_{\text{Reg}}I_{\text{Reg}} \\ &= V_{\text{Reg}}\left(I_{\text{Load}} + I_{\text{Q}}\right). \end{aligned} \tag{3.24}$$

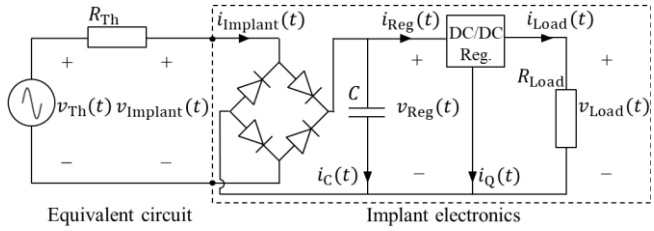


**Fig. 3.6**. Basic circuit topology for obtaining a regulated dc voltage to power a load ($R_{\text{Load}}$). Here it is assumed that the DC/DC regulator consists in a linear regulator.

The maximum regulated dc current that can be obtained ($I_{Load}$) is that one that ensures that the regulator works properly, that is, that for $V_{Reg} = V_{Load} + V_{Drop}$.

## 3.3 Methods: Setup for *in vitro* validation of the models

An *in vitro* experimental setup that replicates the assumptions made to develop the previous expressions was implemented (Fig. 3.7). The ac electric field was delivered by two 86.5×30 mm parallel aluminum plates acting as the external electrode These two electrodes were attached to opposite internal sides of a polycarbonate container (inner dimensions: 84 ×86.5×30 mm) filled with a NaCl solution whose conductivity was measured with a conductivity tester (HI 98312 by Hanna). Sinusoidal voltages, either continuous or in the form of bursts, were generated across the electrodes by the combination of a function generator (4064 by BK Precision) and a custom-made high-HF, high-voltage amplifier. In all instances, the applied voltage was measured using a digital oscilloscope (TPS2014 by Tektronix).

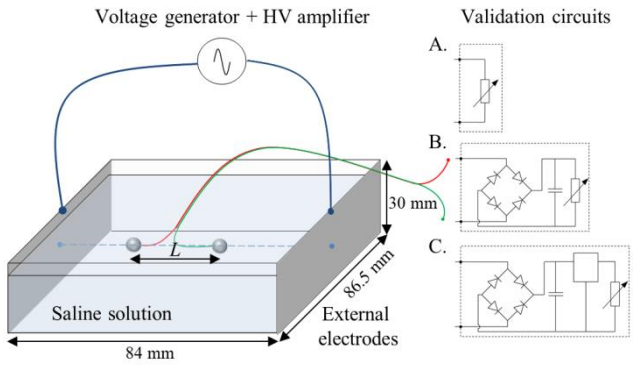


**Fig. 3.7.** Schematic representation of the *in vitro* setup developed to validate the analytical models (see text for details).

Unless otherwise stated, the amplitude of the applied voltage ($A$) was adjusted to obtain a *SAR* of 10 W/kg (in particular, for the described experimental setup, this corresponds to 2.2 W). That is

$$A = \sqrt{\frac{2\rho SAR}{\sigma FB}}\, d, \tag{3.25}$$

where $d$ is the distance between the plate electrodes (84 mm). The dimensions of this setup were chosen to be large for maximizing the uniformity of the electric field at the location of the pick-up electrodes while allowing the use of the custom-made HF high-voltage amplifier (limited to 180 V, 1 A and 5 MHz). The pick-up electrodes of the implants were represented by stainless steel (SAE 317) spherical electrodes with three different diameters: 0.5 mm, 1 mm, and 1.5 mm. Each electrode was laser welded to a 5 cm piece of 32 AWG enameled copper wire.

### 3.3.1 *Absolute maximum attainable power*

To validate (3.6), the pick-up electrodes were connected to a high-precision potentiometer acting as a variable resistor (see validation circuit A. in Fig. 3.7). Before connection, the resistance of the potentiometer ($R_{\mathrm{Load}}$) was adjusted to match $R_{\mathrm{Th}}$ as provided by (3.5). Such adjustment was performed using a multimeter (38XR-A by Amprobe). After connection, the load voltage, $v_{\mathrm{Load}}(t)$, was recorded using the digital oscilloscope and max ($P_{\mathrm{Load}}$) was calculated as the square of the rms recorded voltage divided by the value of $R_{\mathrm{Load}}$, considering a time interval of 5 µs.

### 3.3.2 *Maximum unregulated dc power*

To validate (3.15) and (3.22), it was implemented a PCB with the implant circuit represented in Fig. 3.4. The diodes of the diode-bridge were Schottky diodes (RB521ZS-30 by Rohm Semiconductor). The capacitor $C$ had a capacitance of 10 µF. $R_{\mathrm{Load}}$ was again a high-

precision potentiometer acting as a variable resistor. The diode model parameters used in the analytical expressions were $V_{Diode}$ = 0.2 V and $R_{Diode}$ = 14 Ω. In the experiments reported below in which the value of $R_{Load}$ was not fixed, the expression for $P_{Load\ dc}$ was numerically maximized for obtaining the optimum $\phi$ value and hence the optimum $R_{Load}$ was found for maximum power. When the value of $R_{Load}$ was fixed, the expression for $P_{Load\ dc\ FB}$ was numerically maximized for obtaining the optimum *FB* value.

### 3.3.3 *Maximum voltage-regulated dc current*

A LDO regulator (ADP7112 by Analog Devices) adjusted to produce 3.3 V was mounted on the referred PCB to implement the implant circuit in Fig. 3.6. To study its analytical behavior, its quiescent current ($I_Q$) was set to 80 µA and its dropout voltage ($V_{Drop}$) to 30 mV. Both values are given by the manufacturer for $I_{Load}$ = 10 mA. The capacitor *C* had a capacitance of 10 µF.

## 3.4 Results

### 3.4.1 *Inter-electrode distance and electrodes diameter*

At $f$ = 5 MHz, for a *SAR* of 10 W/kg and for the properties of a saline solution that resembles the properties of muscle tissue, Fig. 3.8 displays a set of results obtained by applying the analytical expressions together with the corresponding validation results using the *in vitro* setup. In particular, the absolute maximum attainable power, max ($P_{Load}$), in Fig. 3.8a, and the maximum obtained dc (unregulated) power, max ($P_{LoadDC}$) and max ($P_{LoadDC\ FB}$), in Fig. 3.8b and in Fig. 3.8c, are represented as a function of the inter-electrode distance (*L*) and the electrodes diameter (*D*). Besides confirming the validity of the models, these results indicate that dc powers above 1 mW can be obtained in very thin (diameter < 1 mm) and short (length < 15 mm) implants. Harvested dc power is larger when the sinusoidal electric field is delivered in the form of bursts (Fig. 3.8c), than when it is delivered continuously (Fig. 3.8b).

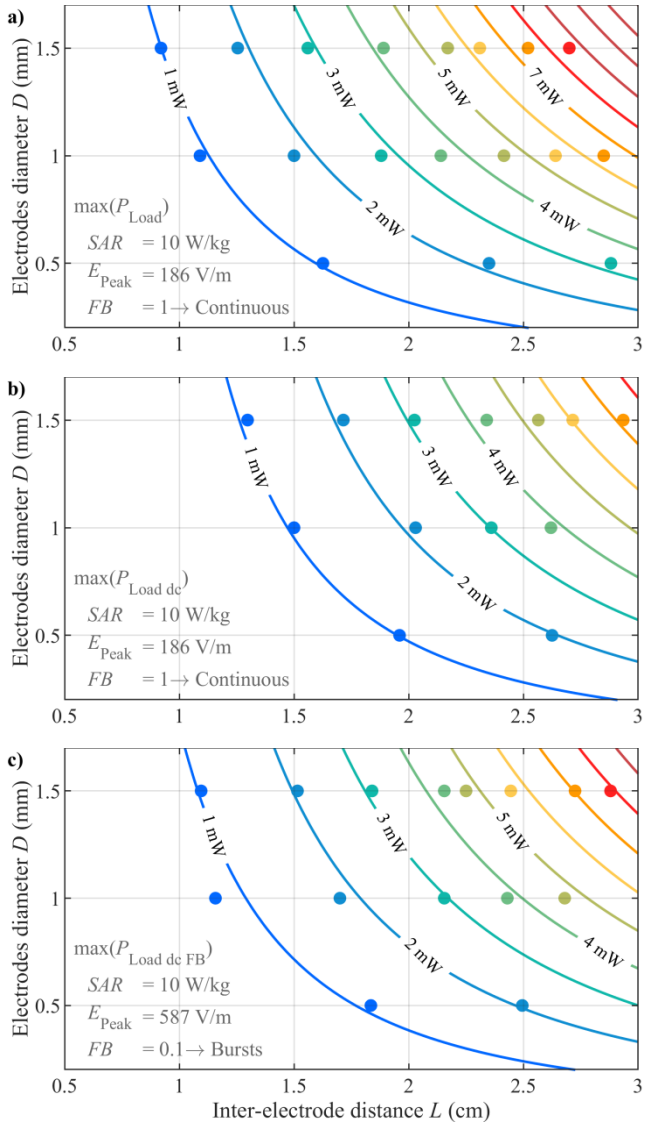


**Fig. 3.8.** Dependency of the maximum power attainable at the implant load on the electrodes diameter ($D$) and on inter-electrode distance ($L$). Conditions: $SAR$ = 10 W/kg, $f$ = 5 MHz, $\sigma$ = 0.58 S/m (0.3% NaCl) and $\rho$ = 1000 kg/m$^3$. Solid lines: results from the analytical expressions; a) (3.6), b) (3.15), c) (3.22). Circles: experimental results; **a)** using Fig. 3.7A, b) and c) the circuit represented in Fig. 3.4 a) Absolute maximum attainable power. **b)** maximum dc (unregulated) attainable power for a continuous sinusoidal field. **c)** maximum dc (unregulated) attainable power for a sinusoidal field applied in the form of bursts ($F$ = 10 kHz, $B$ = 50 µs).

However, even when the field is delivered in the form of bursts, the obtained dc power is still considerably smaller than the absolute maximum attainable power (Fig. 3.8a). This fall in performance becomes especially noticeable for short inter-electrode distances. As further stressed in the following subsections, fall in performance is more severe for short implants because the voltage picked up by the implant electrodes approaches the magnitude of the forward voltage of the rectifier diodes and hence the relative energy losses are higher.

### 3.4.2 *Dependency on the conductivity of the medium*

As (3.6) indicates, and as we *in vitro* demonstrated in [71], the absolute maximum attainable power is independent of the conductivity of the medium. Therefore, here only the dependency of max ($P_{\mathrm{LoadDC}}$) on the conductivity of the medium is inspected. In Fig. 3.9, harvested dc power is surveyed for three different NaCl solutions

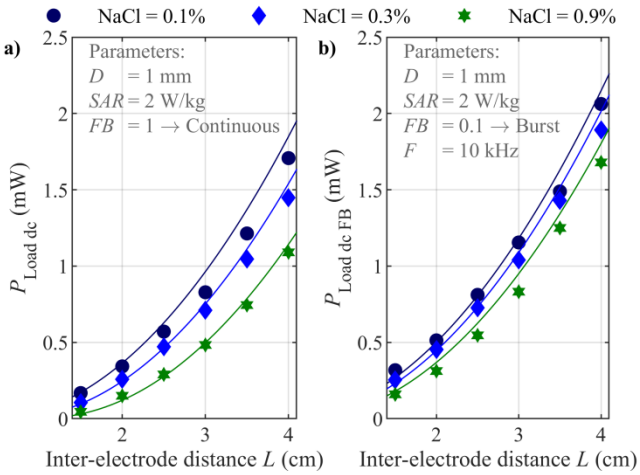


**Fig. 3.9.** Dependency of the maximum dc power attainable at the implant load on the inter-electrode distance for three different conductivities of the medium. Conditions: $SAR$ = 2 W/kg, $f$ = 5 MHz, $\sigma_1$ = 0.20 S/m (0.1% NaCl), $\sigma_2$ = 0.58 S/m (0.3% NaCl), $\sigma_3$ = 1.52 S/m (0.9% NaCl), $\rho$ = 1000 kg/m$^3$ and $D$ = 1 mm. Solid lines: results from the analytical expressions; a) (3.15) and b) (3.22). Markings: experimental results using the circuit represented in Fig. 3.4 a) Maximum dc power when the field is applied continuously. b) Maximum dc power when the field is applied in the form of bursts ($F$ = 10 kHz, $B$ = 10 µs).

with conductivities representative of those found in human tissues. In the case of a continuous field (Fig. 3.9a) it can be observed a notable dependency on the conductivity of the medium. For instance, for $L$ = 3 cm, the obtained dc power for $\sigma$ = 0.2 S/m nearly doubles that for $\sigma$ = 1.52 S/m. The main reason for this dependency is that $E_{peak}$, and hence $V_{Thpeak}$, must be reduced at higher conductivities for keeping the *SAR* value (2.8) and that causes bigger relative losses at the diodes of the full-wave rectifier. On the other hand, if the field is applied in the form of bursts (Fig. 3.9b), since $E_{peak}$, and hence $V_{Thpeak}$, can be higher for the same *SAR*, the obtained dc power is not only higher but also less dependent on the conductivity of the medium. For instance, for $L$ = 3 cm, the dc power for $\sigma$ = 0.2 S/m is only about 20% higher than that for $\sigma$ = 1.52 S/m.

### 3.4.3 *Load resistance and impedance matching*

In the two previous sub-sections it was applied the optimum $R_{Load}$ to maximize the harvested power. Since, in most scenarios, $R_{Load}$ will be a non-adjustable parameter, it is worth inspecting how the harvested power depends on it. In Fig. 3.10 it is displayed the dependency of the maximum attainable power on the value of $R_{Load}$ for the range from 200 Ω to 200 kΩ in the case of a modeled implant with $D$ = 1 mm and $L$ = 30 mm in a medium with $\sigma$ = 0.58 S/m. For these parameters $R_{Th} \approx 550$ Ω. If the voltage is not rectified, that is, if the resistive load is directly connected to the implant electrodes, the dissipated power at the load ($P_{Load\ ac}$) is maximum when $R_{Load} = R_{Th}$. That is the point at which the absolute maximum attainable power is reached. Similarly, a (lower) maximum harvested dc power is found at a $R_{Load} = R_{Load\ Opt\ dc}$ if the sinusoidal electric field is applied continuously. In both cases the obtained power decreases substantially when $R_{Load}$ is lower or higher than the optimum one.

However, if the electric field is applied in the form of bursts, the drop in harvested dc power can be mitigated, and actually reverted, for loads above $R_{LoadOptdc}$. The use of bursts intro duces an additional parameter for allowing power optimization: the duty cycle, *FB*. By reducing *FB* the loss in performance due to the increase of $R_{Load}$ can be compensated. Moreover, since by reducing *FB* the field amplitude,

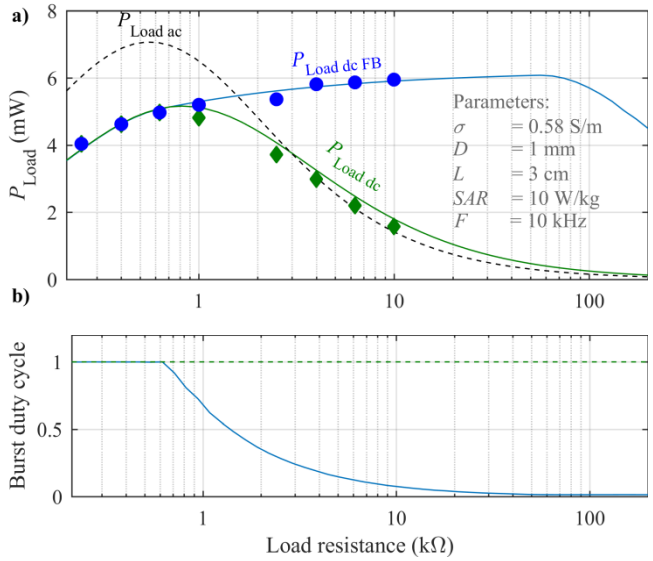


**Fig. 3.10.** a) Dependency of the maximum dc power attainable at the implant load on the value of $R_{Load}$. *Con*ditions: $SAR$ = 10 W/kg, $f$ = 5 MHz, $\sigma$ = 0.58 S/m (0.3% NaCl), $\rho$ = 1000 kg/m$^3$, $L$ = 3 cm and $D$ = 1 mm. Green trace and markings: maximum dc power for a continuous ac field (3.6). Blue trace and markings: maximum dc power for an ac field applied in the form of bursts (duty cycle optimized) (3.22). Solid lines: results from the analytical expressions. Markings: experimental results using the circuits represented in Fig. 3.4 (DC) and Fig. 3.7.A (AC). b) Optimum duty cycle, $FB$, for obtaining the results in sub Fig. 3.10a).

$E_{peak}$, can be increased for the same $SAR$ value, the losses associated with the diodes are reduced and hence the power obtained at the load is higher than that obtained for a continuous electric field at $R_{Load}$ = $R_{Load\ Opt\ dc}$. As it can be observed in Fig. 3.10, the obtained dc power reaches values (~ 6 mW) close to the absolute maximum attainable power (~ 7 mW). Nevertheless, $FB$ cannot be reduced without limit. As explained in the subsection 3.2.2 and in the appendix 3.7, $FB$ must be limited to prevent unsought stimulation. In the case illustrated in Fig. 3.10, $FB$ was limited accordingly and that causes the drop of power observable when $R_{Load}$ is larger than 57 kΩ.

### 3.4.4 *Maximum voltage-regulated dc current*

For a range of inter-electrode distances ($L \in$[0.5 cm, 5.5 cm]), Fig. 3.11 shows the maximum dc current attainable at the output of the

linear regulator (Fig. 3.6) when the ac electric field is applied in three different ways: continuously, in bursts with a constant duty cycle (*FB* = 0.2) and in bursts with a duty cycle optimized for the load seen by the diode-bridge.

For short implants it can be clearly noticed the benefit of using ac fields in the form of bursts. If a continuous ac field is employed, voltage regulator operation is impossible for implants of 2 cm or shorter whereas, for that same length, if the field is applied in the form of bursts, operation is possible and currents of 500 µA can be readily drawn by the load. In addition, the results displayed in Fig. 3.11 also illustrate the importance of optimizing the duty cycle: to obtain a current of 500 µA the minimum implant length is 1.65 cm in the case of optimum *FB* whereas such minimum length has to be increased to 2.56 cm if the constant duty cycle is used.

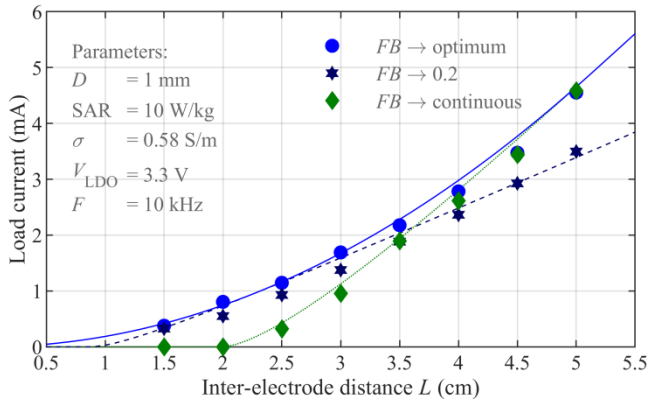


**Fig. 3.11.** Dependency of the maximum voltage-regulated (+3.3 V) dc current attainable at the implant load on the inter-electrode distance (*FB*) for three different field patterns: continuous (green), in the form of bursts with a constant duty cycle of 0.2 (dark blue) and in bursts with an optimized duty cycle (blue). Conditions: $SAR$ = 10 W/kg, $f$ = 5 MHz, $\sigma$ = 0.58 S/m (0.3% NaCl), $\rho$ = 1000 kg/m$^3$ and $D$ = 1 mm. Solid lines: results from the analytical expressions; continuous (3.14), bursts (3.21). Markings: experimental results; using the circuit represented in Fig. 3.6.

## 3.5 Discussion

As stated in Chapter 2, only in a very few occasions the use of volume conduction for powering AIMDs has been proposed and studied. And, to the best of our knowledge, no commercial AIMDs use it. The reasons why other teams are reluctant – or did not conceive – to use volume conduction for power thin and elongated implants can only be guessed.

We conjecture that the reluctance mainly arises from not recognizing two facts about volume conduction. First, large magnitude high frequency (> 1MHz) currents can safely flow through the human body if applied as short bursts. Second, to obtain a sufficient voltage drop across its two intake (pickup) electrodes, the implant can be shaped as a thin and flexible elongated body (Fig. 3.1) which is a configuration highly suitable for minimally invasive deployment through injection or catheterization.

One of the few studies in which volume conduction has been studied for powering elongated implantable devices is [65]. Although that study reinforces the main notion of this study (i.e., volume conduction can be an effective method for powering AIMDs), it must be noted that some of the results and conclusions of that study are implausibly benign according to the assumptions and results of this study. For instance, that study reports that with an interelectrode distance of only 1 mm the implant can harvest a dc voltage of 0.44 V when the *SAR* is below 1 W/kg ($f$ = 13.9 MHz, $FB$ = 1). We deem this result is implausible because a harvested dc voltage of 0.44 V by an implant placed 5 cm inside the tissues would imply $V_{\mathrm{Th}} \geq 0.44$ V which in turn would imply $E_{\mathrm{Th}} \geq 440$ V/m in its surrounding tissues. Furthermore, since volume conduction is a non-focalized WPT method, the electric field is expected to be higher in more superficial locations. Although we do not have enough information to compute the exact value of the *SAR* averaged over 10-g of tissue, the magnitude of the electric field in the implant location together with the distance between external electrodes (from 2 to 5 cm), leads us to be skeptical about the feasibility of achieving the powers reported in [65] without exceeding the limits established by international safety

standards. Another result of that study that we deem implausible is the absence of a significant impact on the obtained power by the relative angle between the external electrodes and the implant electrodes. Since the electric field direction depends on the orientation of the external electrodes, such result would imply that the obtained power is independent of α. And this, as illustrated in Fig. 3.12, is far from what our models and previous results [103] indicate: if the electric field is perpendicular to the implant then the harvested power is null.

Powering AIMDs by volume conduction requires the delivery of currents through external electrodes so that electric fields appear in the tissues where the AIMDs are located. For the sake of brevity and simplicity, the aspects related to current delivery are intentionally neglected in this study; the presence of a homogeneous electric field is assumed. We will treat these aspects in subsequent studies. However, there is an aspect worth briefly discussing now: the impact of the skin effect. In particular, at 10 MHz the current density 10 cm deep within muscles, $J_{10}$ cm, is approximately half of the current density at the surface, $J_0$; and at 100 MHz $J_{10\text{cm}} = 0.1J_0$.

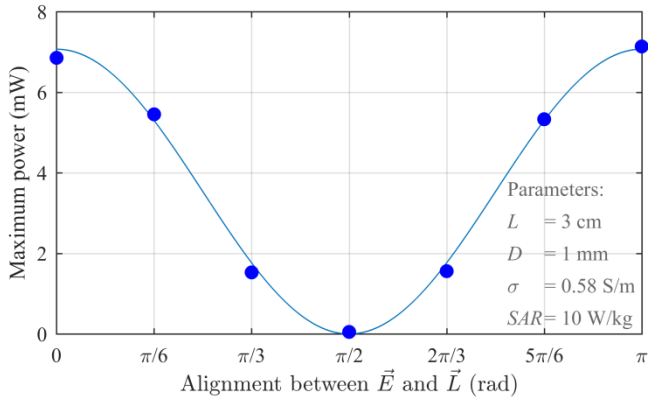


**Fig. 3.12.** Dependency of the absolute maximum power attainable at the implant load on the angle ($\alpha$) between the electric field and the implant. Conditions: $SAR$ = 10 W/kg, $f$ = 5 MHz, $FB$ = 1, $L$ = 30 mm, $D$ = 1 mm, $\sigma$ = 0.58 S/m (0.3% NaCl) and $\rho$ = 1000 kg/m$^3$. Solid lines: results from the analytical model (3.6). Circles: experimental results (the two-spheres arrangement for the implant electrodes in Fig. 3.7 was rotated with respect to the plate electrodes) using the circuit represented in Fig. 3.7a.

Therefore, it appears sensible not to use frequencies significantly above 10 MHz if it is intended to power deep seated implants. That is why we recommend the use of frequencies below 20 MHz (but above 5 MHz to prevent unsought stimulation).

Another limitation of this study is that, again for the sake of simplicity, the shape of the pick-up electrodes was restricted to spheres. This limits their surface area and hence hinders reducing $R_{Th}$. It is worth noting that, for a given electrode diameter (e.g., the maximum allowed by the lumen of a needle), larger powers than those reported here will be harvested if the electrodes are shaped as cylinders rather than as spheres since they will have a lower $R_{Th}$ [101]. Recalling from (3.3), it will imply higher power harvested.

The results obtained here show minor differences between the model and the data obtained *in vitro*. These differences are most likely due to geometrical tolerances in the *in vitro* setup, and limitations in terms of resolution and accuracy imposed by the measurement equipment.

In terms of power transfer efficiency, the specificity of the setup used in this study limits the direct comparison of the results with those obtained with other WP technologies such as inductive coupling and ultrasonic power transfer. However, it is worth noting that we envision systems with the PTE ranging from 0.01% to 1%. For instance, we performed a numerical study in which it was simulated power transfer by volume conduction to stimulation implants in an anatomically realistic leg model and we obtained a PTE of about 0.05% with an input power requirement of less than 4 W, which is low enough to grant the use of small portable rechargeable batteries [104]. Additionally, it must be noted that the results obtained here demonstrate that the maximum attainable power can be well above 1 mW and that such power is enough to supply the electronics of most AIMDs. For instance, power consumption of the electronics of a recently commercialized injectable glucose sensor (Eversense by Senseonics Inc.) is in the order of 250 µW [105].

## 3.6 Conclusion

This study supports the use of volume conduction as a safe option to power very thin and flexible AIMDs. It provides a theoretical framework for optimizing both the design of the implants and the applied electric fields used to power them. The developed analytical expressions, which are *in vitro* validated in this study, indicate that dc powers above 1 mW can be readily obtained in very thin (diameter < 1 mm) and short (length < 15 mm) implants when ac electric fields that comply with safety standards are present in the tissues where the implants are located. Other main conclusions are:

1. The obtained dc power is maximized by delivering the ac field in the form of short bursts rather than continuously.
2. The maximum attainable dc power depends on the conductivity of the medium. Such dependency is minimized by delivering the ac field in the form of short bursts rather than continuously.
3. Both the absolute maximum attainable power and the maximum attainable dc power exhibit a distinctive maximum for a specific load resistance (i.e., optimum load resistance). If the ac field is delivered in the form of bursts rather than continuously, it is possible to set the value of the optimum load resistance by adjusting the duty cycle of the bursts.

The use of volume conduction for powering AIMDs could overcome some of the limitations imposed by other technologies in terms of size and invasiveness. This would improve the deployment and usability of AIMDs in several applications such as bioelectronic medicines [106], neuro-prostheses [8] and implantable sensors [107].

## 3.7 Appendix

**Maximum field amplitude limited by unsought simulation in the case of sinusoidal electric fields applied in the form of bursts.**

The waveform obtained for this case considering a single period can be mathematically expressed as

$$E(t) = \begin{cases} E_{\text{peak}} \sin(2\pi f t), & |t| < B/2 \\ 0, & |t| \geq B/2 \end{cases} \tag{3.26}$$

where $E_{\text{peak}}$ must fulfill (2.4) to avoid tissue overheating. The complex Fourier series representation of (3.26) can be defined as

$$E(t) = \sum_{n=-\infty}^{\infty} c_n e^{in2\pi Ft}. \tag{3.27}$$

The complex Fourier coefficients of (3.27) can be determined as

$$c_n = F \int_{-B/2}^{B/2} E(t) e^{-in2\pi Ft} \, \mathrm{d}t. \tag{3.28}$$

Integrating (3.28) and applying

$$E_n = \begin{cases} \dfrac{E_{\text{peak}} FB}{2}, & Fn = f \\ 2|c_n|, & Fn \neq f \end{cases} \tag{3.29}$$

the $E_n$ magnitude of the $n^{\text{th}}$ Fourier component of the exposure field can be determined. Finally, the obtained set of $E_n$ has to fulfill (2.5) to avoid possible stimulation. In this studied case, (2.5) limits the maximum $E_{\text{peak}}$ when $FB$ tends to be much lower than 1. This fact is illustrated in Fig. 3.13. Considering a $SAR$ = 10 W/kg, $f$ = 5 MHz, $\sigma$ = 0.59 S/m, and $\rho$ = 1000 kg/m$^3$ it can be noticed that for $FB$ > 0.05 and $F$ > 100 Hz the maximum $E_{\text{peak}}$ is limited due to the $SAR$ restriction (2.7). On the other hand, when $FB$ is decreased (2.5) has

to be considered. Remarkably, considering the same *FB,* for higher *F,* higher $E_{peak}$ amplitudes can be safely applied.

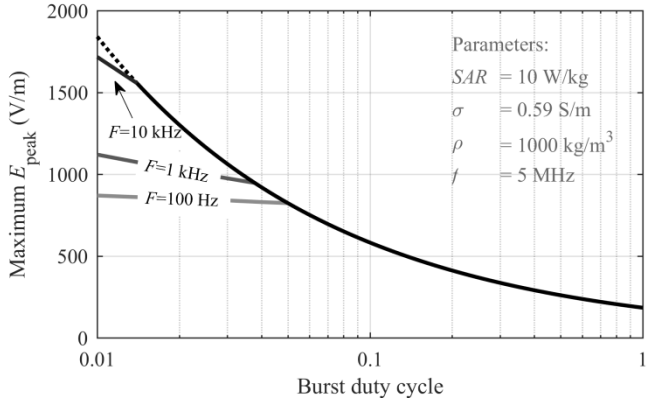


**Fig. 3.13.** Maximum $E_{peak}$ allowed for avoiding tissue overheating and stimulation. Solid lines: maximum $E_{peak}$ for $F$ = 100 Hz, $F$ = 1 kHz, and $F$ = 10 kHz. Dashed line: maximum $E_{peak}$ due to the *SAR* restriction for $F$ above 10 kHz. Conditions: *SAR* = 10 W/kg, $f$ = 5 MHz, $\sigma$ = 0.59 S/m, and $\rho$ = 1000 kg/m$^3$.

# CHAPTER 4

## TRANSMISSION LINK MODEL AND PARAMETRIC ANALYSIS

**Abstract —** The use of networks of wireless active implantable medical devices (AIMDs) could revolutionize the way that numerous severe illnesses are treated. However, the development of sub-mm AIMDs is hindered by the bulkiness and the transmission range that consolidated wireless power transfer (WPT) methods exhibit. The aim of this work is to numerically study and illustrate the potential of WPT based on volume conduction at high frequencies for powering AIMDs. In this study, the system formed by the external electrodes, the tissues and the implants were modeled as a two-port impedance network. The parameters of this model were obtained using a numerical solver based on the finite element method (fem). The model was used to determine the power delivered to the implants and the power transmission efficiency of the system. The results demonstrate that volume conduction at high frequencies can be the basis for a non-focalized WPT method that can transfer powers above milliwatts to multiple mm-sized implants (< 10 $mm^3$) placed several centimeters (> 3 cm) inside the tissues.

Parts of the contents of this chapter are adapted from the following publication:

M. Tudela-Pi, J. Minguillon, L. Becerra-Fajardo and A. Ivorra, "Volume Conduction for Powering Deeply Implanted Networks of Wireless Injectable Medical Devices: A Numerical Parametric Analysis," in IEEE Access, vol. 9, pp. 100594-100605, 2021, doi: 10.1109/ACCESS.2021.3096729.

## 4.1 Introduction

Chapter 3 presents a set of analytical models to determine the maximum power an implant can obtain by applying a uniform electric field. These models set the basis of the theoretical framework of volume conduction as a WPT method for threadlike implants. Nevertheless, these models cannot be used directly in finite geometries that include multiple tissues nor in multiple implant environments.

In this chapter, it was considered a more realistic finite scenario that includes multilayered tissues and the whole transmission link (i.e., the combination of external electrodes, multilayered tissue media, and implants) (Fig. 4.1a). In order to parametrically analyze how different geometrical and anatomical parameters influence the PDL and the PTE, the envisioned scenario (Fig. 4.1a) was simplified using a concentric cylindrical approach (Fig. 4.1b) as it has been done in previous studies in which volume conduction has been analyzed for communications [22]–[24]. Additionally, the system is modeled using a two-port network (Fig. 4.1c) instead of using an analytical approach, since an interpretable closed analytical expression is not feasible because the medium is finite and includes multiple tissue layers. The parameters of the two-port network were obtained using a fem solver.

The electrostimulation risk is not addressed as we propose the use of currents with a frequency of 6.78 MHz, which is above the 5 MHz limit. The 6.78 MHz corresponds to the central frequency of an ISM radio band, thus the possibility of interfering radiocommunications is minimized. We advise against the use of higher ISM radio bands (above 10 MHz) to avoid losses due to skin effect [108], especially in cases where the AIMDs are implanted several centimeters into the tissues

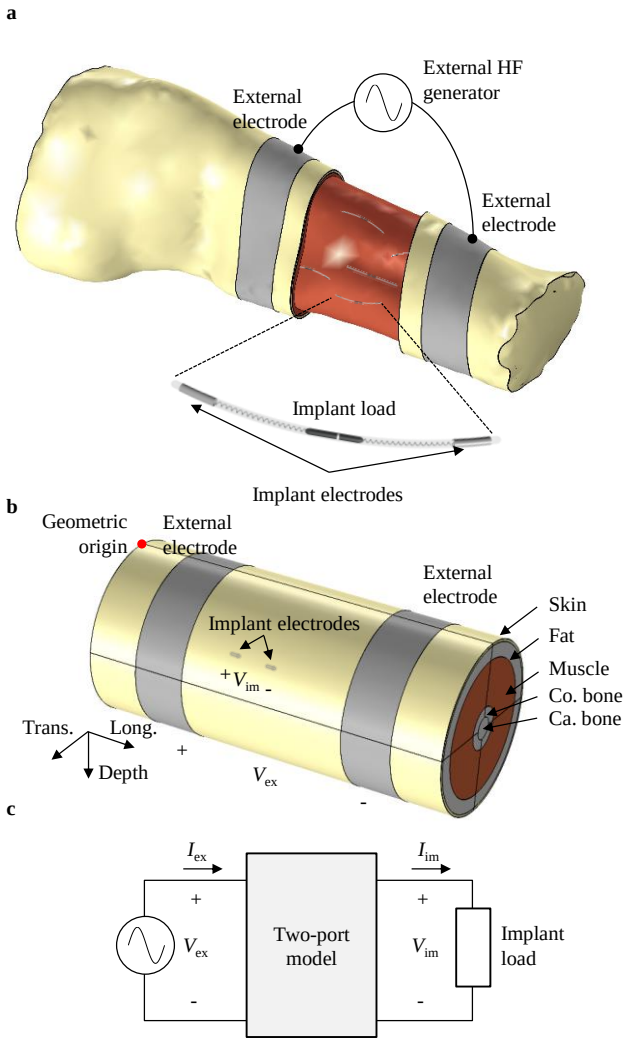


**Fig. 4.1.** a) Envisioned scenario where a swarm of threadlike AIMDs are powered using volume conduction. b) Simplified model of an upper arm that consists in a multilayered concentric cylinder (skin, fat, muscle, cortical bone, and cancellous bone), two external electrodes and two cylindrical electrodes that emulate an implant. c) Two-port network model of the coupling between the external electronic system and the implant electronics.

## 4.2 Modelling

The volume conduction links formed by the external electrodes, the upper arm tissues and the implants' electrodes were modeled using multi-port networks. The impedance parameters of these networks were obtained using a fem solver.

### 4.2.1 *Geometry*

The upper arm geometry was simplified as a five-layer concentric cylinder, as shown in Fig. 4.2, where each layer emulates a tissue: dry skin, fat, muscle, cortical bone, and cancellous bone (Fig. 4.2). Table 4.1 reports the thicknesses used for each layer.

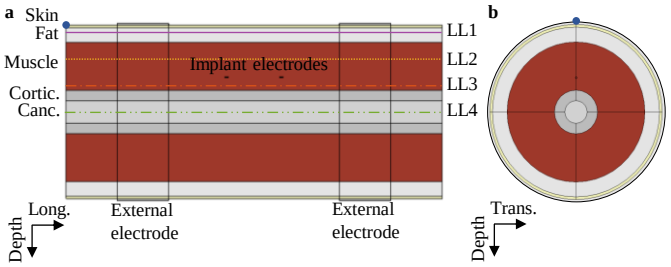


**Fig. 4.2.** Schematic views of the model. The implant electrodes (plotted in black) are placed at a depth of 30 mm and longitudinally aligned with the multilayered cylinder. a) Longitudinal mid cross section. Longitudinal lines LL1, LL2, LL3, and LL4 are located in fat (depth = 5 mm), muscle (depth = 20 mm), muscle (depth = 35 mm) and cancellous bone (depth = 50 mm) respectively. b) Transverse mid cross section.

Similar models have been broadly used to model the upper arm in galvanic coupling communication models [91], [109], [110]. Since all the tissues can be considered electrically isotropic for high frequencies [95], and the quasi-electrostatic condition is considered, each layer was electrically characterized with two scalars: conductivity ($\sigma$) and permittivity ($\varepsilon$). The electrical values of these parameters, for a frequency of 6.78 MHz, were taken from [94], while the tissue density was obtained from [111]. These parameters are reported in Table 4.2.

TABLE 4.1
MODEL NOMINAL DIMENSIONS

| Description | Value (mm) |
|---|---|
| Limb segment (multilayered cylinder) | |
| Length | 220 |
| Dry skin thickness | 1.5 |
| Fat thickness | 8.5 |
| Muscle thickness | 27.5 |
| Cortical bone thickness | 6 |
| Cancellous bone thickness | 6.5 |
| External electrodes | |
| Length | 30 |
| Inner radius | 50 |
| Electrode thickness | 1 |
| Implant electrodes | |
| Length | 2 |
| Diameter | 0.5 |
| Separation distance | 30 |

TABLE 4.2
ELECTRICAL PROPERTIES AND DENSITY OF THE MATERIALS

| Tissue/Material | Conductivity $\sigma$ (S/m) | Relative permittivity $\varepsilon_r$ | Density $\rho$ (kg/m$^3$) |
|---|---|---|---|
| Dry skin | 0.15 | 478 | 1109 |
| Fat | 0.03 | 16 | 911 |
| Muscle | 0.60 | 233 | 1090 |
| Cortical bone | 0.04 | 48 | 1908 |
| Cancellous bone | 0.12 | 90 | 1178 |
| Stainless steel | $1.4 \cdot 10^6$ | 1 | 8000 |

Although for comfort we propose, and have demonstrated, the use of external electrodes made of conductive fabric [20], in this simplified model the external electrodes consisted in a pair of cylindrical rings embracing the skin with dielectric properties and density equivalent to those of stainless steel [112]. Their dimensions are also reported in Table 4.1. Unless otherwise indicated, the separation distance between the edges of both electrodes was 100 mm and their length was 30 mm.

Regarding the elongated implant, for the sake of simplicity, it was modeled as an aligned pair of stainless-steel cylindrical electrodes separated at a given distance. Their dimensions are reported in Table 4.1. Unless otherwise stated, the implant electrodes were placed at a depth of 30 mm. They were longitudinally aligned with the multilayered cylinder, placing one electrode at the longitude of 95 mm and the other one at 135 mm. For both electrodes, the transverse position was set to zero (see Fig. 4.2).

### 4.2.2 *Multi-port networks models*

The system composed of the external electrodes, the tissues, and the implants' electrodes, is linear and reciprocal for low current densities [113]. For this reason, it can be modeled with multi-port networks. For the case of a single implant, the system can be modeled as a two-port network [114]

$$\begin{bmatrix} V_{\mathrm{ex}} \\ V_{\mathrm{im}} \end{bmatrix} = \begin{bmatrix} Z_{\mathrm{ex}} & Z_{\mathrm{exim}} \\ Z_{\mathrm{exim}} & Z_{\mathrm{im}} \end{bmatrix} \begin{bmatrix} I_{\mathrm{ex}} \\ I_{\mathrm{im}} \end{bmatrix}, \tag{4.1}$$

where $V_{\mathrm{ex}}$ ($V_{\mathrm{rms}}$) and $I_{\mathrm{ex}}$ ($A_{\mathrm{rms}}$) are the transmitter voltage and current phasors, while $V_{\mathrm{im}}$ ($V_{\mathrm{rms}}$) and $I_{\mathrm{im}}$ ($A_{\mathrm{rms}}$) are the implant voltage and current phasors, and the impedances are defined as

$$Z_{\mathrm{ex}} \stackrel{\mathrm{def}}{=} \left.\frac{V_{\mathrm{ex}}}{I_{\mathrm{ex}}}\right|_{I_{\mathrm{im}}=0}, Z_{\mathrm{im}} \stackrel{\mathrm{def}}{=} \left.\frac{V_{\mathrm{im}}}{I_{\mathrm{im}}}\right|_{I_{\mathrm{ex}}=0}, Z_{\mathrm{exim}} \stackrel{\mathrm{def}}{=} \left.\frac{V_{\mathrm{ex}}}{I_{\mathrm{im}}}\right|_{I_{\mathrm{ex}}=0}, \tag{4.2}$$

where $Z_{\mathrm{ex}}$ corresponds to the impedance between the two external electrodes, $Z_{\mathrm{im}}$ is the impedance between the implant electrodes, and $Z_{\mathrm{exim}}$ is the transimpedance between the external electrodes and the implant electrodes. For the studied frequency, the tissue impedance seen by the implant electrodes is mostly resistive due to the biological properties of the tissues (see Table 4.2). Assuming a purely resistive $Z_{\mathrm{im}}$, the maximum power is transferred to the load when the implant load ($R_{\mathrm{L}}$) matches $Z_{\mathrm{im}}$. For this reason, $R_{\mathrm{L}}$ was set to be equal to the real part of $Z_{\mathrm{im}}$. Consequently, the implant current was defined as

$$I_{\mathrm{im}} = -\frac{V_{\mathrm{im}}}{R_{\mathrm{L}}}. \tag{4.3}$$

For the cases in which two implants were considered, the two-port model (4.1) was expanded to a multiport model

$$\begin{bmatrix} V_{\mathrm{ex}} \\ V_{\mathrm{im1}} \\ V_{\mathrm{im2}} \end{bmatrix} = \begin{bmatrix} Z_{\mathrm{ex}} & Z_{\mathrm{exim1}} & Z_{\mathrm{exim2}} \\ Z_{\mathrm{exim1}} & Z_{\mathrm{im1}} & Z_{\mathrm{im1im2}} \\ Z_{\mathrm{exim2}} & Z_{\mathrm{im1im2}} & Z_{\mathrm{im2}} \end{bmatrix} \begin{bmatrix} I_{\mathrm{ex}} \\ I_{\mathrm{im1}} \\ I_{\mathrm{im2}} \end{bmatrix}, \tag{4.4}$$

where

$$Z_{\mathrm{im1im2}} \stackrel{\mathrm{def}}{=} \left.\frac{V_{\mathrm{im2}}}{I_{\mathrm{im1}}}\right|_{I_{\mathrm{im2=0}}, I_{\mathrm{iex=0}}}. \tag{4.5}$$

### 4.2.3 *Extraction multi-port networks parameters*

For the described scenario, the quasi-static electric field approach can be assumed, since for a frequency of 6.78 MHz, the electric field wavelength is much larger than the model dimensions.

The model geometry described in Fig. 4.2 was implemented in COMSOL Multiphysics 5.3 (from COMSOL, Inc., Burlington, MA, US) to calculate the electric field distributions and the parameters of the multi-port network models using the “Electric Currents (ec)” physics from the “AC/DC module”. This physics mode considers the quasistatic approach and solves the following equations

$$\nabla \cdot \boldsymbol{J} = -\frac{\partial \rho_{\mathrm{c}}}{\partial t}, \tag{4.6}$$

where $J$ is the current density (A/m$^2$) and $\rho_{\mathrm{c}}$ is the charge density (C/m$^3$),

$$\boldsymbol{J} = \sigma \boldsymbol{E} + i\omega \boldsymbol{D}, \tag{4.7}$$

being $\omega$ the angular frequency of the field (rad/s), and $D$ the electric displacement field (C/m$^2$),

$$\boldsymbol{D} = \varepsilon_0 \varepsilon_r \boldsymbol{E} \tag{4.8}$$

and

$$\boldsymbol{E} = -\nabla V_{\mathrm{rms}}. \tag{4.9}$$

The used mesh consisted of two tetrahedral meshes. The first one was applied in the regions close to the implant electrodes (< 5 mm from their centers), imposing a maximum edge length of 0.1 mm. This refined mesh was used to obtain a proper resolution and therefore accurate impedance values for the implant electrodes. The second one comprises the rest of the geometry and was automatically generated. The total number of elements was comprised between 1,000,000 and 1,200,000.

The multi-port impedance parameters were extracted simulating the delivery of a known current ($f$ = 6.78 MHz) through the selected electrodes and measuring the received voltage at the electrodes of interest, see (4.2). To calculate the averaged SAR, the normalized values of the simulated $E_{\mathrm{rms}}$ and $\sigma$ were stored in a regular 3-D grid (steps of 1 mm) for the whole geometry. Then, using MATLAB R2019a (from MathWorks, Inc., Natick, MA, US), the local SAR (2.7) was averaged over cubes with a volume of ~10 $\mathrm{cm}^3$ (edge equal to 21 mm and an approximately mass of 10-g) for each of the grid points. The peripheral points that could not be the center of a cube, as the cube included points outside the tissues, were assigned to the highest spatial-averaged value in which they were enclosed as indicated by an IEEE guide [115].

### 4.2.4 *PDL and PTE*

The power delivered to the implant load can be calculated as

$$PDL = \frac{|V_{\mathrm{im}}|^2}{R_{\mathrm{L}}}. \tag{4.10}$$

The active power ($P_{\mathrm{in}}$) coupled to the tissues by the external electrodes is calculated as

$$P_{\text{in}} = I_{\text{ex}} V_{\text{ex}} cos(\varphi), \tag{4.11}$$

where φ is the phase (rad) between Vex and Iex. As most of the power is dissipated at the tissues and as will be seen, only a tiny portion can be dissipated at the implants, the applied power (4.11) can be approximated as

$$P_{\text{in}} \approx I_{\text{ex}}^2 \mathbb{R}(Z_{\text{ex}}). \tag{4.12}$$

Therefore, the active power transfer efficiency (PTE) is calculated as

$$PTE = \frac{\sum_{m=1}^{N} PDL_{\text{m}}}{P_{\text{in}}}, \tag{4.13}$$

where *N* is the total number of implants.

## 4.3 Results

### 4.3.1 *Electric field inside the tissues*

The amplitude of the external HF current that can be coupled to the tissues is limited by the SAR restrictions. For the nominal model of Table 4.1, it was found that the applied current must be below 0.46 $A_{rms}$ (at 6.78 MHz), since above this value, the local averaged SAR will overpass the limitation of 20 W/kg. If not otherwise indicated, this value will be the applied current for the following cases. Fig. 4.3 shows the averaged *SAR* distribution when the external electrodes apply 0.46 $A_{rms}$ at 6.78 MHz. The results highlight that the averaged SAR is focused close to the external electrodes and has a maximum value of 20 W/kg.

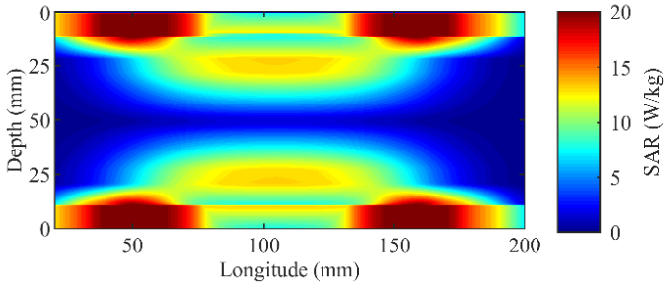


**Fig. 4.3.** Distribution of SAR averaged over a 10-g cube (longitudinal mid cross section). The current applied between both external electrodes was 0.46 $A_{rms}$. The maximum SAR was located close to both external electrodes (20 W/kg).

Fig. 4.4a shows the electric field distribution along four longitudinal lines at the depths: 5 mm, 20 mm, 35 mm, and 50 mm (see Fig. 4.2a). The maximum electric field is located close to both external electrodes (see LL1, which runs through the middle of the fat layer). However, it can be observed how the electric field tends to be uniform a few centimeters away from the external electrodes. Considering the most central segment of the model (i.e., longitudes between 95 mm and 125 mm) the electric field can be considered depth-independent (e.g., at a depth of 50 mm the electric field is just 1.5% lower than at a depth of 5 mm, for the entire range). The electric field at mid distance between the external electrodes (i.e., longitude position equal to 110 mm) is of about 155 $V_{rms}$/m. Considering an implant with a length of 30 mm and aligned parallel to the applied electric field, the voltage that this implant can pick up is 4.65 $V_{rms}$ (see Fig. 4.4b). It is worth noting that, although this will be the maximum rms amplitude because of the SAR limitation, it will be possible to obtain much higher peak amplitudes by delivering the ac currents in the form of short bursts [116], [117].

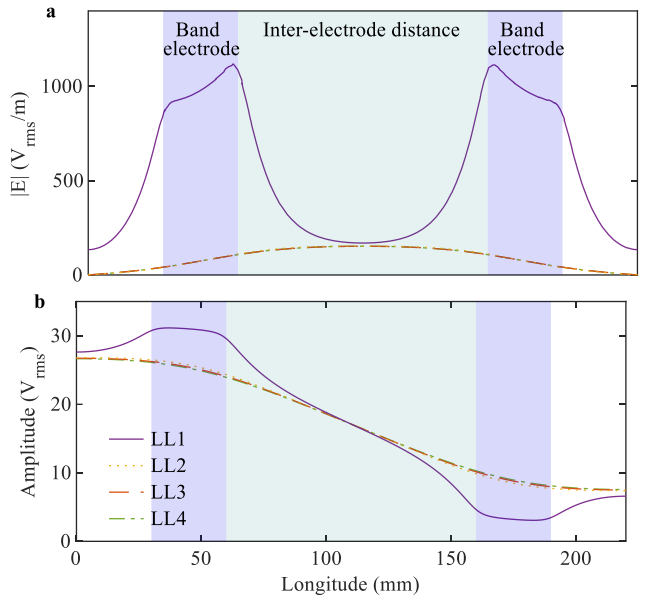


**Fig. 4.4. (a)** Electric field (rms) and (**b)** rms voltage distribution along four longitudinal lines (see Fig. 4.2a). LL1: depth = 5 mm (Fat), LL2: depth = 20 mm (Muscle), LL3: depth = 35 mm (Muscle), and LL4: depth = 50 mm (Cancellous bone).

### 4.3.2 *Implantation depth*

To study the *PDL* and *PTE* as a function of the implantation depth, the longitudinal position of the implant electrodes was set to 95 mm and 125 mm respectively while the transverse position was zero for both electrodes. The electrodes' depth position was swept from the peripheral fat layer (depth = 3 mm) to the cancellous bone (depth = 50 mm), see Fig. 4.5.

The results show that the maximum *PDL* is obtained when the implant electrodes are surrounded by muscle tissue. This maximum value is obtained for a depth of 22 mm and has a value of 11.8 mW and its *PTE* is 0.07%. The lowest PDL is obtained when the implant is surrounded by fat tissue (*PDL* = 0.4 mW, *PTE* = 0.004%, and depth = 7 mm). This difference in the PDL between different layers is mostly related to the tissue impedance seen by the implant electrodes. At a depth of 5 mm (i.e., fat tissue) the tissue impedance seen by the implant electrodes ($Z_{im}$) is 8612-1262i Ω, while for a depth of 25 mm (i.e., muscle tissue) is 464-50i Ω. As the maximum power is transferred to the load approximately when RL matches the

real part of $Z_{im}$, $Z_{im}$ directly affects the obtained *PDL* (4.10). Nevertheless, the obtained *PDL* as a function of the depth is hardly affected by the maximum voltage that an implant can pick up, since as Fig. 4.2b highlights, for the studied area, the maximum voltage that an implant could receive is not related to its implantation depth.

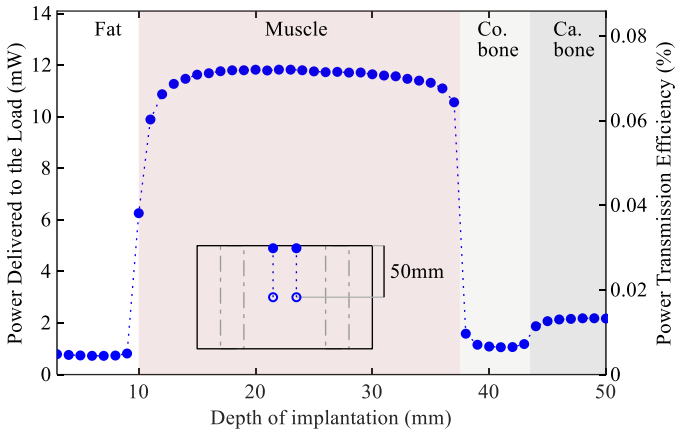


**Fig. 4.5.** *PDL* and *PTE* as a function of the implantation depth. Co. bone: Cortical bone, Ca. bone: Cancellous bone. The inlet shows the electrodes displacement.

### 4.3.3 *External electrodes separation*

Fig. 4.6 illustrates the influence of the separation distance between the inner edges of the external electrodes. In this figure the implant electrodes were kept at the default position (i.e., an implantation depth of 30 mm, a transverse position of 0 mm, and a longitudinal position of 95 mm for the first electrode and 135 mm for the second one), while the separation distance between the external electrodes was symmetrically increased from 30 mm to 120 mm. The amplitude of the applied current was adjusted to obtain a *SAR* of 20 W/kg, resulting in a current amplitude of 0.46 $A_{rms}$ for the entire range studied. The results show that the picked up *PDL* is reduced when the external electrodes are aligned over the implant electrodes (i.e., a separation distance of 30 mm regarding the depth axis), as the electric field $\boldsymbol{E}$ is focused on the more superficial layers (see Fig. 4.4a). In this case, the implant picked up 2.8 mW with a *PTE* of 0.03%. The results illustrate that *PDL* increases with the separation distance of the external electrodes. The maximum power transferred is for the

case where the external electrodes were separated 120 mm. For this case, the *PDL* is 11.6 mW and the *PTE* is 0.068%. On the other hand, the *PTE* has its maximum (0.072%) for a separation of 90 mm.

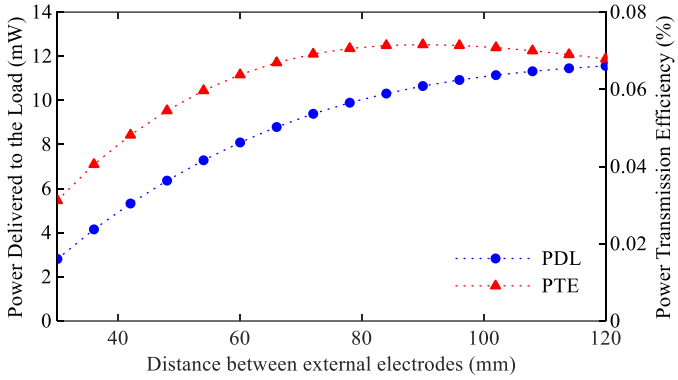


**Fig. 4.6.** PDL and PTE as a function of the separation distance between edges of the external electrodes.

### 4.3.4 *External electrodes width*

To determine the influence of the width of the external electrodes, their size was swept from 10 mm to 35 mm (Fig. 4.7) while the separation distance between the edges of the electrodes was kept constant at 100 mm. The current applied for each band size was set to obtain a maximum averaged SAR of 20 W/kg (Fig. 4.7a) ranging from 0.345 $A_{rms}$ to 0.49 $A_{rms}$. The results show that as the band electrodes get wider, the *PDL* and *PTE* obtained are also higher (Fig. 4.7b).

### 4.3.5 *Fat thickness*

One of the anatomical parameters of the model that varies more between individuals is the fat thickness [118]. To study how the fat thickness can influence in the *PDL* and the *PTE*, the thickness of this layer was swept from 1 mm to 25 mm, while the thicknesses of the

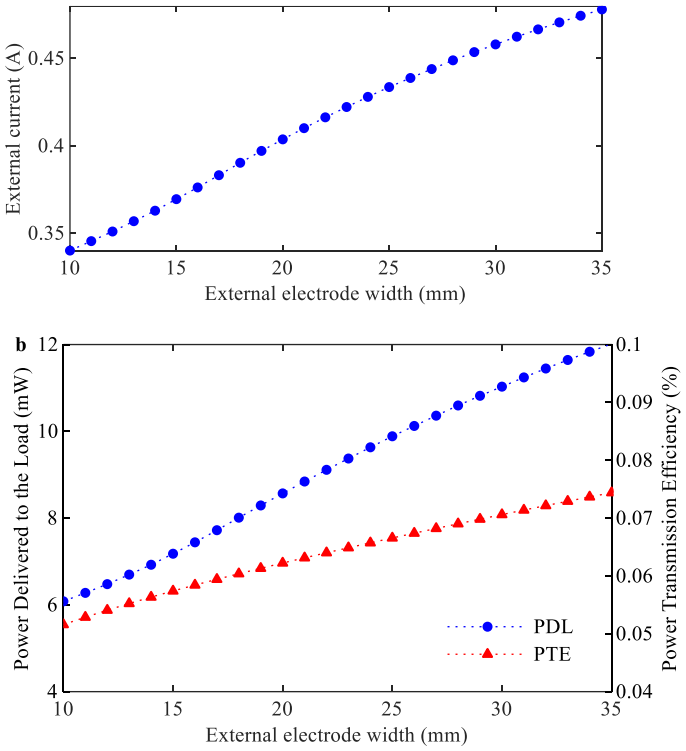


**Fig. 4.7 (a)** Admissible external current to produce a maximum averaged SAR of 20 W/kg. (**b)** PDL and PTE as a function of the external electrode width.

dry skin, cancellous bone and cortical bone were kept constant, and the muscle thickness was modified to obtain a total radius of 50 mm (i.e., the limb radius was kept constant to allow the comparison between cases). Again, the external current $I_{ex}$ was set to obtain a maximum averaged SAR of 20 W/kg (Fig. 8a) ranging from 0.34 $A_{rms}$ to 0.69 $A_{rms}$.

The results indicate that to avoid tissue over-heating, the applied $I_{ex}$ must be reduced as the fat thickness is increased (Fig. 4.8a). Interestingly, the results show that as the fat layer gets thicker, the power that an implant placed in the muscle can obtain is higher (Fig. 4.8b). The minimum *PDL* value corresponds to a 5 mm fat layer (*PDL* = 10.6 mW, and *PTE* = 0.067%).

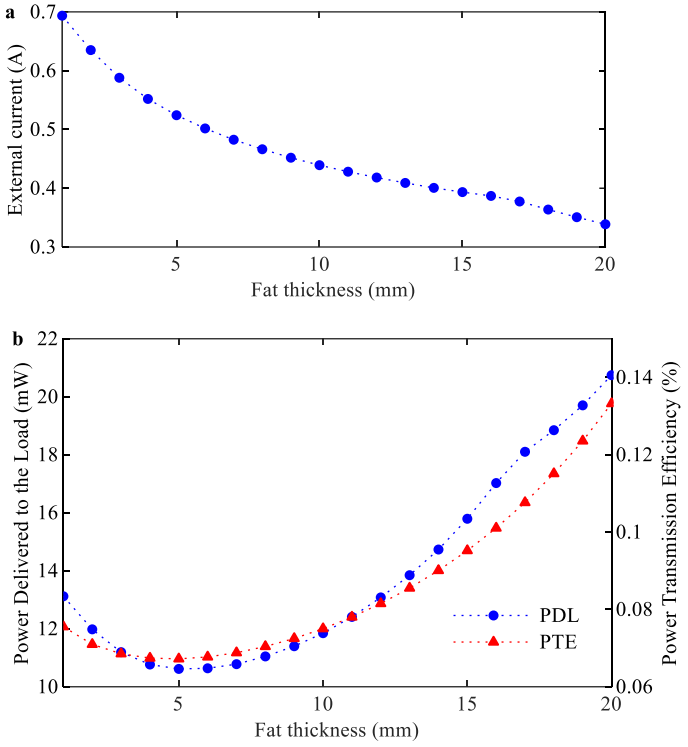


**Fig. 4.8. (a)** Admissible external current to produce a maximum averaged SAR of 20 W/kg. **(b**) PDL and PTE as a function of the fat layer thickness imposing a SAR of 20 W/kg.

### 4.3.6 *Interaction of multiple implants*

To determine how neighboring implants may influence the *PDL* of each individual implant, a parametric sub-analysis was performed varying the separation distance of two parallel implants along two different axes independently. In this sub-analysis it was assumed a minimum separation distance of 3 mm between both parallel devices due to implantation limitations. In this sub-analysis it was also assumed that the load of both implants corresponds to the real part of $Z_{im}$.

In Fig. 4.9a a longitudinal displacement was done while fixing the length of both implants to 30 mm. The position of the Implant 1 was kept constant, while the Implant 2 was longitudinally displaced along

an axis 3 mm more superficial. The longitudinal displacement of the left electrode of the Implant 2 was swept from 45 mm to 145 mm. During this displacement, the implantation depth of both electrodes of Implant 2 was kept constant at 27 mm and their transverse position was 0 mm (see inlet Fig. 4.9a).

In the second case, Fig. 4.9b, the displacement was done with respect to the implantation depth. Here, the location of Implant 1 was kept constant at a depth of 30 mm, while the depth position of Implant 2 was swept from 3 mm to 27 mm (i.e., 3 mm away from Implant 1), keeping the transverse position equal to zero, and both electrodes aligned parallel to the electrodes of Implant 1 regarding the longitudinal axis (see inlet in Fig. 4.9b).

The results presented in Fig. 4.9 show that the *PDL* moderately decreases for both implants as the separation distance between electrodes is reduced. For instance, the *PDL* obtained by Implant 1 when the electrodes of both implants are placed parallel at a depth separation of 3 mm is 9.5 mW (i.e., a reduction of 19.5% compared to the single implant case, see Fig. 4.5b). However, this power reduction becomes less than 10% for depth separations above 10.5 mm. In the same way, when two electrodes of different implants are placed consecutively regarding the longitudinal axis (e.g., a longitudinal separation of ± 30 mm regarding the left electrodes, and a depth separation of 3 mm, see Fig. 4.9a) the obtained power is also reduced in this case, the *PDL* is reduced 11% compared to the single implant case (Fig. 4.5b). (It must be noted that the substantial *PDL* decreases observed in Fig. 4.9 for large longitudinal separations and in Fig. 4.9b for large depth separations are not due to the interaction between the implants but to the non-uniformity of the electric field and to the change of tissue type respectively).

### 4.3.7 *Fibrous capsule around the implant*

The presence of an artificial implant within the human body will trigger physiological reactions that will end up producing a fibrous tissue capsule around the device, even if the implanted device is

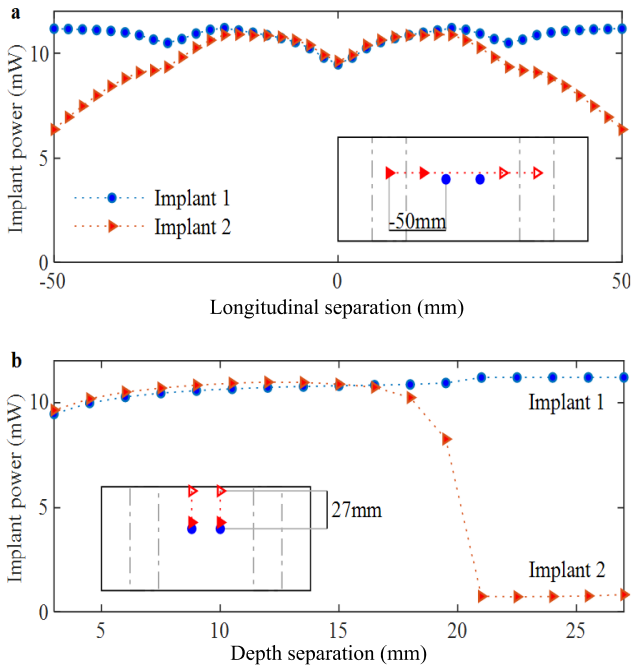


**Fig. 4.9.** PDL as a function of the distance between two 30 mm length implants. (**a**) Longitudinal displacement. Regarding the left electrodes of both implants the longitudinal displacement was from -50 mm to +50 mm (see inlet Fig. 4.9a). (**b**) Displacement regarding the depth position. Both implants were parallel aligned regarding the longitudinal axis. The displacement between implants was from 3 mm to 27 mm regarding the depth axis (see inlet Fig. 4.9b).

considered to be biocompatible [119]. In the systems considered here, this encapsulation will modify the tissue impedance seen by the implants, and therefore the *PDL*. The two main factors that will contribute to the impedance change will be the capsule conductivity and the capsule thickness.

A sub-analysis was conducted to analyze the potential impact of the encapsulation. The conductivity of the fibrous tissue can be considered mostly frequency independent and in [120] the authors found that the conductivity of the fibrotic capsule formed around silicon rubber had a value around $0.16 \pm 0.1$ S/m. Thus, here we assumed a fibrotic conductivity of 0.16 S/m. The implant electrodes were positioned at the default location of Table 4.1, within muscle

tissue. The modeled thicknesses of the fibrotic capsule ranged from 0.1 to 1 mm.

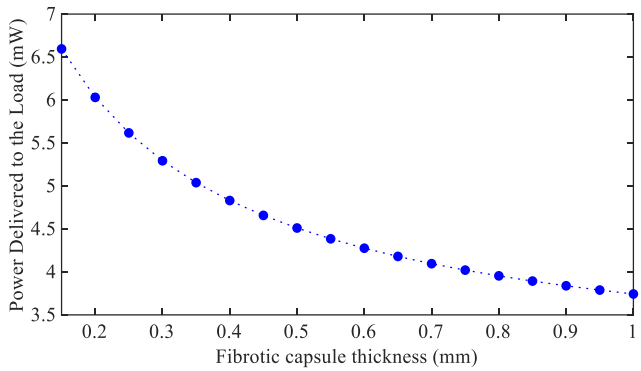


**Fig. 4.10.** *PDL* as a function of the thickness of a fibrotic capsule. The fibrotic tissue conductivity was set to 0.16 S/m.

The results presented in Fig. 4.10 show that, for the described scenario, a capsule of just 0.1 mm substantially reduces the maximum power that the implant could pick up; the *PDL* drops from 11.6 mW (Fig. 4.5) to 6.6 mW. Interestingly, the rate of *PDL* drop decreases with the thickness and for a tenfold thickness, 1 mm, the *PDL* (3.7 mW) is still considerably high.

### 4.3.8 *Implant electrode size*

The size of the implant electrodes has a direct effect on the impedance across them (i.e., $Z_{im}$) [116]. To study their contribution to the *PDL* and *PTE*, the length of the implant electrodes was changed from 1 mm to 3.5 mm for two different electrode diameters (0.5 mm and 0.25 mm), while the separation distance between electrodes was kept constant. The results show that for the studied range the *PTE* depends linearly on the *PDL*, and confirm that as in [116] the power is maximized by increasing the size of the implant electrodes (Fig. 4.11).

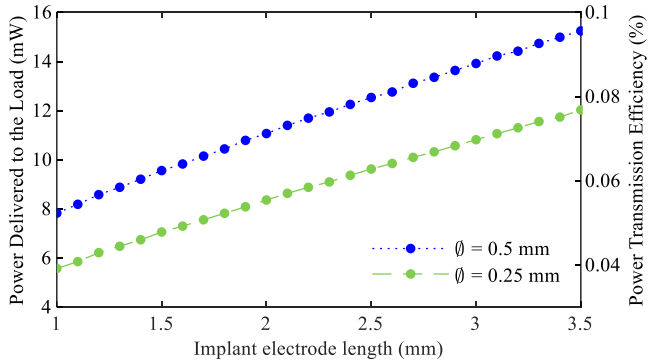


**Fig. 4.11.** *PDL* and *PTE* as a function of the implant electrode length for two different electrode diameters: 0.5 mm and 0.25 mm.

### 4.3.9 *Radius of the modeled limb*

The radius of the limbs varies within the population [121]. In Fig. 4.12 the radius of the multilayered concentric cylinder was swept from 40 mm to 60 mm, while the thicknesses of the layers were scaled to preserve the proportions of Table 4.1. The implant was placed at a depth equivalent to half of the cylinder's radius, the transverse position was zero, the longitude of the implant was 30 mm, and the longitudinal position of its electrodes was 95 mm and 135 mm (i.e., centered regarding the inter-electrode region). The applied current was limited to obtain a maximum SAR of 20 W/kg (Fig. 4.12a) ranging from 0.34 $A_{rms}$ to 0.58 $A_{rms}$.

The results show, that both *PDL* and *PTE* decrease as the multilayered cylinder radius increases (Fig. 4.12b). The *PDL* for a radius of 60 mm is 8.3 mW (i.e., a reduction of 48% compared to the 40 mm case), and the *PTE* for the 60 mm case is 0.046% (i.e., a reduction of 69% compared to the 40 mm case).

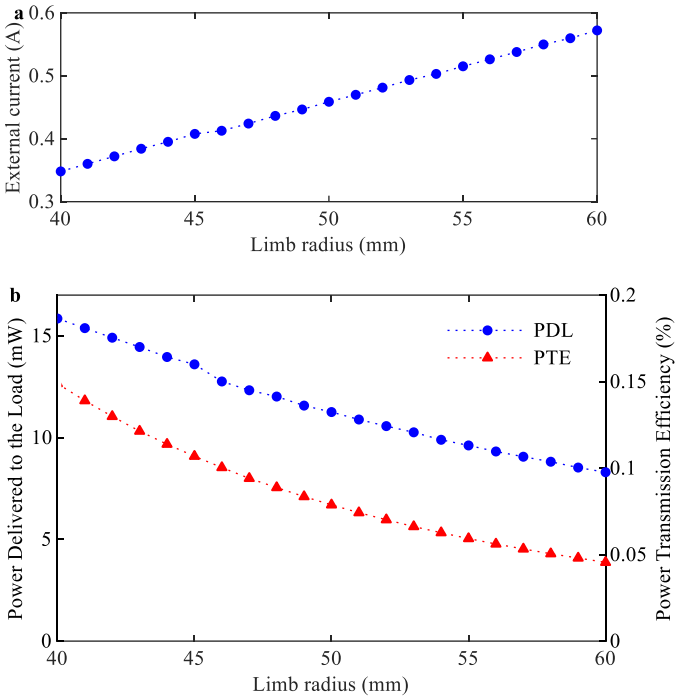


**Fig. 4.12. (a)** Maximum external current that can be applied to obtain an averaged SAR of 20 W/kg. **(b)** *PDL* and *PTE* as a function of the radius of the limb. The thicknesses of the layers were scaled with the limb radius to preserve the proportion of Table 4.1.

## 4.4 Discussion

The numerical results obtained here indicate that the proposed WPT technique based on volume conduction can be considered to be a proper method to power networks of deeply implanted AIMDs at the limbs. This claim is supported by three pieces of evidence presented here. First, powers above 10 mW can be obtained with threadlike thin and elongated implants (e.g., diameter equal to 500 µm and length 30 mm), while the externally applied currents comply with safety limitations (i.e., SAR $\leq$ 20 W/kg for extremities, and a frequency above 5 MHz). This obtained power is orders of magnitude higher than the power required for most existing AIMDs [122]. Second, the generated electric field is coarsely uniform within the region encompassed by the external electrodes. Thus, the maximum voltage

that the implants can receive is almost independent on their implantation depth; deeply implanted devices can be powered. Third, the presence of multiple implants placed just a few millimeters apart has a minor impact on their *PDL*, while it increases the *PTE* of the system.

An unanticipated and counterintuitive finding is that as the fat layer becomes thicker, the power picked up by the implant placed at the muscle tissue becomes higher. This is attributable to two main reasons. First, fat tissue is more insulating than the underlying muscle tissue and this enables safe delivery of higher currents: a thicker fat layer around the external electrodes (i.e., lower conductivity than the muscle layer) reduces the edge effect of the external electrodes, making it possible to increase the applied external current. Second, the increase in thickness of the fat layer at the expense of the muscle layer causes that more current will flow through the muscle, increasing the electric field within this layer. Therefore, the *PDL* of the implants increases.

In this study, for the sake of simplicity and because the waveform of the applied current does not influence the PDL (for the case where the implant load is a purely resistive load [116]) the applied external current was considered purely sinusoidal. However, by applying the external currents in the form of short bursts, the peak voltage that an implant can obtain using volume conduction can be increased. This is relevant for most electronic implants, and particularly for digital implants, as these devices will typically require a minimum voltage to operate. By delivering the ac current in the form of bursts rather than continuously the received peak voltage can be increased without incrementing the complexity of the implant's electronics (i.e., in most of the scenarios, the implant circuit will not require bulky boost converters). Regarding the safety limitations, if the current bursts are applied with a repetition frequency $F$ (Hz) of tens of Hertz, and the burst has a duration $B$ (s), (2.7) becomes

$$\mathrm{SAR} = \frac{\sigma F B \left|\boldsymbol{E}_{\mathrm{peak}}\right|^2}{\rho}. \tag{4.14}$$

However, it must be considered that, by delivering the current in the form of bursts rather than continuously, the field is no longer purely sinusoidal. It must be verified that the low frequency components of the modulation harmonics cannot produce undesired stimulation [123].

Another interesting result is that even considering a capsule formation with a thickness of 1 mm around the implant electrodes (i.e., twice the diameter of the considered electrode), the implant would be able to harvest powers above 3.7 mW for the studied geometry. However, it must be mentioned that although in this study it was used a fibrotic tissue conductivity of 0.16 S/m, which is the most used in the literature [120], the electrical properties of the fibrotic tissue are not clearly determined [124], [125]. Therefore, the electrical properties and growth of the fibrotic capsule are key features to study in future long term *in vivo* studies.

In this work, the size of the implant was intentionally kept constant. This is due to the fact that the separation distance between the implant electrodes and the dimensions of the electrodes were deeply studied in [116]. Considering that the implant electrodes are part of a flexible tubing that includes the implant electronics, if the diameter of this tubing coincides with the electrodes' diameter (500 µm), the volume of the AIMDs would be 6.5 $mm^3$. The small size of the implants combined with their threadlike shape will allow their percutaneous injection. However, previous *in vivo* studies we conducted [126] emphasized the relevance of inserting the whole implant into the target muscle. Otherwise, the implant may fail due to mechanical stress. Due to the difficulty and in many cases the impossibility of repairing a damaged implant, we are currently developing and mechanically validating new robust and resilient [127] implant encapsulations.

Table 4.3 benchmarks the obtained results against state-of-the-art deeply placed ($\geq 3$ cm) AIMDs. This comparison highlights the potential of the proposed technique to obtain high power densities (i.e., *PDL* per implant volume).

TABLE 4.3
BENCHMARKING OF DEEPLY PLACED AIMDS

| | This work | Zhang [128] | Zada [129] | Meng [130] | Agrawal [48] |
|---|---|---|---|---|---|
| WPT method | VC | IC | MW | US | MW |
| Study type | *in silico* | *ex vivo* | *in vitro* | *in vitro* | *in vivo* |
| Implantation depth (mm) | 30 | 50 | 45 | 30 | 42 |
| Implant volume ($mm^3$) | 6.7 | 1140 | 21‡ | 1‡ | 12 |
| Implant section ($mm^2$) | 0.2 | 900 | 42 | 1.3 | 1.77 |
| PDL (mW) | 11.6 | 1.5 | 4.7 | 2 | 0.45 |
| PDL/Volume ($mW/mm^3$) | 1.73 | 0.001 | 0.22‡ | 2‡ | 0.04 |

VC: Volume Conduction. IC: Inductive Coupling. MW: Microwave. US: Ultrasounds. ‡ Only includes the volume of the energy pick-up element. The volume will be increased by attaching a functional AIMD circuitry.

Regarding the external electrodes the results show that to power deeply implanted devices (e.g., depth above 10 mm) it is preferable a separation distance considerably larger than the length of the implant (assuming that the implant is placed in the central region between both external electrodes). However, if this separation distance is too large, the *PTE* is reduced because, as the separation distance between the external electrodes increases, more power is dissipated through the tissues, while the *PDL* remains almost constant. Another noteworthy observation related to the external electrodes is that wider external electrodes allow the application of higher external electric currents, thereby increasing the *PDL*. The results show that for a wider electrode, $Z_{ex}$ is reduced, and consequently, the *PTE* improves. Nevertheless, the width of the band electrodes is obviously limited by the available space in the limbs.

## 4.5 Conclusions

In this study it is numerically demonstrated that the proposed WPT technique based on volume conduction can be a safe and effective method for powering electronic devices deeply implanted within human limbs. Powers above 10 mW can be obtained by thin (diameter < 1 mm) threadlike implants, which can be easily

implanted using minimally invasive procedures such as percutaneous injections.

The results show that the maximum *PDL* and *PTE* are mostly related to the tissue impedance as measured across the implant electrodes ($Z_{im}$). The main feature that affects this impedance, apart from the implant electrode size [116], is the kind of tissue that surrounds the implant: the PDL ranges from 10.4 mW in muscle tissue to 0.4 mW in fat tissue. Other features that affect *PDL* and *PTE* are the size and location of the external electrodes. Larger external electrodes allow the application of higher external currents, increasing the *PDL*. Additionally, to maximize the *PTE* in deeply implanted devices, the external electrodes must have a separation distance moderately larger than the implant's length. The geometrical dimensions and the tissue anatomy of the limbs also contribute to the *PDL* and *PTE*. In this way, the fact of having a fat layer above 10 mm significantly increases the *PDL* for an implant placed inside muscle tissue. Furthermore, as the diameter of the modeled limb increases, the *PDL* and *PTE* are decreased. Nevertheless, it is worth noting that transferred powers of several mW were obtained in all the cases reported here.

It must be acknowledged that although tens of milliwatts can be safety transferred using the proposed WPT technique, the *PTE* of this method is considerably lower compared to the *PTE* of focalized WPT methods (e.g., inductive coupling). However, it also must be acknowledged that the proposed WPT technique is a non-focalized method and that the implants do not interfere substantially in terms of power extraction if they are spaced few millimeters away. Therefore, the proposed WPT technique can be particularly suitable to power distributed networks of minimally invasive implants.

# CHAPTER 5

## IN HUMAN VALIDATION OF VOLUME CONDUCTION AS A WIRELESS POWER TRANSFER METHOD

**Abstract —**Aiming at miniaturization, wireless power transfer (WPT) is frequently used in biomedical electronic implants as an alternative to batteries. However, WPT methods in use still require integrating bulky parts within the receiver, thus hindering the development of devices implantable by minimally invasive procedures, particularly when powers above 1 mW are required in deep locations. In this regard, WPT based on volume conduction of high frequency currents is an advantageous alternative relatively unexplored, and never demonstrated in humans. We describe an experimental study in which ac and dc electric powers in the order of milliwatts are obtained from pairs of needle electrodes (diameter = 0.4 mm, separation = 30 mm) inserted into the arms or lower legs of five healthy participants while innocuous and imperceptible high frequency (6.78 MHz) currents are delivered through two textile electrodes strapped around the considered limb. In addition, we demonstrate a procedure to model WPT based on volume conduction which characterizes coupling between the transmitters and the receivers by means of two-port impedance models which are generated from participants' medical images.

Parts of the contents of this chapter are adapted from the following preprint publication:

J. Minguillon, M. Tudela-Pi, L. Becerra-Fajardo, E. Perera-Bel, A. J. del-Ama, A. Gil-Aguado, A. Megía-García, A. García-Moreno, A. Ivorra, "Powering electronic implants by high frequency volume conduction: in human validation," *bioRxiv*, 2021.03.15.435404; doi: https://doi.org/10.1101/2021.03.15.435404

## 5.1 Introduction

Chapter 4 introduced a parametric model validated *in silico* considering a simple cylindrical geometry. In this chapter, this proposed model is validated in human volunteers. Furthermore, this chapter also details the procedure followed to obtain the multiport model parameters from participants' medical images (MRI) by using finite element methods. This procedure is not only relevant for the design of systems using WPT based on volume conduction, but it could also be applied for modeling transmission channels in intrabody communications based on volume conduction.

This chapter also describes how large magnitude HF currents can be innocuously and imperceptibly applied to humans and how part of those currents can be picked up by a pair of thin intramuscular electrodes separated a very few centimeters to power a digital circuit. The innocuity of the applied currents is ensured by adhering to available international safety standards for human exposure to electromagnetic fields [131], [132]. In this study, the IEEE standard [131] was followed. The frequency of the applied sinusoidal currents (modulated as bursts) was set to 6.78 MHz because it corresponds to the central frequency of a designated ISM band [133], thus minimizing the possibility of interfering radiocommunication systems, and because it is high enough to easily avoid risks related to unsought electrostimulation. Briefly, five volunteers evaluated the use of volume conduction as a WPT method. Two intramuscular commercial electrodes were inserted in each participant's upper limb and calf while an HF electric field was coupled to the tissues using two-band electrodes (see Fig. 5.1). The complete procedure is detailed in the subsection 5.2.2.

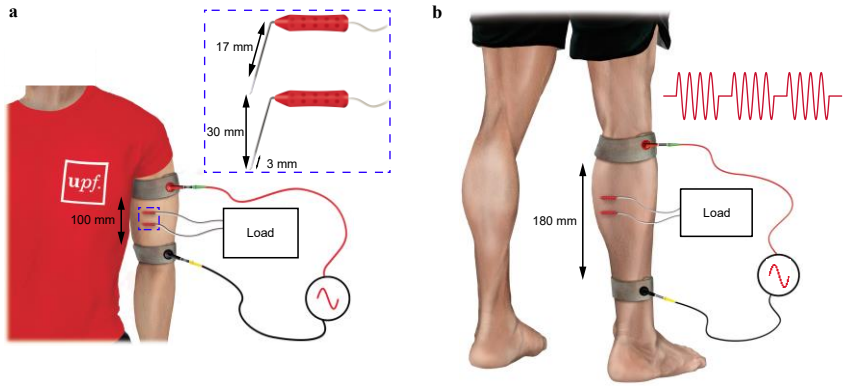


**Fig. 5.1.** Experimental setups employed in the present study. (**a)** Upper limb (arm) experimental setup: an external electrical load (resistive) is connected to a pair of needle electrodes inserted into the brachial biceps. **(b)** Lower limb (lower leg) experimental setup.

## 5.2 Methods

### 5.2.1 *Participants*

Five young (age range from 21 to 38 years) healthy volunteers participated in the study: P1 (female), P2 (female), P3 (female), P4 (male) and P5 (male). They were recruited through a call for participation sent by email to colleagues and were not paid for their participation. Before starting the experimental procedure, they were provided with oral and written information regarding the study (including risks, benefits, and data protection aspects) and signed an informed consent form. The study was conducted in the National Hospital for Paraplegics in Toledo (Spain). The experimental protocol was approved by the Ethics Committee for Clinical Investigation of the Complejo Hospitalario de Toledo (December 5, 2019; reference number: 467).

### 5.2.2 *Experimental procedures*

The experimental procedures were divided into two phases: 1) magnetic resonance imaging (MRI) images acquisition and 2) assays.

During the first phase, MRI images were acquired of the non-dominant upper (arm) and lower (leg) limb of each participant. These

images were used to build 3D computational models for numerical calculations (see subsection 5.2.10). Prior to MRI acquisition, the planned locations for the external and for the intramuscular electrodes were marked by drawing crosses using a permanent ink marker. Then, MRI fiducial markers (PinPoint® for Small Field of View Imaging 187 from Beekley Corporation, Bristol, CT, US) were placed over the marks. Two MRI markers were used for the needle electrodes per participant and limb (i.e., one per needle) and three for each band. The position of the participants during MRI acquisition was the same as that during the second phase of the experimental procedures. Once all the participants finished the first phase, they sequentially participated in the second phase.

During the second phase, different procedures and assays were conducted. First, the participant was positioned on a stretcher (supine and prone positions for arm and lower leg, respectively) and instructed to avoid unnecessary movements. A pair of external electrodes was strapped around the corresponding limb. As control, another pair of electrodes was strapped around the contralateral limb for later discerning whether skin alterations could be due to the delivery of the HF currents or were caused by the materials of the electrodes. These external electrodes consisted in textile bands with a width of 3 cm (used for arms) or 4 cm (used for lower legs) and were made of conductive fabric.

The electrodes on the non-dominant limb were connected to a HF voltage generator (i.e., an arbitrary waveform generator (4065 from B&K Precision, Yorba Linda, CA, US) connected to a custom-made class AB amplifier). Sinusoidal voltage bursts (carrier frequency of 6.78 MHz and $FB = 0.1$; where $F = 1$ kHz is the repetition frequency of the bursts and $B = 100$ μs is their duration) of different amplitudes (increasing order) were applied to check if the participant perceived some discomfort. Once the preliminary assay was performed (without any notification of sensations by any of the participants), a pair of intramuscular needle electrodes were inserted either into the brachial biceps or into the medial gastrocnemius of the non-dominant limb for the arm and lower leg, respectively, under aseptic conditions. These needle electrodes had a diameter of 0.4 mm and a length of

20 mm of which only the distal 17.5 mm were inserted (i.e., an implantation depth of 17.5 mm). The needle has a 3 mm long exposed surface on its tip (530607 from Inomed Medizintechnik GmbH, Emmendingen, Germany; see inlet Fig. 1b). The needle electrodes were connected to a discrete potentiometer (3683S-1-202L from Bourns Inc., Riverside, CA, US) using short cables (maximum of 12 cm) to avoid inductive and capacitive wiring effects. After that, the remaining assays (i.e., maximum transferable power, and screen power-up, and, in one case, temperature evolution in 18 minutes) were conducted. Once the last assay was finished, the textile electrodes were unstrapped, the needle electrodes were extracted and the skin areas where the electrodes had been located were inspected. No damage was observed in these areas or in the electrodes. Only one case (arm of P2) presented small-sized superficial hematomas in the areas where the needle electrodes had been inserted approximately one hour after the extraction.

The temperature of the limb was monitored using a thermal imaging infrared camera (E60 from FLIR Systems Ltd) during the entire phase. The second phase was repeated for the other limb. The order of the limbs was randomized among the participants.

### 5.2.3 *MRI acquisition and segmentation*

Each participant underwent MRI images acquisition, recording four sequences per limb: T1 axial (slice resolution = 0.52 x 0.52 mm; slice thickness = 6 mm), T1 sagittal (slice resolution = 1.04 x 1.04 mm; slice thickness = 4.8 mm), T1 coronal (slice resolution = 1.04 x 1.04 mm; slice thickness = 4.65 mm), and T2 axial (slice resolution = 0.52 x 0.52 mm; slice thickness = 6 mm). These sequences were acquired with a 3 Tesla system (Magnetom Trio, a Tim System from Siemens Healthcare GmbH). Four different tissues were segmented: 1) bone, which included cortical and trabecular tissues, bone marrow, and articular cartilages (e.g., meniscus), 2) muscle, including tendons, ligaments, and intramuscular fat, 3) subcutaneous fat, and 4) skin.

For the segmentation of bone, muscle and fat, the procedure started by manually segmenting the T1 axial acquisition every other slice.

The initial segmentation of the skin had to be performed using a different procedure since it was not visible in the entire MRI stack because of its thinness. The skin thickness was approximated by measuring it in different slices of the MRI, and then the skin was generated by performing a 2D axial dilation on the fat segmentation.

The measured skin thicknesses are reported in Table 5.1. For each tissue, the remaining slices were interpolated with the "3D interpolation" built-in tool of The Medical Imaging Interaction Toolkit from the German Cancer Research Center, Heidelberg, Germany. This interpolation was based on the radial basis function interpolation [134] and on Laplacian smoothing [135]. Minor manual adjustments were required to correct sharp curvatures of the geometry in the interpolated slices. Finally, smoothed surface meshes were generated from the 3D interpolation (see Fig. 5.2) and then exported for numerical computation. The MRI fiducial markers centers were precisely annotated.

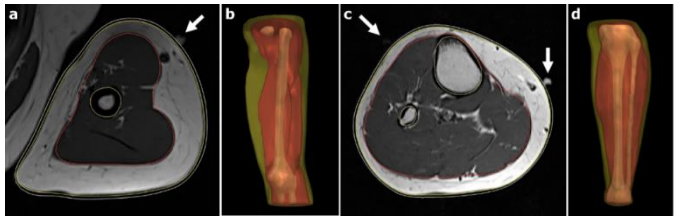


**Fig. 5.2.** Examples of smoothed surface meshes and markers position from MRI images. White arrows indicate the MRI markers for electrode placement. **(a)** Axial slice of arm. **(b)** 3D representation of segmented arm. **(c)** Axial slice of lower leg. **(d)** 3D representation of segmented lower leg. Bone mesh in brown, muscle in red, fat in yellow, and skin in white (only in (a) and (c)).

TABLE 5.1.
Measured skin thickness from MRI images for each participant and limb

| Skin thickness (mm) | P1 | P2 | P3 | P4 | P5 |
|---|---|---|---|---|---|
| Arm | 1.75 | 1.50 | 1.50 | 2.00 | 1.75 |
| Leg | 1.50 | 2.00 | 1.75 | 2.00 | 2.25 |

### 5.2.4 *Maximum transferable power*

The maximum received power for an optimal resistive load was obtained. For that, first, sinusoidal voltage bursts (carrier frequency of 6.78 MHz and $FB$ = 0.1 ($F$ = 1 kHz)) were applied across the external electrodes and the optimal load (i.e., the resistance that provides maximum power transfer) was experimentally found by adjusting the resistance of the discrete potentiometer. Then, with the optimal load connected to the intramuscular electrodes and the same voltage waveform applied across the external electrodes, different amplitudes were applied. The externally applied voltage, the external current, and the voltage at the load ($V_{\mathrm{Load}}$) were measured. As was stated on Chapter 3, for each amplitude, the received power at the load was computed as

$$\begin{aligned} P_{\mathrm{load}} &= \frac{V_{\mathrm{load\ rms}}^2}{R_{\mathrm{load}}} \\ &= \frac{V_{\mathrm{load}}^2}{R_{\mathrm{load}}} k^2 FB, \end{aligned} \tag{5.1}$$

where $R_{\mathrm{load}}$ is the optimal load and the scaling factor $k\sqrt{FB}$, with $k = \sqrt{11/32}$, transforms amplitude values into RMS values for the applied waveform (see appendix 5.6 for details of the applied waveform). The average channel efficiency was also computed as the ratio between the received power and the externally applied power.

### 5.2.5 *Screen power-up assay*

To illustrate the potential of volume conduction to power complex digital implants, a demonstrative circuit was designed and manufactured using commercial off-the-shelf components (Fig. 5.3). This electronic device was connected to the needle electrodes. The main function of this circuit was to show its input voltage and current by means of a 1.3” LCD screen (LS013B7DH05 from Sharp Corporation Sakai, Osaka Prefecture, Japan).

The electronic device is composed of three subcircuits: 1) power stage, 2) sensing stage and 3) control unit and display. The power stage consists of a dc-blocking capacitor for each electrode, followed

by a bridge rectifier (diode MCL103B from Vishay Intertechnology, Malvern, PA, US), a smoothing capacitor (10 µF) that rectifies the picked-up high frequency voltage, and a linear voltage regulator (TLV701 from Texas Instruments, Dallas, TX, US) that fixes a voltage of 3.3 V (Fig. 5.3a).

The sensing stage is used to measure the input dc voltage and current. The voltage is measured across the smoothing capacitor that follows the diode bridge. The current is measured by acquiring the voltage drop across a shunt resistor (30 Ω) located after the smoothing capacitor of the regulator's output. This voltage is amplified using two amplification stages (implemented with operational amplifiers TLV521 from Texas Instruments, Dallas, TX, US) that set a gain of 51 V/V. The voltages are digitized using two 8-bit analog-to-digital converters (ADS7040 from Texas Instruments, Dallas, TX, US). The result of the conversions is obtained by the control unit through a serial peripheral interface (SPI).

The control unit is based on an 8-bit, low-power microcontroller (PIC18LF47K42 from Microchip Technology Inc., Chandler, AZ, US) with a clock frequency set to 1 MHz. The microcontroller interrogates the ADCs every 10 ms and then updates the LCD screen (via SPI communication) with the acquired measurement. Both current (mA) and voltage (V) are shown on the screen with a resolution of 0.1 mA and 0.1 V, respectively (Fig. 5.3c).

Approximately every 20 s the microcontroller refreshes the LCD and changes the logo that the LCD shows on its top. Two different logos can be displayed. Since the main purpose of this device was to show the potential of volume conduction to power complex digital circuits, the circuit was designed to minimize its power consumption at the expense of the measurement accuracy.

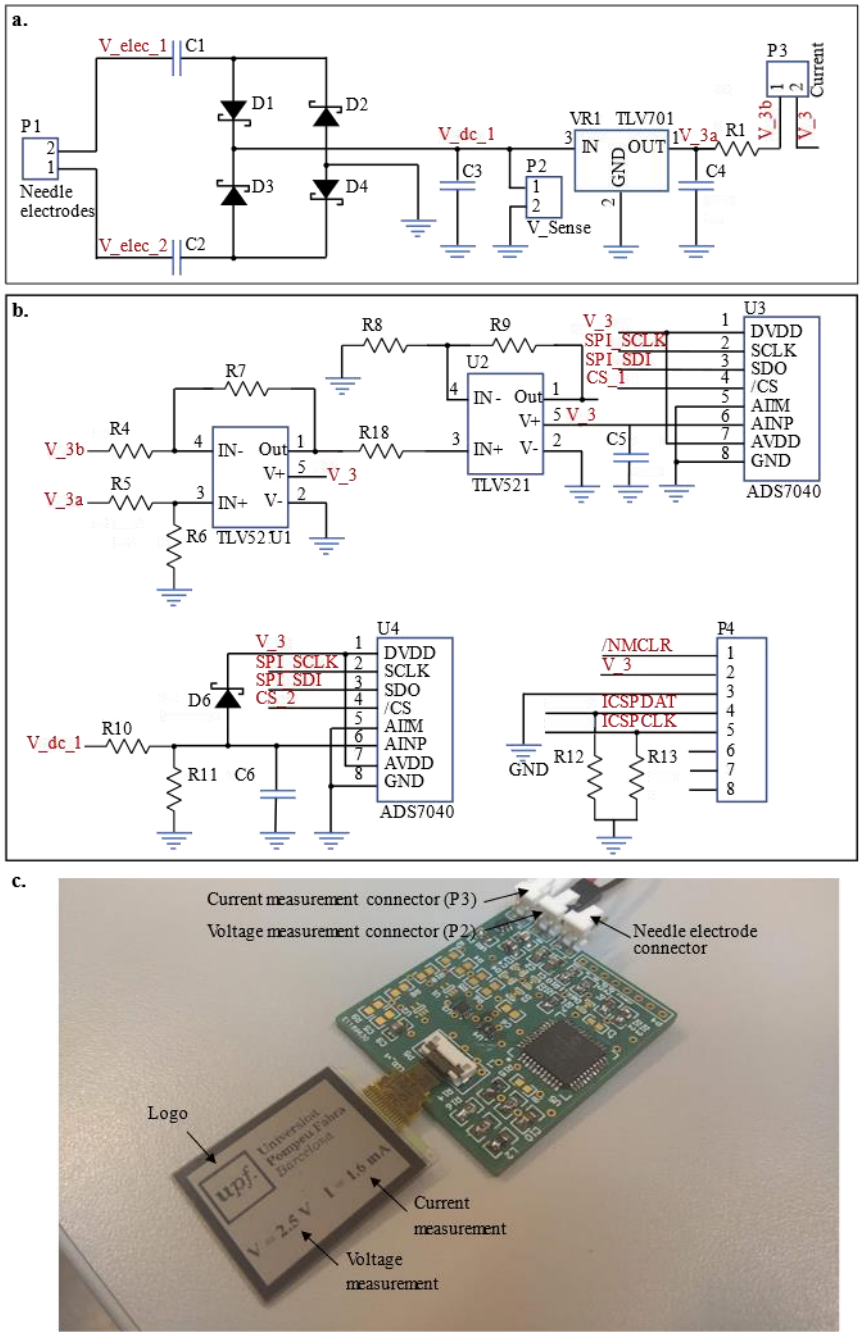


**Fig. 5.3.** Schematic and picture of the digital demonstrative circuit. (**a**) Power stage of the digital circuit. (**b**) Sensing components of the designed circuit. (**c**) Picture of the electronic device.

That is the reason why the voltage and the current to calculate the power consumption were externally measured through the two 2-pin connectors P2 and P3 using the multimeters mentioned in the subsection 5.2.9. The electronic components were mounted on a 45 × 40 mm two-layers PCB (see Fig. 5.3c). The base material is FR-4 and its thickness is 1.55 mm. The device has a power consumption of approximately 1 mW, this device is comparable to the electronics of most implantable electronic devices, and far above in terms of power consumption to that of pacemakers, which is in the order of 10 μW [74].

The assay consisted in finding out the required external voltage amplitude to power-up the electronic device. With the same external HF voltage waveform as above (carrier frequency of 6.78 MHz and $FB = 0.1$ ($F = 1$ kHz)), the external amplitude was increased until the screen powered-up and displayed information. Both the externally applied voltage and current were measured. In addition, the dc voltage and the dc current were measured at the load. In one case (lower leg of P4), for illustrating the capability of the proposed approach to power multiple devices, a second identical device was connected to an additional pair of electrodes inserted in the lateral gastrocnemius of the same limb.

### 5.2.6 *Temperature evolution in 18 minutes*

In one case (lower limb of P4), the same external HF voltage waveform as above (carrier frequency of 6.78 MHz and $FB = 0.1$ ($F = 1$ kHz)) with fixed amplitude (the same as for powering-up the screen) was uninterruptedly applied for 18 minutes. This was performed once the intramuscular electrodes had been extracted. With the participant seated in a chair, the temperature variations were monitored and recorded using the infrared camera. The contralateral limb was used as control: external electrodes were strapped around the lower leg, but no voltage was applied.

### 5.2.7 *Perception of heat-related and electrical-stimulation-related sensations*

During the second phase of the experimental procedures, self-perception of heat-related (HR) and electrical-stimulation-related (ESR) sensations was monitored. In particular, the participants were asked for oral notification of any HR or ESR sensation at any time without knowing when the HF voltage bursts were applied. In case of sensation, the HR perception was classified into three intensity levels (1-Not sure, 2-Pleasant warmth and 3-Unpleasant warmth) and the ESR perception was classified into three intensity levels (1-Not sure, 2-Pleasant sensation and 3-Unpleasant sensation) and five categories (1-Tingling, 2-Puncture, 3-Pressure, 4-Pain and 5-Other).

### 5.2.8 *Electrical safety*

As was stated in Chapter 2, the electrostimulation risks are especially relevant for low frequencies (< 100 kHz). However, if the sinusoidal currents are applied in the form of bursts, the generated low frequency harmonics must be considered [136]. In this study, sinusoidal voltage bursts (carrier frequency of 6.78 MHz and $FB = 0.1$ ($F = 1$ kHz)) were applied. To minimize the contribution of the generated low frequency harmonics, the applied bursts were smoothed with a tapered cosine window (with $r = 0.5$, see Appendix 5.6 for details of the applied waveform).

Applying the expression for non-sinusoidal fields established in the safety standard to the used voltage waveform, the maximum peak electric field that can be applied (i.e., the maximum in situ electric field to avoid electrostimulation) is above 200 MV/m (see Appendix 5.6). This limit is far above the electric field amplitudes that were computed to be produced during the experimental sessions.

Regarding the risk of thermal damage, in the case of limbs, the IEEE standard indicates that the maximum admissible SAR is 20 W/kg, space-averaged over any cubical 10-g of tissue and time-averaged for 6 minutes [131].

To ensure that the SAR restriction was met during the experimentation, the external voltages were applied for short time exposures (i.e., < 30 seconds). On the other hand, the SAR values indicated in section 5.3 correspond to projected SAR values for exposures longer than 6 minutes. That is, the electric field magnitudes obtained with the 3D computational models (see subsection 5.2.10) were used to compute the SAR that would be produced by sinusoidal voltage bursts continuously applied for 6 minutes or more. In all cases, the projected whole-body SAR was below this limit (i.e., 0.4 W/kg) for exposures longer than 1 hour.

### 5.2.9 *Measurement apparatus*

The electrical ac measurements were acquired using a floating digital oscilloscope (TPS2014 from Tektronix, Inc., Beaverton, OR, US). For the applied external voltage and the potentiometer voltage, active differential probes (TA043 from Pico Technology Ltd, Saint Neots, UK) were used. A current probe (TCP2020A from Tektronix, Inc., Beaverton, OR, US) was used for the applied external current (i.e., current corresponding to the applied external voltage). This is shown in Fig. 5.4a. The electrical dc measurements (i.e., voltage and current to calculate the power consumption of the demonstrative electronic device connected as load to the needle electrodes) were acquired using two multimeters (38XR-A from Amprobe, Everett, WA, US): one to measure voltage and another one to measure current. This is shown in Fig. 5.4b.

### 5.2.10 *Numerical methods*

The segmented meshes (from the MRI images) of the tissues were imported into COMSOL Multiphysics 5.3 (from COMSOL, Inc., Burlington, MA, US) to create the 3D computational model. To numerically determine the electric field and voltage distributions inside the tissues, the “electric current” physics that is included inside

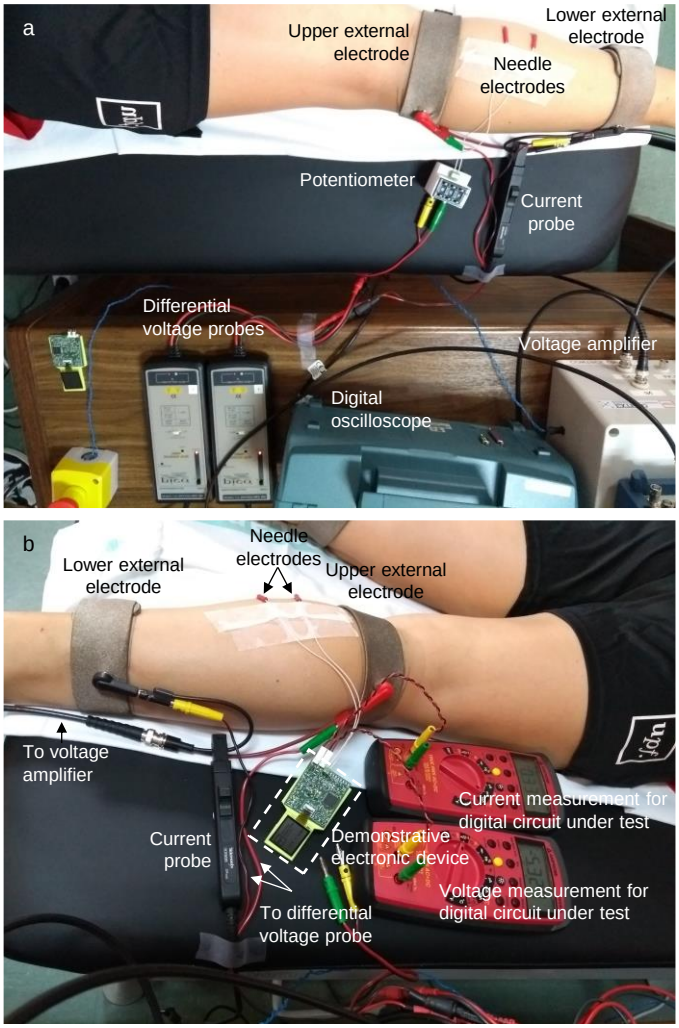


**Fig. 5.4.** Measurement apparatus. (a) Experimental ac measurement setup. (b) Experimental dc measurement setup.

the ac/dc module of COMSOL Multiphysics 5.3 was used. The geometry of each one of the ten studied 3D computational models consisted in a four-tissue layered segmented limb obtained from the MRI images. The four layers, from the most peripheral to the most internal one were: skin, fat, muscle, and cancellous bone. The passive electrical properties and densities of the tissues are reported in Table 5.2.

TABLE 5.2.
Passive electrical properties and density of modeled tissues at a frequency of 6.78 MHz [137]

| Dielectric properties @ 6.78MHz | Conductivity (S/m) | Relative permittivity | Density ($kg/m^3$) |
|---|---|---|---|
| Skin | 0.147 | 478 | 1109 |
| Fat (subcutaneous) | 0.0496 | 35 | 911 |
| Muscle | 0.602 | 233 | 1090 |
| Bone (cancellous) | 0.116 | 90 | 1178 |

Two cylindrical electrodes with a diameter of 0.4 mm, and a total length of 20 mm emulated the needle electrodes that we used in the experimental part. Their length was divided into two longitudinal sections: 17 mm of insulating material and 3 mm of exposed surface at the tip of the needle. The position of these electrodes was determined using the coordinates of the MRI markers. They were perpendicularly aligned with the skin tissue and were inserted 17.5 mm inside the tissues. The position coordinates of the external electrodes were also identified in the MRI using three markers per electrode. These data were used to obtain a three-point plane. Following, a plane parallel to the previous one was created with a separation distance of 30 mm for the arms and 40 mm for the calf (i.e., the width of the band electrodes used during the experimentation). Then, the superficial tissue area encompassed between both planes was considered the area of the external electrodes. Finally, the whole limb was set inside a block that emulated the air. The size of this block was adjusted for each case to guarantee a minimum of 2 cm gap of air in any direction. The density and electrical properties of non-biological materials are reported in Table 5.3. Fig. 5.5 shows the resultant geometry of the 3D computational model of the arm of participant P5.

The electrical coupling between the external electrodes and the needle electrodes was modeled as a two-port network. This model included the external electrodes, the limb tissues, and the needle electrodes (emulated as cylinders). Since all its elements were passive, the system could be considered reciprocal [138].

TABLE 5.3.
Electrical properties of non-biological materials

| Dielectric properties | Conductivity (S/m) | Relative permittivity | Density ($kg/m^3$) |
|---|---|---|---|
| Conductive electrodes (Steel, 0.65% carbon) [139] | $5.5 \cdot 10^{6}$ | 1 | 7844 |
| Insulating material of needle electrodes [140] | $1 \cdot 10^{-17}$ | 3.2 | 1000 |
| Air (at 20º) | $1 \cdot 10^{-9}$ | 1 | 1.2 |

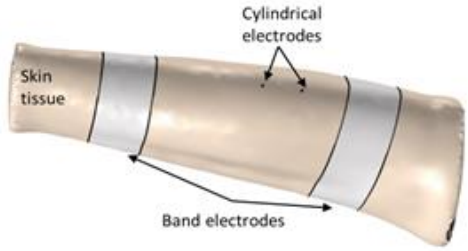


**Fig. 5.5.** Geometry of the 3D computational model (COMSOL) of the arm of P5. The air box that surrounded the arm has been intentionally hidden for visualization purposes.

Therefore, voltages and currents at the network could be expressed as in (4.1). Where $V_{ex}$ is the voltage across the external electrodes, $V_{in}$ is the voltage across the needle electrodes, $I_{ex}$ is the current through the two external electrodes and $I_{in}$ is the current through the needle electrodes. The impedances $Z_{ex}$ and $Z_{12}$ were determined by simulating the delivery of a reference current (1 A at 6.78 MHz) through the external electrodes, while keeping $I_{in}$ equal to 0, and measuring the voltage across the external electrodes (for $Z_{ex}$) and the voltage across the needle electrodes (for $Z_{12}$). The same procedure was done for determining $Z_{in}$ but, in this case, applying a reference current through the needle electrodes and measuring the voltage across the needle electrodes.

The parameters obtained for the five participants are summarized in Table 5.4 and Table 5.5, for the arm and the lower leg respectively. Note that the impedance parameters $Z_{in}$ and $Z_{12}$ include three different

angles (0º, -10º, +10º). As the needle electrodes were inserted manually, a misalignment of ±10º between both electrodes could be obtained.

TABLE 5.4.
Arm impedance parameters at 6.78 MHz.

| Impedances | | P1 | P2 | P3 | P4 | P5 |
|---|---|---|---|---|---|---|
| $Z_{ex}$ (Ω) | | 94-29i | 95-28i | 104-32i | 59-15i | 56-19i |
| $Z_{im}$ (Ω) | 0º | 423-63i | 460-69i | 432-65i | 450-62i | 416-63i |
| | -10º | 418-62i | 454-68i | 424-63i | 411-61i | 411-62i |
| | +10º | 430-64i | 484-73i | 444-67i | 431-64i | 420-64i |
| $Z_{12}$ (Ω) | 0º | 19-4i | 20-4i | 19-4i | 13-2.3i | 13-3.2i |
| | -10º | 15-3.1i | 17-3.4i | 14.7-3i | 8.1-1.5i | 10.6-2.5i |
| | +10º | 22-4.6i | 23.4-4.7i | 23-4.9i | 17.8-3.2i | 15.8-3.8i |

TABLE 5.5.
Lower leg impedance parameters at 6.78 MHz.

| Impedances | | P1 | P2 | P3 | P4 | P5 |
|---|---|---|---|---|---|---|
| $Z_{ex}$ (Ω) | | 79-19i | 72-20.1i | 87-24i | 60-15.1i | 61-15.5i |
| $Z_{im}$ (Ω) | 0º | 429-63i | 423-63i | 491-73i | 418-62i | 419-62i |
| | -10º | 425-63i | 420-62i | 484-72i | 419-62i | 415-61i |
| | +10º | 438-65i | 428-63i | 547-83i | 410-60i | 424-63i |
| $Z_{12}$ (Ω) | 0º | 7.6-1.3i | 7.7-1.3i | 6.7-1.2i | 7.6-1.3i | 7.5-1.3i |
| | -10º | 6.4-1.1i | 6.3-1.1i | 5.5-1i | 6-1i | 6.1-1.1i |
| | +10º | 8.9-1.5i | 9.1-1.6i | 8-1.4i | 9.3-1.6i | 8.9-1.6i |

An alignment of 0º corresponds to a parallel alignment between both cylindrical electrodes, -10º corresponds to the case when the distance between both tip electrodes was minimum and +10º corresponds to the case when the separation distance on the tips was maximum.

Modelling the z-parameters as a T-circuit, the power delivered to the load (PDL) can be expressed as

$$P_{\text{load}} = |I_{\text{load}}|^2 \Re(Z_{\text{load}}), \tag{5.2}$$

where $P_{\text{load}}$ is the power dissipated at the load, and $I_{\text{load}}$ is the current flowing through the load. $I_{\text{load}}$ can be calculated as

$$I_{\text{load}} = I_{\text{ex}} \frac{Z_{12}}{Z_{\text{in}} + Z_{\text{load}}}. \tag{5.3}$$

The power transmission efficiency (PTE) of the system is calculated as

$$PTE = \frac{P_{\text{load}}}{P_{\text{total}}} 100, \tag{5.4}$$

where $P_{\text{total}}$ is the total power delivered through the external electrodes. In addition, the 3D computational model was also used to calculate the electric potential and the electric field magnitude distributions inside the tissues. For that, a sinusoidal voltage (frequency = 6.78 MHz) was applied to the external electrodes, being its RMS value equal to the RMS value of the experimental applied waveform. The transformation from amplitude values into RMS values was done by applying the mentioned scaling factor $k\sqrt{FB}$, with $k = \sqrt{11/32}$. The projected local SAR was calculated from the electric field magnitude according to the safety standard, with equation (2.7). The SAR was space-averaged over any cubical 10-g of tissue following the guidelines of the standard [131],[52].

## 5.3 Results

### 5.3.1 *Maximum transferred power*

Fig. 5.6a shows an MRI image corresponding to the arm of participant P3. The markers of the external electrodes can be observed in this image. After building a 3D computational model from the MRI images, the electric field, the electric potential and the projected SAR (see definition in subsection 5.2.8) distributions were numerically calculated. It can be observed that, within the region encompassed by the two external electrodes, a few millimeters away from them, the electric field is coarsely uniform where the section of the limb smoothly changes (arm of the participant P3: Fig. 5.6b, rest of limbs: Fig. 5.7). Consequently, the electric potential coarsely drops

linearly between those electrodes (arm of the participant P3: Fig. 5.6c, rest of limbs: Fig. 5.8). Regarding the projected SAR distribution, it can be noted that maxima are generally located near the external electrodes. However, it is also worth noting that the values of these SAR maxima do not differ substantially from the SAR values where the needle electrodes were placed (arm of the participant P3: Fig. 5.6d, rest of limbs: Fig. 5.9). Thus, the fact of having the SAR maxima close to the external electrodes does not significantly limit the maximum power transferred to the implants.

The average optimal load (i.e., the resistance that experimentally maximized the received ac power) was (244 ± 9) Ω (mean ± standard error of the mean, SEM) for the arms and (258 ± 6) Ω (mean ± SEM) for the lower legs (see Table 5.6). The received ac powers (for the optimal load) for both limbs of all the participants are reported in Fig. 5.10a.

This time-averaged power was obtained in the load with it connected to the pair of intramuscular electrodes when sinusoidal voltage bursts (carrier frequency = 6.78 MHz, $B$ = 100 μs and $F$ = 1 kHz) were applied across the external electrodes. It can be observed that the received ac power shows a quadratic dependency on the externally applied voltage amplitude. Powers up to a projected maximum SAR of 20 W/kg, which is the limit imposed by the IEEE safety standard [131] for limbs in controlled settings, are reported for arms of P2 and P5. In the remaining cases, the maximum reported power corresponds to a lower projected SAR due to technical limitations (i.e., maximum output amplitude of the generator) during the experimentation. For the arms, the maximum received power ranges from 7.7 mW (A4) to 13.7 mW (A2), with an average value of (10 ± 2) mW (mean ± SEM). For the lower legs, these values are noticeably lower. They range from 3.1 mW (LL1) to 6.1 mW (LL5), with an average value of (4.3 ± 0.6) mW (mean ± SEM). These results indicate that powers in the order of milliwatts can be transferred while complying with the safety standard. For a projected maximum SAR of 10 W/kg, the received powers in the arms range from 4.0 mW (A5) to 7.3 mW (A3), with an average value of

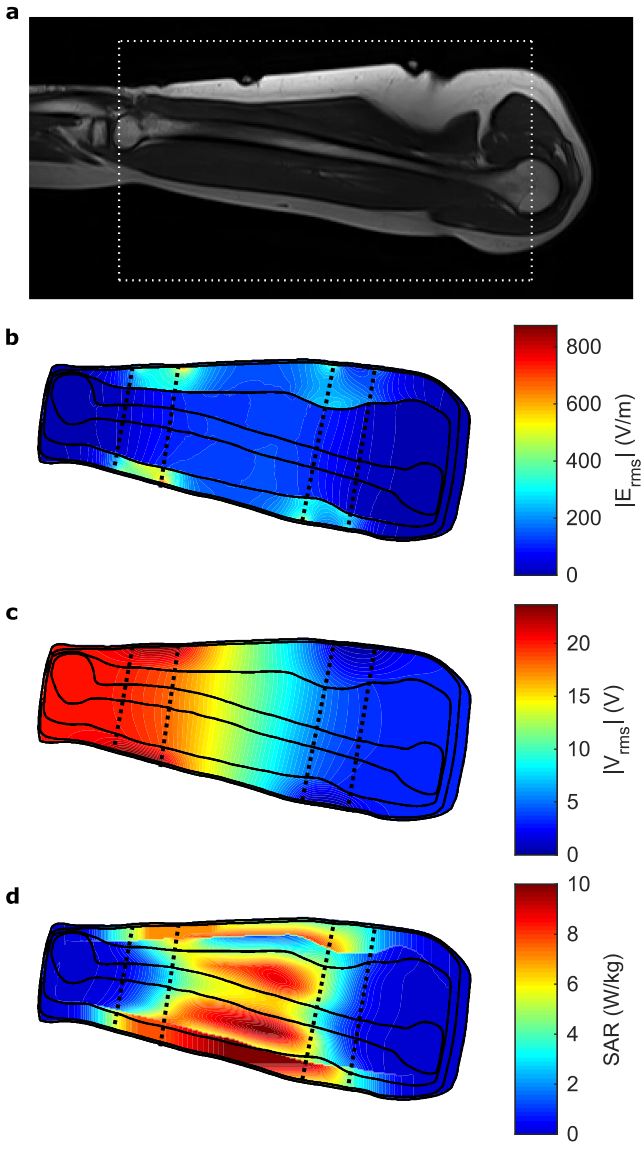


**Fig. 5.6.** Examples of MRI computed electric field, electric potential and projected SAR distributions, and power transfer experimental results. (a) MRI image of the arm of participant P3 (i.e., A3). (b) Computed electric field distribution inside A3. (c) Computed electric potential distribution inside A3. (d) Computed projected SAR distribution inside A3.

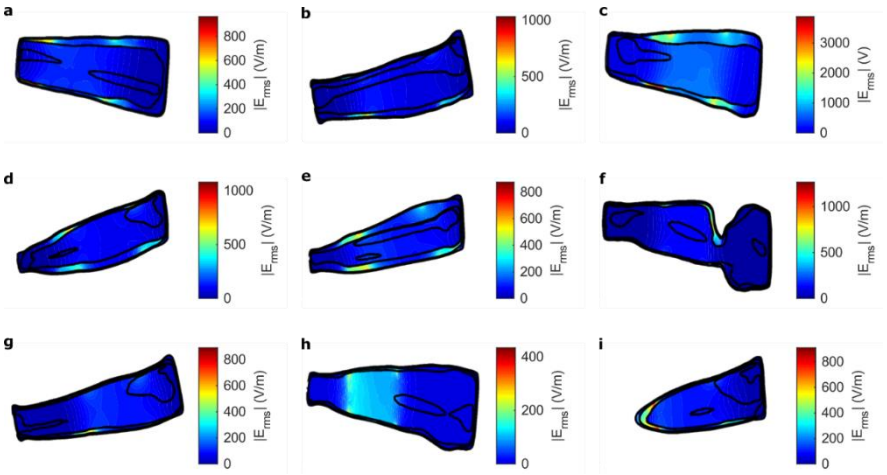


**Fig. 5.7.** Computed electric field distribution for each case. a, Arm of P1 (A1). b, Lower leg of P1 (LL1). c, Arm of P2 (A2). d, Lower leg of P2 (LL2). e, Lower leg of P3 (LL3). f, Arm of P4 (A4). g, Lower leg of P4 (LL4). h, Arm of P5 (A5). i, Lower leg of P5 (LL5). The electric field distribution for the arm of P3 (A3) is reported in Fig. 5.6b.

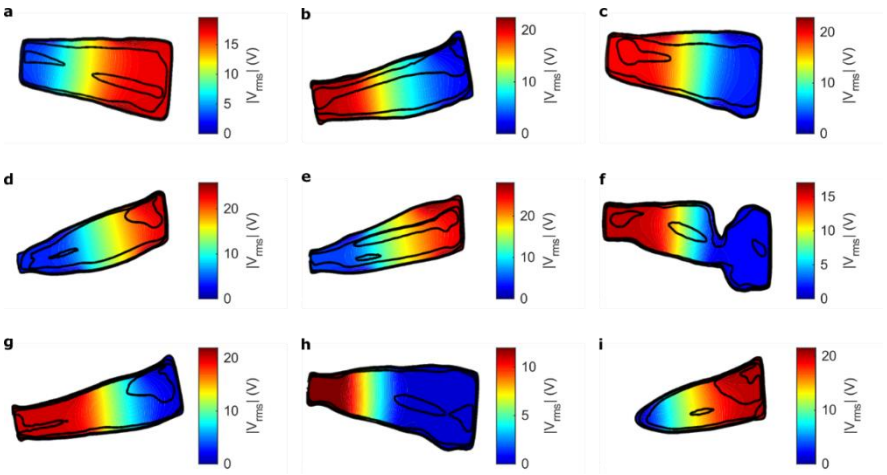


**Fig. 5.8.** Computed voltage distribution for each case. a, Arm of P1 (A1). b, Lower leg of P1 (LL1). c, Arm of P2 (A2). d, Lower leg of P2 (LL2). e, Lower leg of P3 (LL3). f, Arm of P4 (A4). g, Lower leg of P4 (LL4). h, Arm of P5 (A5). i, Lower leg of P5 (LL5). The voltage distribution for the arm of P3 (A3) is reported in Fig. 5.6c.

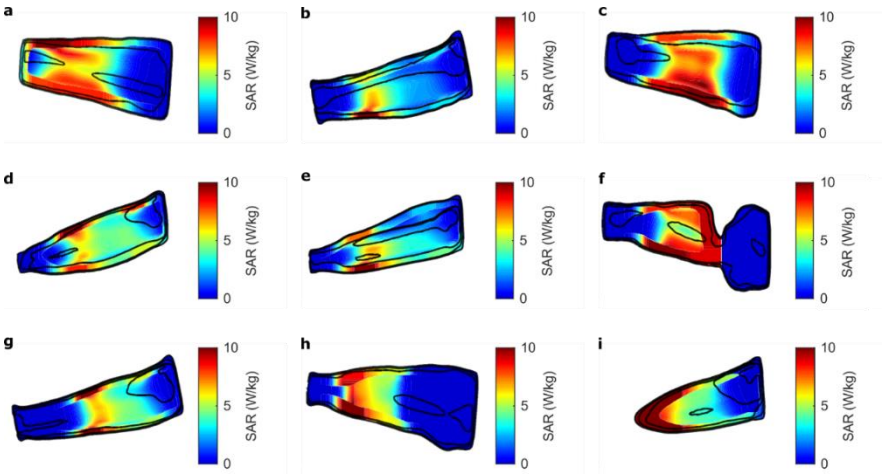


**Fig. 5.9.** Computed projected SAR distribution for each case. a, Arm of P1 (A1). b, Lower leg of P1 (LL1). c, Arm of P2 (A2). d, Lower leg of P2 (LL2). e, Lower leg P3 (LL3). f, Arm of P4 (A4). g, Lower leg of P4 (LL4). h, Arm of P5 (A5). i, Lower leg of P5 (LL5). The projected SAR distribution for the arm of P3 (A3) is reported in Fig. 5.6d.

(5.9 ± 0.7) mW (mean ± SEM), and in the lower legs they range from 2.0 mW (LL1) to 3.3 mW (LL5), with an average value of (2.4 ± 0.3) mW (mean ± SEM) (see Fig. 5.10b).

TABLE 5.6.
Optimal $Z_{load}$ for each participant and limb.

| $Z_{load}$ (Ω) | P1 | P2 | P3 | P4 | P5 |
|---|---|---|---|---|---|
| Arm | 210 | 250 | 260 | 250 | 250 |
| Lower leg | 260 | 250 | 280 | 250 | 250 |

The channel efficiency for every single case is reported in Fig. 5.10c. For the arms, it ranges from 0.15% (A4) to 0.27% (A2), with an average value of (0.19 ± 0.03)% (mean ± SEM). For the lower legs, it ranges from 0.029% (LL3) to 0.047% (LL5), with an average value of (0.035 ± 0.003)% (mean ± SEM). The difference between arms and lower legs is mainly due to the anatomical characteristics of both limbs (e.g., volume, section, length, fat thickness, etc.) [131]. These power transfer efficiencies in the order of 0.1% are much lower than

those typically reported, in the order of 1% or even in the order of 10%, for WPT systems based on inductive coupling or ultrasonic acoustic coupling [26], [52].

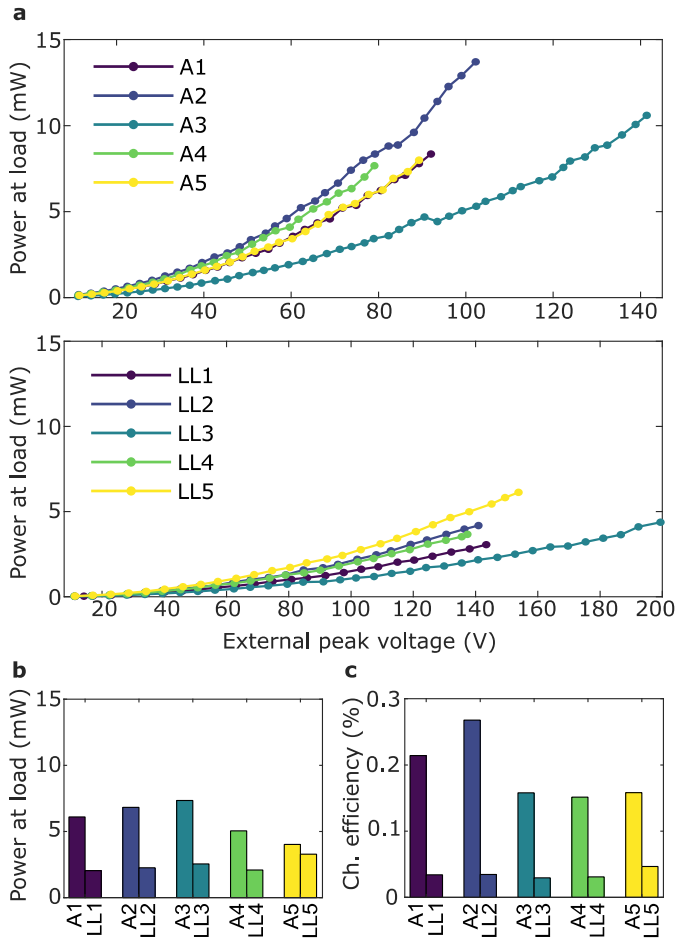


**Fig. 5.10.** (a) Maximum transferred power to the optimal load connected across the pair of intramuscular needle electrodes when sinusoidal voltage bursts (carrier frequency = 6.78 MHz, burst duration = 100 µs and repetition frequency = 1 kHz) were applied across the pair of external electrodes: in the arms (i.e., A1 to A5) on top and in the lower legs (i.e., LL1 to LL5) on the bottom. Dots indicate experimental measurements. (b) Maximum transferred power to the optimal load with a projected maximum SAR of 10 W/kg. (c) Channel efficiency.

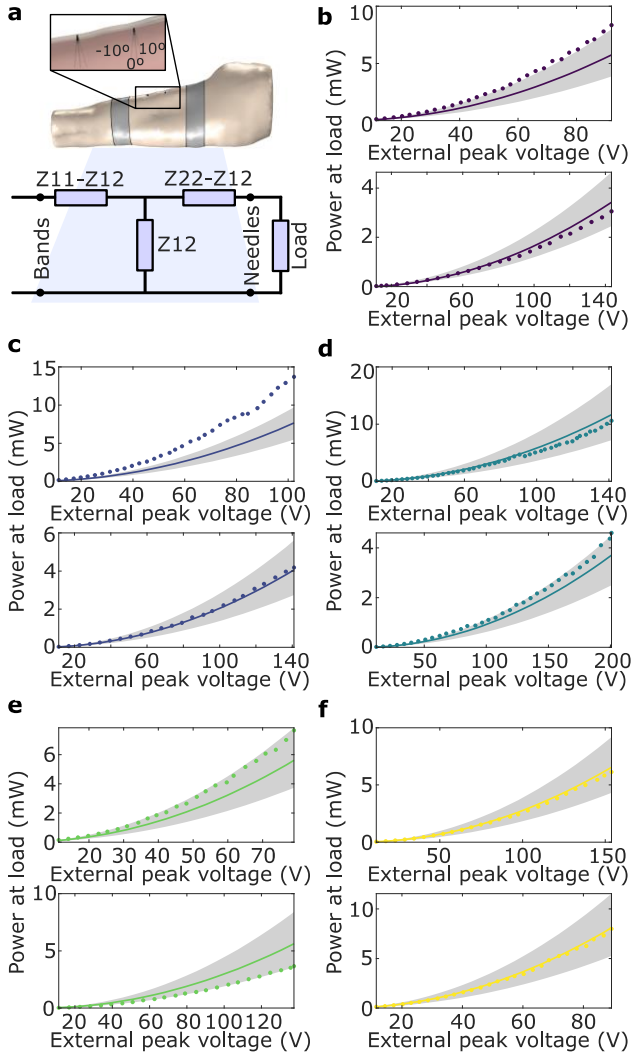


**Fig. 5.11.** Computational modeling results. (a) The transmission channel (i.e., limb tissues, band electrodes and needle electrodes) was modeled as a two-port network. The inlet shows the considered insertion angle error of the needle electrodes. (b) Comparison of experimental maximum transferred power and simulated transferred power using the optimal experimental load in the arm (top) and in the lower leg (bottom) of P1. Dots indicate experimental measures. Solid line indicates simulated results under the assumption that that both needle electrodes are perfectly aligned (i.e., 0º). Upper shadow edge indicates simulated results under the assumption that both needle electrodes have an inclination of -10º (i.e., 10º towards the center). Lower shadow edge indicates simulated results under the assumption that both needle electrodes have an inclination of +10º (i.e., 10º towards the band electrodes). (c) Same as Fig. 5.11b for P2. (d) Same as Fig. 5.11b for P3. (e) Same as Fig. 5.11b for P4. (f) Same as Fig. 5.11b for P5.

### 5.3.2 *Computational model validation*

The transmission channel formed by the band electrodes, the tissues and the needle electrodes was modeled as a two-port impedance network (Fig. 5.11a) [48]. The impedance (Z) parameters of the network were numerically computed using the 3D computational model of the limb obtained after segmenting the MRI images. The obtained two-port impedance networks allow simulating power transfer with reasonable accuracy. As an example, when applying a peak voltage of 79 V across the external electrodes, the average relative error between the experimentally received power and the simulated one is 4%, with a standard deviation of 26% (see Fig. 5.11b-f).

### 5.3.3 *Powering electronic devices*

Fig. 5.12a shows a picture of an electronic device connected to the needle electrodes of the arm of P1, being safely powered according to the IEEE standard through volume conduction of HF current bursts (carrier frequency = 6.78 MHz, $B$ = 100 µs, and $F$ = 1 kHz). The electronic device connected to the needle electrodes does not contain any power source and it is composed by: 1) a circuit consisting of a bridge rectifier with dc blocking capacitors, a voltage regulator and a microcontroller and 2) an LCD screen (see inlet in Fig. 5.12a).

This device is similar to most implantable medical devices in terms of complexity and power consumption (approximately 1 mW). Fig. 5.12c reports the projected maximum SAR that appears in tissues when the amplitude of the external voltage is sufficient for powering the device in all participants and limbs. In all cases, the SAR is below 10 W/kg. It ranges from 2.3 W/kg (A3) to 4.0 W/kg (A5) for the arms, with an average value of (3.2 ± 0.4) W/kg (mean ± SEM). For the lower legs, it ranges from 6.2 W/kg (LL5) to 8.1 W/kg (LL1), with an average value of (7.0 ± 0.4) W/kg (mean ± SEM). Fig. 5.12b shows two electronic devices being powered by the same pair of external electrodes in the lower leg of P4.

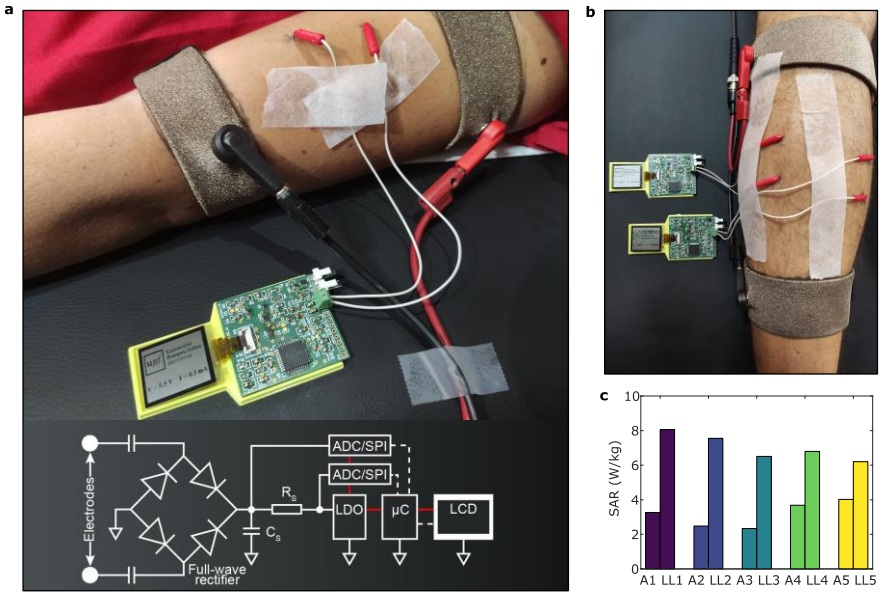


**Fig. 5.12.** Illustration of the capability of WPT based on volume conduction for safely powering electronic devices. (a) Picture of an electronic device, which is comparable to a medical implant in terms of circuit complexity and power consumption, being powered by volume conduction of high frequency current bursts (carrier frequency = 6.78 MHz, burst duration = 100 µs, and repetition frequency = 1 kHz). The insert shows the circuit diagram of the electronic device. This device connected to the needle electrodes does not contain any power source and it is composed by: a circuit consisting of a bridge rectifier with dc blocking capacitors, a voltage regulator and a microcontroller and 2) an LCD screen (b) Two devices being simultaneously powered by the same current bursts. (c) Projected maximum SAR in tissues when the amplitude of the external voltage is sufficient for powering the electronic devices of this setup.

## 5.4 Discussion

The obtained results highlighted that the electric potential within the tissues located between the external electrodes coarsely drops linearly (Fig. 5.6b-c). This is noteworthy for two reasons: 1) the electric field at the location of an implant (and hence the power obtained by the implant [136]) would not depend on the implantation

depth, and 2) WPT based on volume conduction can be considered to be a non-focused WPT method since the applied electric field is present in the whole inter-electrode region. Non-focality implies that WPT based on volume conduction can be used for powering multiple implants with the same external energy source (this fact is illustrated in subsection 5.3.3). Examples of non-focused methods are those based on Helmholtz-like coil configurations [19]. Moreover, each device only draws a small portion of the total external energy without significantly distorting the electric field at the location of the other implant, thus enabling the possibility of increasing the total efficiency of the method by increasing the number of devices in the same powered area.

Comparison in terms of efficiency with published WPT systems is not straightforward as efficiency depends on multiple factors such as the geometry of the elements (e.g., the dimensions of the external applicator and of the receiver) and the relative conformation of the elements of the system (e.g., whether the receivers are within a region encompassed by the applicator of the transmitter). In fact, for some conformations, volume conduction is advocated by some researchers because of its superior efficiency [26]. Comparison of the results reported here for the arm (efficiency around 0.2%) with those reported for a similar scenario in which inductive coupling was assayed *ex vivo* with an efficiency of around 2% [19] suggests that volume conduction is ten times less efficient than inductive coupling. Nevertheless, this comparison must be considered as inconclusive because the receiver inductor of that study had a diameter of 4 mm and inductive coupling efficiency strongly depends on such diameter [53]. Further research is required regarding this aspect. In any case, the efficiency of volume conduction does not jeopardize the feasibility of using a wearable external system (such as the one showed in the envisioned scenario in Fig. 5.1). Taking into account the mean of the channel efficiency (i.e., 0.19% and 0.035% for arms and lower legs, respectively) and the power consumption of electronic medical implants (typically 1 mW or less), the externally applied power should be in the order of 0.5 and 3 W for the arms and lower legs, respectively. In the market, there are several wearable rechargeable batteries (e.g., 100 $cm^3$ or less) that provide more than

30 W for one hour (e.g., 2447-3034-20-520 from Ansmann AG, Assamstadt, Germany).

Regarding the two-port model, after analyzing the impact of different possible sources of error in the experimental procedures and in the simulations, it was determined that the variability in the insertion angle of the needle electrodes was the most likely cause of the discrepancies observed between the simulated and the experimental results. This variability causes significant random errors in the separation distance between the conductive tips of the electrodes. Even though the location of the insertion point of the needles was carefully ensured by using markers, the insertion was performed manually orthogonally to the skin without any provision to ensure the penetration angle. Simulations were performed assuming ±10° errors in the penetration angle. Considering this penetration angle error margin, the simulations fit the experimental results in all cases except for the arm of P2. This inconsistency may be caused by the fact that, in this case, the insertion marks of the needle electrodes had to be displaced 5 mm from the original position to avoid a blood vessel that was detected in the MRI images during the experimentation. Although the position of the needles was accordingly modified on the numerical model, this adjustment may explain the inconsistency.

None of the participants reported any sensation related to heat or electrostimulation during the experimentation in both limbs. They barely reported uncomfortable sensations related to the fact of having the needles inserted. Therefore, the applied HF current bursts are not only innocuous, as guaranteed by adherence to the IEEE standard, but also imperceptible. No skin alterations were observable. This study focuses on the safety of the method by following the IEEE standard on safety levels with respect to human exposure to electromagnetic fields. These aspects can be extrapolated to chronic implants but, for the final application (chronic use with implantable devices), there are other safety aspects (e.g., long-term electrode changes, mechanical stability, etc.) that should be analyzed in chronic animal studies.

## 5.5 Conclusions

This study in healthy participants demonstrates that, albeit with poor efficiency, ac and dc electric powers in the order of milliwatts can be obtained from pairs of thin electrodes within limb muscles when HF sinusoidal current bursts are safely delivered through two textile electrodes shaped as bands strapped around the limb and encompassing the region where the pair of thin electrodes is located. In addition, it is demonstrated that these currents are imperceptible and that the obtained power from the pair of thin electrodes can be used to power complex electronic circuits with digital and analog functionalities. To the best of our knowledge, this is the first time that the use of WPT based on HF volume conduction has been validated in humans. Since none of the observations and principles preclude the use of this approach in other comparable conditions (e.g., different waveforms, tissues, anatomical locations or geometries for the systems), the results of this study pave the road for the development of diagnostic and therapeutic systems using threadlike electronic implants powered by WPT based on HF volume conduction in limbs.

In addition to unprecedented minimal invasiveness, other remarkable advantages of the presented approach over other WPT methods are the capabilities to: 1) power deep implants, 2) simultaneously power multiple implants with the same external applicator, 3) deliver high peak powers and 4) avoid inconvenient external applicators and elements such as rigid bulky coils for inductive coupling or gels for ultrasonic acoustic coupling.

Furthermore, this study proposes and demonstrates a procedure to accurately model WPT based on volume conduction that characterizes the coupling between the transmitters and the receivers by means of two-port impedance models generated from medical imaging data. This procedure is not only relevant for the design of systems using WPT based on volume conduction, but it could also be applied for modeling transmission channels in intrabody communications based on volume conduction.

## 5.6 Appendix

In terms of the electrostimulation effects, the IEEE safety standard [131] defines the dosimetric reference level (DRL) as the in situ electric field, and it is determined for frequencies between 0 Hz and 5 MHz. Accordingly, for continuous 6.78 MHz sinusoidal waveform, which is the carrier frequency of the sinusoidal voltage bursts used in this study, the DRL for electrostimulation mechanisms does not apply. However, the standard also provides limits for non-sinusoidal fields, as it is the case here. The standard indicates that the exposure waveform consisting of multiple frequencies must satisfy that

$$\sum_{0\ \mathrm{MHz}}^{5\ \mathrm{MHz}} \frac{A_i}{RL_i} \leq 1, \tag{5.5}$$

where $A_i$ is the magnitude of the *ith* Fourier component of the sinusoidal voltage bursts, and $RL_i$ represents the in situ electric field restriction defined by the maximum allowed in situ electric field $E_i$ for the *ith* Fourier component

$$E_i = \begin{cases} E_0, & f < f_\mathrm{e} \\ E_0 \dfrac{f}{f_e}, & f \geq f_\mathrm{e} \end{cases} \tag{5.6}$$

where $E_0$ is the rheobase in situ field, $f_\mathrm{e}$ is the transition frequency, and $f$ is the frequency of the *ith* Fourier component. For the scenario considered in this study, in which the sinusoidal voltage bursts are applied to the limbs, $E_0$ is defined as 2.10 $V_{rms}$/m, and $f_\mathrm{e}$ is defined as 3350 Hz.

To avoid electrostimulation there are two ranges: a lower bound ($f \leq 3350$ Hz) and an upper bound (5 MHz $\geq f >$ 3350 Hz). Therefore,

$$\sum_{0}^{3350\ \mathrm{Hz}} \frac{A_i}{E_0} + \sum_{3350\ \mathrm{MHz}}^{5\ \mathrm{MHz}} \frac{A_i}{E_0 \dfrac{f_i}{f_e}} \leq 1. \tag{5.7}$$

The maximum peak electric field that could be applied by the voltage generator was calculated according to equation (5.7) using MATLAB R2019a. The sinusoidal voltage burst waveform (carrier frequency = 6.78 MHz, $B$ = 100 µs and $F$ = 1 kHz) was smoothed with a tapered cosine window created using the tukeywin function

from MATLAB (5.8), with $r = 0.5$. A 0.1 s duration waveform was then generated using a sampling frequency of 100 Msps, and its discrete Fourier transform was calculated. After identifying the two ranges defined by equation (5.7), their summation was computed having in mind the magnitude of the $ith$ Fourier component, the rheobase in situ field, and the transition frequency. The resulting maximum peak electric field (i.e., the maximum in situ electric field to avoid electrostimulation) was approximately 227 MV/m.

To minimize the contribution of the harmonics generated by windowing the sinusoidal waveform, the applied bursts were smoothed with a tapered cosine window. This window is defined as

$$w(t) = \begin{cases} \frac{1}{2}\left[1 - \cos\left(\frac{2\pi t}{rB}\right)\right], & 0 \le t \le \frac{r}{2}B \\ 1, & \frac{r}{2}B \le t \le B - \frac{r}{2}B \\ \frac{1}{2}\left[1 - \cos\left(\frac{2\pi t}{rB} - \frac{2\pi}{r}\right)\right], & B - \frac{r}{2}B \le t \le B \end{cases} \tag{5.8}$$

where $r$ is the cosine fraction and $B$ is the burst duration (i.e., window duration). This window is a rectangular window with the first and last $r/2$ percent of the time equal to parts of a cosine. The expression for a single smoothed burst with a sinusoid as the modulated waveform is

$$\begin{aligned} b(t) &= v(t)w(t) \\ &= V_{\text{peak}} \sin(2\pi f t + \varphi)w(t), \end{aligned} \tag{5.9}$$

where $V_{\text{peak}}$, $f$ and $\varphi$ are the amplitude, frequency and initial phase of the sinusoidal modulated waveform respectively. Therefore, the RMS voltage of the waveform during the burst ($V_{\text{rms in burst}}$) is

$$V_{\text{rms in burst}} = \sqrt{\frac{1}{B}\int_0^B [v(t)w(t)]^2 dt}. \tag{5.10}$$

If we assume $\varphi = 0$ and $rBf/2$ is an integer number higher than zero (which corresponds to our case), then

$$V_{\text{rms in burst}} = \frac{V_{\text{peak}}}{\sqrt{2}}\sqrt{1-\frac{5}{8}r} = V_{\text{peak}}k, \tag{5.11}$$

where $k$ is a constant that depends on the cosine fraction $r$. The RMS voltage of the waveform ($V_{\text{rms}}$) is

$$V_{\text{rms}} = V_{\text{peak}}k\sqrt{FB}, \tag{5.12}$$

where $FB$ is the duty cycle, being $F$ and $B$ the repetition frequency and the duration of the bursts, respectively. Therefore, for power calculation, a scaling factor $k\sqrt{FB}$ has to be applied to transform amplitude values into RMS values for the applied waveform. A cosine fraction $r$ = 0.5 was used, thus $k = \sqrt{11/32}$ . A smoothed burst ($V_{\text{peak}}$ = 1 V, $f$ = 6.78 MHz, $B$ = 100 µs) is shown in Fig. 5.13.

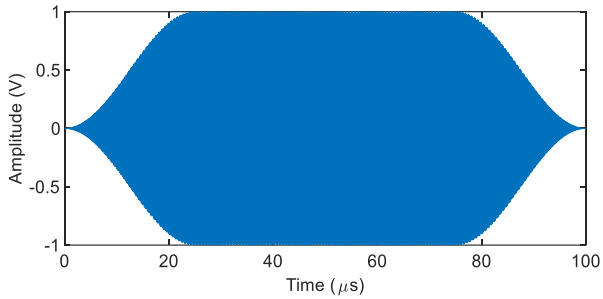


**Fig. 5.13.** Smoothed burst ($V_{\text{peak}}$ = 1 V, $f$ = 6.78 MHz, $B$ = 100 µs) with tapered cosine window ($r$ = 0.5).

# Chapter 6

## NUMERICAL ANALYSIS OF COMMUNICATIONS BY VOLUME CONDUCTION BASED ON LOAD MODULATION

**Abstract —** To develop minimally invasive electronic implants, it is essential to minimize their power consumption. A substantial part of the power consumption of most biomedical implants is associated with communications and, in particular, with the channel from the implant to the external system. Thus, for communications, rather than relying in active injection of energy into the medium, the current trend is to develop implants with passive communication methods. In these methods, the energy for communications is provided by the external system and the implant performs communications by passively interacting with such energy. One of the most common passive communications methods is load modulation. Although this method has been broadly used in inductive coupling, it has barely been used until recently in coupling by volume conduction. This chapter presents a simple modulation circuit and its analytical model that allows determining the variation in externally applied current as a function of the modulation of the implant. The analytical expression is obtained by modeling the transmission link as a two-port network and considering a communication circuit that consists of a diode bridge with a variable resistance in series with a MOSFET at its output. This circuit has been demonstrated *in vitro* using a saline solution as a transmission medium. On the one hand, the results highlighted that thin (< 1 mm) and elongated implants (> 2 cm) could transmit digital information with a low bit-error rate (BER) (< 0.01), even when separated by several centimeters from the external electrodes. On the other hand, the results showed that the circuit model can determine the variation of the external impedance as a function of the modulation performed by the implant. Hence, the proposed analytical model here can be especially handy for sizing future implant designs.

## 6.1 Introduction

The deployment of networks of minimally invasive implants that allow the interaction and monitoring of physiological functions would revolutionize how we treat several current pathologies [141]. As it has been stated in Chapter 1.1, the bottleneck that is hampering the development of these networks is the difficulty of powering and communicating with millimeter or submillimeter implants, especially when these implants have to be deployed several centimeters inside the tissues [142].

The most widely used method of communicating and powering biomedical implants is inductive coupling [143]–[145]. Although this WPT method is energy efficient and well established for short-range applications and centimeter-sized devices (e.g., cochlear implants [146]), typically, these systems work at relatively low frequencies (< 10 MHz) in resonance to maximize power transmission efficiency and this limits their bandwidth for communications [142]. To overcome this limitation, several authors have proposed using separated coils (or antennas) for power and for communication [147], [148]. However, using extra coils (or antennas) increases the implants' complexity and bulkiness, furthering the challenge of developing minimally invasive implants. Furthermore, due to the lossy nature of the biological tissues, it is challenging to design communication links based on RF propagation when millimetric or sub-millimetric biomedical implants are placed deep inside the tissues [149].

The use of coupling by volume conduction, typically less accurately referred to as galvanic coupling has gained increasing interest as an intrabody communication (IBC) method [150]–[152]. This method uses the biological tissues in the human body as a transmission channel. For communication, in most cases, the transmitter (either the external system or the implant) injects an innocuous high-frequency current to the tissues, and the receiver gets the information by sensing the voltage gradient such current produces. This method has been studied mainly for superficial battery-powered

medical devices [84], [86], [153]. In addition to simplicity this method offers security. Since the biological tissues are more conductive than the air, the communication signals are mostly confined inside the body. As a consequence, this method is inherently more secure than radiated methods [58].

Current injection by the external system for performing (downlink) communications is generally not an issue because energy is readily available. However, it is an issue for the design of the implant because, as said, the energy source or its reservoir have a very important impact on the size of the implant. Because of that, it has been proposed to develop implants that perform (uplink) communications by passively interacting with current applied externally. In particular, it has been proposed to perform load modulation [154]. In [155], we proposed a battery-free communication scheme in which the implant modulates its load to communicate with the external system.

Although coupling by volume conduction and, in particular, communications by volume conduction based on load modulation, are relatively new and unexplored, the use of load modulation also referred to as impedance modulation, for passive communications is well known in the field of inductive coupling and in the field of RF communications, where it is also referred to as backscattering. In backscattering the reflection of the applied incident waves changes, so the receiver can sense these load changes [156]. Most current backscattering biomedical studies are based on inductive coupling or RF radiation, where the resonance of the link is exploited to optimize the load modulation communication [144], [157]–[159].

In [70], load modulation was performed using the same circuits used to do neuromuscular stimulation. This chapter introduces, models, and *in vitro* validates a more generic load modulation circuit that does not require current stimulators. Briefly, the load modulation circuit emulates an ac switch using a diode bridge with a MOSFET that allows the bridge output to be shorted or in an open circuit.

Fig. 6.1 shows an envisioned scenario where an implant communicates with an external system using load modulation based

on volume conduction. The implant can modulate its load, so the external current is slightly modified by this modulation.

The following sections of this chapter describe the proposed modulation circuit. Then, the two-port model introduced in Chapter 4 is adjusted to model the envisioned scenario (Fig. 6.1). The analytical model obtained is then demonstrated *in vitro* using a homogeneous saline solution as a transmission medium. Finally, the influence on communications of the main parameters of the system is studied.

## 6.2 Methods

### 6.2.1 *Load modulation*

The operation principle of load modulation based on volume conduction is that the external current can be slightly modified by modulating the amplitude of the current flowing through the implant.

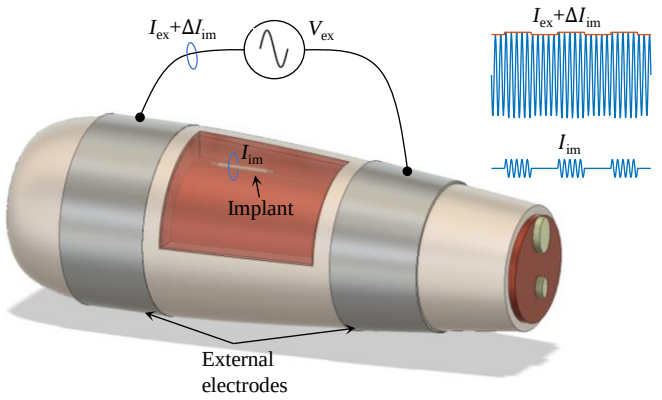


**Fig. 6.1.** An envisioned scenario where a flexible and thin implant communicates with an external system by modulating its load. The current flowing through the implant ($I_{im}$) influences the external flowing current ($I_{ex}$).

Here, we propose to use the external HF current as a carrier signal while the digital data is modulated using amplitude-shift keying (ASK) modulation. The simplest case of load modulation is when the implant alternates between shorting its electrodes and leaving its load at high impedance. In this way, keeping the amplitude of $V_{\mathrm{ex}}$ constant,

the value of $I_{ex}$ will increase if the implant short-circuits its load, compared to the case in which the load is left at high impedance.

### 6.2.2 *Analytical model and modulation circuit*

The communication system envisioned in Fig. 6.1 can be split into three main blocks: the external system, the transmission channel, and the implant communication circuit (Fig. 6.2). The external system consists of a high-frequency voltage generator that can also sense its current. The transmission channel entails the interface between the external electrodes, the tissues, and the interface of the implant electrodes. Due to the complexity of obtaining a closed-analytical model considering the interface between several tissues in a finite medium, the channel has been modeled as a two-port system, as explained in depth in Chapter 4.

The two-port model expressed using the *Z*-parameter matrix approach is defined as in (4.1). Since for frequencies above 10 kHz (i.e., beyond the bandwidth of the bioelectric signals), the transmission channel can be considered passive and the two-port model is reciprocal. Therefore, $Z_{exim}$ and $Z_{imex}$ are equivalent.

The communication circuit used in this study is shown in Fig. 6.2. The output of a diode bridge is connected to a variable resistor in series with a MOSFET. Two blocking capacitors are connected in series between the electrodes and the bridge to avoid potentially dangerous low-frequency currents that can affect both the electrodes and the tissues. If $R_M$ is zero, assuming ideal semiconductors and a frequency that allows the neglection of the dc-blocking capacitors, the circuit emulates an ac-switch. By controlling the gate voltage of the MOSFET, the communication circuit can short-circuit the implant electrodes or leave the circuit in high-impedance mode. The implemented ac switch minimizes the use of extra components in the implant (since most of the current implant already have a rectifier). Furthermore, as the circuit has few and simple electronic components, its voltage and current can be analytically determined.

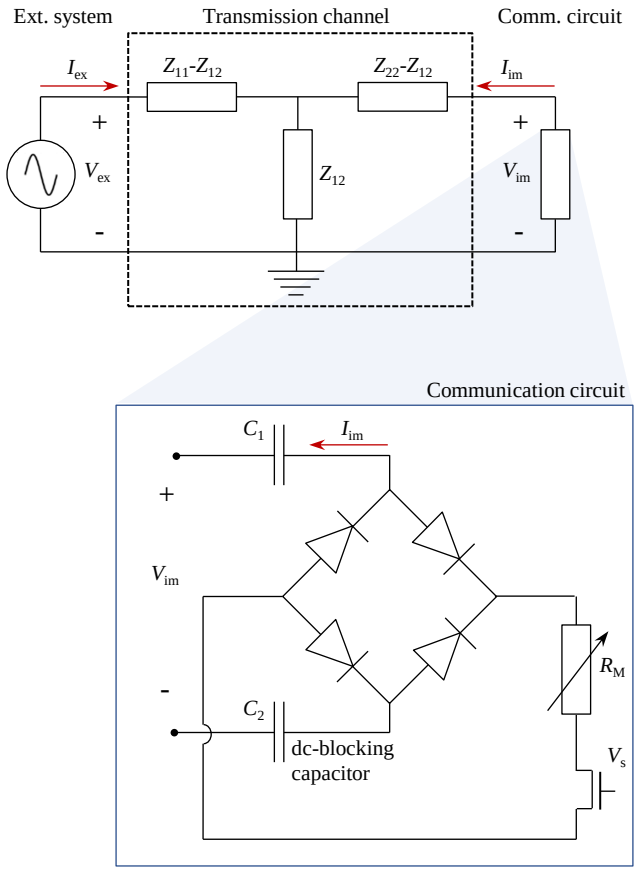


**Fig. 6.2.** Schematic model of the proposed system. The communication system is split into three blocks: the external system, the transmission channel, and the communication circuit.

To obtain an analytical solution, we have determined the current flowing through the implant as a function of the MOSFET's region of operation (cutoff or linear). Furthermore, the diodes are simplified to obtain a closed analytical expression as a combination of an ideal diode and a series voltage source ($v_{\mathrm{D}}$). The MOSFET is modeled as a resistor ($R_{\mathrm{sw}}$) when it operates in the linear region and as an open circuit in the cutoff region.

The implant's current ($I_{\mathrm{im}}$) when the MOSFET operates in the cutoff region is zero. To calculate $I_{\mathrm{im}}$ when the MOSFET operates in its linear zone, it is necessary to determine, on the one hand, the

conduction duty cycle ($D$) (i.e., the conduction angle divided by the whole cycle angle), and on the other hand, the rms value of $I_{\mathrm{im}}$ when $|V_{\mathrm{im}}| > 2v_{\mathrm{D}}$.

To determine $D$, the conduction angle for a semi-cycle ($\theta_{\mathrm{sc}}$) is defined as

$$\begin{aligned}\theta_{\mathrm{sc}} &= \omega(t_{\mathrm{off}} - t_{\mathrm{on}}),\\ &= \pi - \sin^{-1}\left(\frac{2v_{\mathrm{D}}}{V_{\mathrm{im}}\sqrt{2}}\right) - \sin^{-1}\left(\frac{2v_{\mathrm{D}}}{V_{\mathrm{im}}\sqrt{2}}\right),\\ &= \pi - 2\sin^{-1}\left(\frac{2v_{\mathrm{D}}}{V_{\mathrm{im}}\sqrt{2}}\right),\end{aligned} \tag{6.1}$$

where $\omega$ is the angular frequency, $t_{\mathrm{off}}$ is the time when the conduction stops (i.e., $|v_{\mathrm{im}}(t)| < 2v_{\mathrm{D}}$), and $t_{\mathrm{on}}$ is the time when the diode starts conducting (i.e., $|v_{\mathrm{im}}(t)| > 2v_{\mathrm{D}}$).

If $V_{\mathrm{im}} \gg v_{\mathrm{D}}$, (6.1) can be simplified as

$$\theta_{\mathrm{sc}} \approx \pi - \frac{4v_{\mathrm{D}}}{V_{\mathrm{im}}}. \tag{6.2}$$

Since, here, we have a symmetrical full-wave rectifier, for a complete period the complete conduction angle ($\theta_{\mathrm{cc}}$) is determined as

$$\theta_{\mathrm{cc}} = 2\theta_{\mathrm{sc}}. \tag{6.3}$$

Finally, by definition $D$ is calculated as

$$D = \frac{\theta_{\mathrm{cc}}}{2\pi}. \tag{6.4}$$

To facilitate the calculation of $I_{\mathrm{im}}$ when $|v_{\mathrm{im}}(t)| > 2v_{\mathrm{D}}$, the two-port model circuit of Fig. 6.2 is simplified using its Thévenin equivalent model calculated on the $V_{\mathrm{im}}$ terminals (Fig. 6.3).

The Thevenin impedance ($Z_{\mathrm{Th}}$) for the Fig. 6.3 circuit is defined as

$$Z_{\mathrm{Th}} = \frac{(Z_{\mathrm{ex}} - Z_{\mathrm{exim}})Z_{\mathrm{exim}}}{Z_{\mathrm{ex}}} + Z_{\mathrm{im}} - Z_{\mathrm{exim}}. \tag{6.5}$$

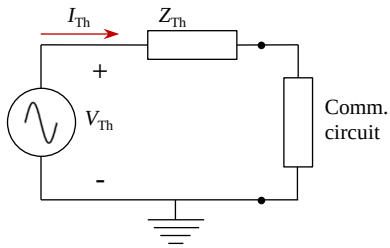


**Fig. 6.3.** Thévenin equivalent circuit of the two-port model calculated on the communication circuit terminals.

And its Thévenin voltage ($V_{\mathrm{Th}}$) as

$$V_{\mathrm{Th}} = V_{\mathrm{ex}} \frac{Z_{\mathrm{exim}}}{Z_{\mathrm{ex}}}. \tag{6.6}$$

Applying the Kirchhoff's second law in the Thévenin equivalent circuit (being the communication circuit the one introduced in Fig. 6.2), when the diodes conduce, $I_{\mathrm{Th}}$ is calculated as

$$\begin{aligned} I_{\mathrm{Th\,cc}} &= \frac{\frac{\sqrt{2}V_{\mathrm{Th}} - 2v_{\mathrm{D}}}{\sqrt{2}}}{Z_{\mathrm{Th}} + R_{\mathrm{M}} + R_{\mathrm{sw}} + 2Z_{\mathrm{C}}}, \\ &= \frac{V_{\mathrm{Th}} - \sqrt{2}v_{\mathrm{D}}}{Z_{\mathrm{Th}} + R_{\mathrm{M}} + R_{\mathrm{sw}} + 2Z_{\mathrm{C}}}. \end{aligned} \tag{6.7}$$

The rms value of $I_{\mathrm{Th}}$ (6.7) averaged over a complete carrier period ($T_{\mathrm{c}}$) is calculated as

$$\begin{aligned} I_{\mathrm{Th}} &= \frac{1}{T_{\mathrm{c}}} \int_0^{T_{\mathrm{c}}} |I_{\mathrm{Th}}(t)|^2 dt \\ &= I_{\mathrm{Th\,cc}} \sqrt{D}. \end{aligned} \tag{6.8}$$

Once the current flowing through the communications circuit has been determined, the Thévenin equivalent current can be related to the two-port model considering that

$$I_{\mathrm{im}} = -I_{\mathrm{Th}}. \tag{6.9}$$

Regarding $I_{\mathrm{ex}}$, isolating from (4.1), it is expressed as

$$I_{\mathrm{ex}} = \frac{V_{\mathrm{ex}} - Z_{12} I_{\mathrm{im}}}{Z_{11}}. \tag{6.10}$$

Therefore, when the MOSFET operates in its cutoff region, the current through the implant ($I_{\mathrm{im}}$) is zero, and so, the current through the external system ($I_{\mathrm{ex}}$) is $V_{\mathrm{ex}}$ divided by $Z_{11}$. When the MOSFET operates in its linear region, a current flows through the implant and $I_{\mathrm{ex}}$ is modified by $I_{\mathrm{im}}$, as (6.10) states.

### 6.2.3 *Noise and BER analysis*

The two main sources of noise for the described system are, on the one hand, the Johnson-Nyquist thermal noise and, on the other hand, the quantization noise. Both signals can be considered additive noises with an approximately flat power spectral density [160], [161]. The biological noise is mostly focused on the low-band frequencies, generally below 10 kHz [54]. Therefore, since the frequency band of digital communications will not coincide with the band of biological signals (> 10 kHz), the noise introduced by them can be filtered using a low-pass filter. The same stands for artifacts associated with body movements (< 10 Hz). For this reason, biological signals and movement artifacts were not considered the main noise sources.

The one-sided power spectral density Johnson-Nyquist noise ($N_{\mathrm{v-JN}}$) is calculated as

$$N_{\mathrm{v-JN}} = 4 k_{\mathrm{B}} T R, \tag{6.11}$$

where $k_{\mathrm{B}}$ $(J/K)$ is Boltzmann's constant, $T$ $(K)$ is the resistance temperature, and $R$ $(\Omega)$ is the resistance value. If the measured signal is current, (6.11) can be rearranged as

$$N_{\mathrm{i-JN}} = \frac{4 k_{\mathrm{B}} T}{R}. \tag{6.12}$$

Regarding the quantization noise, the one-sided quantization noise power ($N_{\mathrm{Q}}$) is calculated as

$$P_{\mathrm{Q}} = 2\frac{\Delta^2}{12}, \tag{6.13}$$

being Δ the step size of the converter

$$\Delta = \frac{FS}{2^n}, \tag{6.14}$$

$FS$ the full-scale range, and $n$ the number of bits. Assuming a uniform power spectral distribution, the power spectral density of (6.13) is calculated as

$$N_{\mathrm{Q}} = \frac{P_{\mathrm{Q}}}{N_{\mathrm{bin}}}, \tag{6.15}$$

where $N_{\mathrm{bin}}$ is the frequency bin width.

The power spectral density of the noise influences the bit-error rate (BER): the number of bit errors divided by the total number of transferred bits during a time interval. Assuming that the noise of the system is additive white Gaussian noise and the transmitted signal is modulated as ASK, the BER can be determined analytically as

$$BER = \frac{1}{2}\mathrm{erfc}\sqrt{\frac{E_{\mathrm{s}}}{2N_0}}, \tag{6.16}$$

where erfc is the Gauss error function and $E_{\mathrm{s}}$ is the energy of the symbol [162]. The symbol energy can be calculated as

$$E_{\mathrm{s}} = E_{\mathrm{b}} \log_2 M, \tag{6.17}$$

being $E_{\mathrm{b}}$ the bit energy and $M$ the total number of alternative modulation symbols. To analytically determine $E_{\mathrm{b}}$, first, the difference of (6.10) ($\Delta I_{\mathrm{ex}}$) is determined as a function of the state of the MOSFET. Then the bit energy is calculated as

$$E_{\mathrm{b}} = \frac{|\Delta I_{\mathrm{ex}}|^2}{f_{\mathrm{comm}}}, \tag{6.18}$$

where $f_{\mathrm{comm}}$ is the frequency of the digital communication.

### 6.2.4 *In vitro demonstration setup*

To demonstrate the proposed circuit (Fig. 6.2) and its analytical model (6.7)-(6.10), we used an *in vitro* setup based on a saline solution (Fig. 6.4). A container was filled with a homogeneous saline solution ($L$ = 146 mm, $W$ = 87 mm, and $D$ = 35 mm). The conductivity ($\sigma$) of the medium was measured with a conductivity tester (HI 98312 by Hana Instruments). Three different saline solutions mediums were assayed ($NaCl_{0.2\%}$ = 0.28 S/m, $NaCl_{0.3\%}$ = 0.58 S/m, and $NaCl_{0.6\%}$ = 1.28 S/m). The external voltage, $V_{\mathrm{ex}}$, was coupled to the saline solution using two parallel stainless-steel electrodes on the container's opposite side. The communication circuit picked-up the voltage $I_{\mathrm{im}}$ using two spherical stainless-steel electrodes separated by a known inter-electrode distance ($S$). Each electrode was laser welded to a 5 cm piece of 32 AWG enameled copper wire. We used three different electrode diameters (ø): 0.5 mm, 1 mm, and 1.5 mm.

The $Z$-parameters (4.1) for the described geometry can be analytically determined [113]. Because, on the one hand, the relative permittivity of the saline solution is low ($\epsilon_{\mathrm{r}} = 80$), and on the other hand, the applied frequency is above 1 MHz, the medium has been approximated as a pure resistive medium. Therefore, the external impedance considering $I_{\mathrm{im}} = 0$ is calculated as

$$Z_{\mathrm{ex}} = \frac{L}{\sigma WD}. \tag{6.19}$$

Assuming an orthogonal alignment between $\vec{S}$ and the external electrodes plates, the impedance $Z_{\mathrm{exim}}$ can be calculated as

$$Z_{\mathrm{exim}} = \frac{|\vec{S}|}{\sigma WD}. \tag{6.20}$$

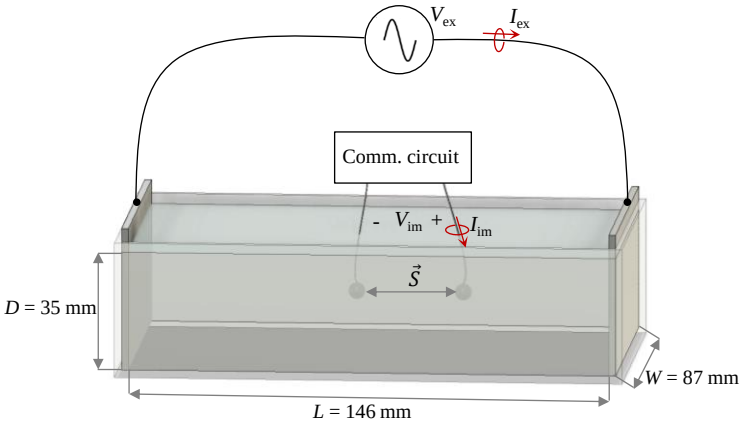


**Fig. 6.4.** Illustration of the experimental *in vitro* setup. The container was filled with homogeneous saline solution acting as a transmission medium. The external voltage was coupled using two plate electrodes placed on opposite sides of the container. As implant electrodes, we used two spherical stainless-steel electrodes.

Furthermore, considering that both spherical electrodes had the same ø, if $|\vec{S}| \gg$ ø, the resistance between both electrodes ($Z_{\mathrm{im}}$) can be approximated as

$$Z_{\mathrm{im}} = \frac{1}{\pi\sigma\text{ø}}. \tag{6.21}$$

Introducing (6.19)-(6.21) into (4.1), the two-port model for the described geometry is

$$\begin{pmatrix} V_{\mathrm{ex}} \\ V_{\mathrm{im}} \end{pmatrix} = \begin{pmatrix} \frac{L}{\sigma WD} & \frac{|\vec{S}|}{\sigma WD} \\ \frac{|\vec{S}|}{\sigma WD} & \frac{1}{\pi\sigma\text{ø}} \end{pmatrix} \begin{pmatrix} I_{\mathrm{ex}} \\ I_{\mathrm{im}} \end{pmatrix}, \tag{6.22}$$

The external voltage was applied as short bursts of high frequency (6.78 MHz) sinusoidal signals. The frequency of 6.78 MHz was chosen because it is above the safety threshold to avoid neuromuscular stimulation (5 MHz [39], [79]), and it corresponds to the central frequency of the first ISM band. To avoid overheating, the voltage was applied as a short burst. The burst duration ($B$) was 10 ms

and it was applied at a repetition frequency (*F*) of 10 Hz. The voltage amplitude was adjusted to obtain an averaged SAR of 2 W/kg. If both external plates produced a uniform electric field between them, the SAR can be determined using (2.7).

The voltage applied through the external electrodes was obtained using an arbitrary function generator (BK4065 from B&K Precision) connected to a custom-made class AB power amplifier. The applied voltage was measured on the external electrodes using an active differential probe (TA043 from Pico Technology, St Neots, UK). The current was measured using an ac/dc current probe (TCP2020 from Tektronix, Inc.). The wire connecting one of the external electrodes was wrapped five times around the current probe to increase the sensitivity of the current measurement. Both the voltage and current probes were plugged into a floating USB oscilloscope (5244D from Pico Technology, St Neots, UK). The signals were acquired during 2 ms using a sampling frequency of 125 MHz and a rectangular window. The resolution was 15 bits per channel, and the full scale (*FS*) was 200 V and 2 A, respectively.

Since the power amplifier slightly modifies its voltage amplification factor as a function of its current, in this work we measure both the output voltage and the external current and calculate the impedance to eliminate this error. Hence, we studied the impedance changes as a function of $I_{\mathrm{im}}$ instead of $I_{\mathrm{ex}}$. Hence, the previous model (6.10) was rearranged to determine $Z_{\mathrm{ex}}$ as a function of $I_{\mathrm{im}}$ (i.e., $Z'_{\mathrm{ex}}$)

$$Z'_{\mathrm{ex}} = Z_{\mathrm{ex}} - Z_{\mathrm{exim}} \frac{I_{\mathrm{im}}}{I_{\mathrm{ex}}}. \tag{6.23}$$

Introducing (6.7) and (6.8) into (6.23) the obtained impedance model is

$$Z'_{\mathrm{ex}} = Z_{\mathrm{ex}} + \frac{Z_{\mathrm{exim}}}{Z_{\mathrm{ex}}} \frac{V_{\mathrm{Th}} - 2v_{\mathrm{D}}}{Z_{\mathrm{Th}} + R_{\mathrm{M}} + 2Z_{\mathrm{C}}} \sqrt{D}. \tag{6.24}$$

To obtain the experimental value of $Z'_{\mathrm{ex}}$ and avoid introducing noise by dividing by values close to zero, the measured $v_{\mathrm{ex}}$ and $i_{\mathrm{ex}}$ signals

were root mean square averaged over 152 ns (i.e., 19 samples). This value includes at least one complete period at 6.78 MHz. Then, the resistance was determined using Ohm's law.

Regarding the noise sources, considering the analytical expressions introduced in subsection 6.2.3, for the worst-case scenario studied here (i.e., $NaCl_{0.2\%}$), the voltage Johnson-Nyquist noise (6.12) of $Z_{ex}$ (171 Ω at 298.15 K) is $N_{v\text{-}JN} = 2.8 \cdot 10^{-18}$ $V^2/Hz$, and $N_{i\text{-}JN} = 9.6 \cdot 10^{-23}$ $V^{2/}Hz$ (6.13). Regarding the quantization noise (6.13), considering $N = 500$ Hz (i.e., a temporal window of 2 ms), the voltage measurement has a one-sided power spectral density noise of $1.24 \cdot 10^{-8}$ $V^2/Hz$, and $1.24 \cdot 10^{-12}$ $V^2/Hz$ for the current measurement. Thus, clearly, the main source of noise is the quantization of the voltage measurement.

To obtain the experimental noise, an external sinusoidal voltage of 6.78 MHz, and 25 $V_{rms}$ was applied through the external electrodes (Fig. 6.4). The medium conductivity was 0.58 S/m. Both $V_{ex}$ and $I_{ex}$ were recorded using a window of 2 ms, and the rms value of these parameters was calculated as stated. Finally, the power spectral density of the impedance was calculated by determining its periodogram and averaging the results from 1 kHz to 1 MHz, obtaining that $N_0$ was $1.21 \cdot 10^{-8}$ $\Omega^2/Hz$.

### 6.2.5 *Measurement of $\Delta Z_{ex}$*

To measure the variation of $Z'_{ex}$ ($\Delta Z_{ex}$) as a function of $I_{im}$, the transmitted digital data was a square train signal that toggled the MOSFET $M_1$ from its cutoff region to its linear region (i.e., '0101010'). Therefore, the modulated signal's frequency spectrum contains the carrier's components, the noise, and the frequency components of the square pulse train.

Considering a square pulse train defined as in (6.25)

$$\Pi(t) = \begin{cases} A, & |t| < \dfrac{T_\mathrm{p}}{2} \\ 0, & |t| \geq \dfrac{T_\mathrm{p}}{2} \end{cases}, \quad -\frac{T_\mathrm{p}}{2} < t \leq \frac{T_\mathrm{p}}{2} \tag{6.25}$$

where $t$ is the time, $A$ is the pulse amplitude, and $T_\mathrm{p}$ is the pulse duration. Since (6.25) is even, the Fourier series of $\Pi(t)$ is

$$x_\mathrm{T}(t) = a_0 + \sum_{n=1}^{\infty} a_n \cos(n\omega_0 t), \tag{6.26}$$

where $a_0$ is the averaged signal. The parameters $a_n$ can be calculated as

$$\begin{aligned} a_n &= \frac{2}{T_\mathrm{p}} \int_{-\frac{T}{2}}^{\frac{T}{2}} A \cos(n\omega_0 t)\, dt \\ &= 2\frac{A}{n\pi} \sin\left(\frac{n\pi}{2}\right). \end{aligned} \tag{6.27}$$

The first harmonic (i.e., $n = 1$) will have a value of $2A/\pi$. Therefore, to determine the variation of (6.24) related to the load modulation, the Fourier transform of the measured rms impedance is first calculated. Then, to determine $\Delta Z_\mathrm{ex}$, the frequency component with a frequency of $1/T_\mathrm{p}$ (i.e., $n = 1$ in (6.26)) is multiplied by $\pi/2$ to recover the $\Delta Z_\mathrm{ex}$ amplitude value.

### 6.2.6 *Communication circuit*

The described circuit in the inlet of Fig. 6.1 was implemented on a 40×30 mm two-layer PCB (see Fig. 6.5) using on-the-shelf components. The diodes ($D_{1-5}$) were small-signal fast switching diodes (1N4148 from Vishay Semiconductors) having a typical forward voltage ($v_\mathrm{D}$) of 0.75 V (for a current of 10 mA at 25 ºC). The MOSFETs ($M_{1\text{-}2}$) were small signal MOSFETs (BS170F by On Semiconductor).

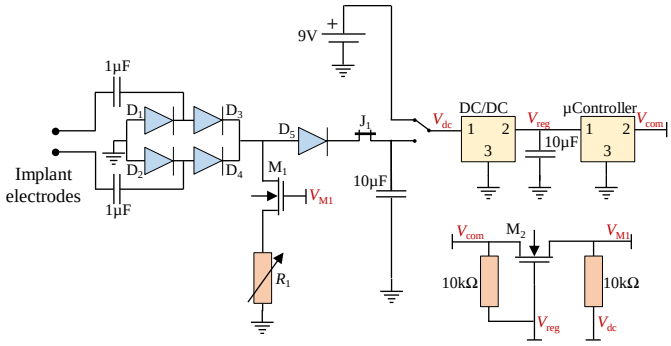


**Fig. 6.5.** Schematic of the implemented communication circuit. The circuit can be powered by volume conduction or using a 9 V external battery.

For $M_1$, the maximum value of $R_{SW}$ is 5 Ω, so we considered $R_{SW}$ = 5 Ω. To ensure that $M_1$ operates as a switch without limiting the flowing current through the channel (i.e., in the cutoff region for a '0' and in the ohmic region for a '1'), the $M_2$ MOSFET acts as a bidirectional logic level shifter, so it increases the $V_{GS}$ of $M_1$.

The digital part of the circuit could be powered using two different methods 1) using volume conduction and 2) using an external 9 V battery. Unless otherwise stated, the circuit was powered from the 9 V battery, and $J_1$ was disconnected. The dc voltage was regulated using a low dropout regulator (MIC5236 from Microchip) to obtain a fixed voltage of 3.3 V. The operation mode of $M_1$ was controlled by a low-power microcontroller (ATtiny-85 from Microchip). The clock frequency of the microcontroller was 20 MHz, and three different communication frequencies were used (125 kbps, 250 kbps, and 1050 kbps).

## 6.3 Results

### 6.3.1 *Dependency on inter-electrode distance*

In Fig. 6.6, we studied the influence of the inter-electrode distance, $|\vec{S}|$, in the impedance variation and in the BER. The saline solution resembled the properties of the muscle tissue at 6.78 MHz (NaCl at 0.3%, $\sigma = 0.58\,\mathrm{S/m}$). The external voltage, $V_{\mathrm{ex}}$, was adjusted to obtain an averaged SAR of 2 W/kg ($V_{\mathrm{peak}} = 38.3\,V$, $F = 100$ Hz, and $B = 1$ ms). To get accurate results the one-sided power spectral density ($N_0$) was the experimental one (i.e., $N_0 = 1.21 \cdot 10^{-8}\ \Omega^2$/Hz, see subsection 6.2.4). Unless otherwise stated, this value has been used in the rest of the results section.

The implant electrodes had a diameter of 1 mm. They were submerged to a depth of 10 mm, and the vector formed by both electrodes ($\vec{S}$) was orthogonally aligned with the external electrodes. The inter-electrode distance was swept from 10 mm to 40 mm in steps of 5 mm. The electrode wires were attached to a 3-d printed support to ensure both the orthogonally and the fixed inter-electrode distance.

The results show that the analytical model accurately reproduces the experimental trend, especially for distances above 25 mm. The results of Fig. 6.6 show that for these values, the experimental measurements are within the shaded area (i.e., they have a relative error below $\pm 10$ % regarding the analytical expression). For inter-electrode distances below 25 mm, although the analytical model still follows the experimental values, the relative error is above $\pm$10%. The error between the analytical model and the experimental measurements for inter-electrode distances below 25 mm may be partially associated with the fact that the amplitude of the communication signal is close to that of the noise. Therefore, when the experimental amplitude of $Z_{\mathrm{ex}}$ was determined for short distances, a significant part of the obtained value was due to system noise.

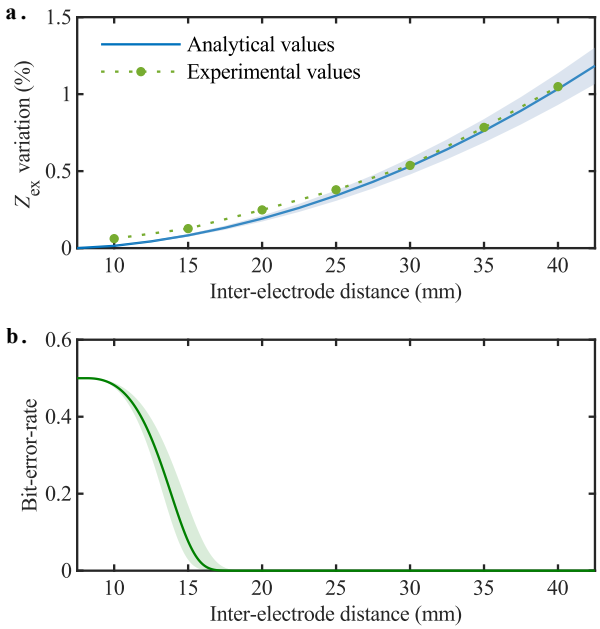


**Fig. 6.6.** Influence of the inter-electrode distance in (**a)** the impedance variation (shaded blue: ±10%, line: theoretical value, markers: experimental values), and in (**b)** the analytical BER calculated as (6.16) (shaded green: ±50%).

Additionally, the results have also shown that the BER can be reduced by increasing the inter-electrode separation. This trend is described in the analytical model. Equation (6.24) of the model describes how incrementing the inter-electrode spacing increases $V_{\mathrm{Th}}$, and consequently, $Z_{\mathrm{ex}}$. When $V_{\mathrm{Th}} \gg 2v_{\mathrm{D}}$, the variation of $Z_{\mathrm{ex}}$ increases at squared with the $Z_{\mathrm{exim}}$ and consequently with the inter-electrode distance. Then, since $E_{\mathrm{s}}$ increases with inter-electrode distance, the BER is reduced (6.16).

### 6.3.2 *Dependency on electrode diameter*

To determine the influence of the device width, we studied three different electrode diameters: 0.5 mm, 1 mm, and 1.5 mm (Fig. 6.7).

For each diameter, the inter-electrode distance was swept from 10 mm to 40 mm in steps of 5 mm. The conductivity of the medium and the applied voltage were the same as those in Fig. 6.6.

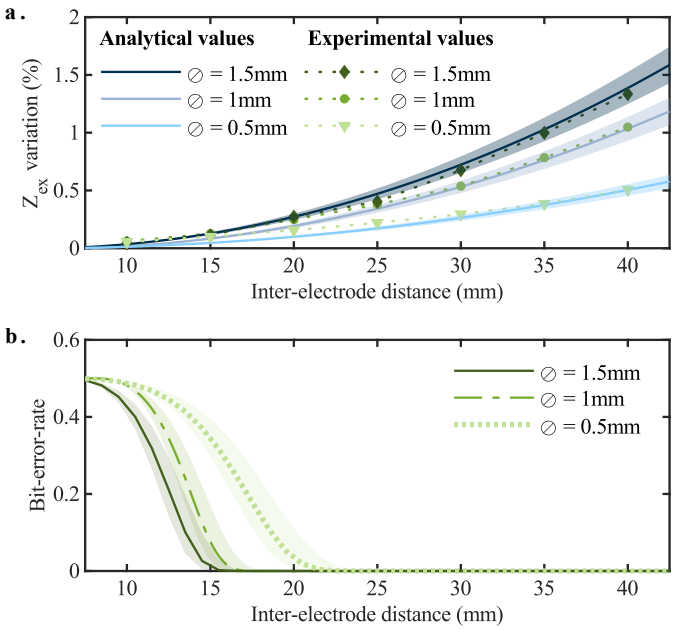


**Fig. 6.7.** Influence of the electrode diameter (ø) in (**a)** the impedance variation (shaded blue: ±10%, line: theoretical value, markers: experimental values), and in (**b)** the analytical BER. Three different diameters were considered: 0.5 mm, 1 mm, and 1.5 mm (shaded green: ±50%).

Since the electrode diameter is inversely proportional to the implant resistance ($Z_{22}$) (6.21), the implant current decreases with the electrode diameter (6.10), and consequently, the variation of the external resistance is also reduced. The analytical values of $Z_{22}$ for the three different diameters were $Z_{22}(\emptyset_{0.5}) = 1098\ \Omega$, $Z_{22}(\emptyset_{1}) = 549\ \Omega$, and $Z_{22}(\emptyset_{1.5}) = 366\ \Omega$. To get a BER of less than 0.01 for a diameter of 0.5 mm, an inter-electrode distance of at least 21 mm is required, while for the 1.5 mm case, the inter-electrode distance must be at least 15 mm.

### 6.3.3 *Dependency on modulation load* ($R_1$)

In more realistic scenarios, when the implant is also powered by volume conduction, directly shorting the diode bridge for communication purposes may not be suitable: while the bridge is shorted, the implant cannot harvest energy for powering purposes. Therefore, it is recommended to limit the maximum communication current. To study how the current limitation influences the communications, we have plugged an external variable resistance ($R_1$) in series with the communication MOSFET ($M_1$) (see Fig. 6.5). The value of $R_1$ was swept from 100 Ω to 2 kΩ in steps of 100 Ω. The inter-electrode distance was kept constant at 30 mm. The diameter of the electrodes was 1 mm, and the medium conductivity was 0.58 S/m. The results are shown in Fig. 6.8.

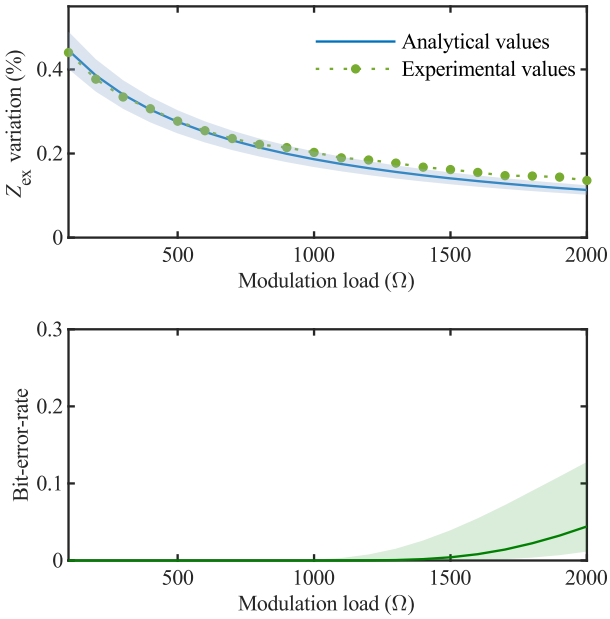


**Fig. 6.8.** Influence of the modulation load in (**a)** the impedance variation (shaded blue: ±10%, line: theoretical value, markers: experimental values), and in (**b)** the analytical BER calculated as (6.16) (shaded green: ±50%).

For $R_1 < 1.2\ \text{k}\Omega$, the analytical model matches the experimental results with an error of less than $\pm 10\%$. For values above 1.2 kΩ, produces a BER greater than $1 \cdot 10^{-4}$. As in the previous cases, when the BER is higher than this value, a slight divergence appears between the theoretical model and the experimental results.

To illustrate that part of the picked-up power can be used for powering purposes, it was considered the case when $R_1 = 600\Omega$. With this load, a BER of $2.2 \cdot 10^{-17}$ was obtained, and the analytical current, $I_{\text{m}}$, was 2.3 mA. Applying the Joule law, the power dissipated by $R_1$ when the MOSFET is in the linear region was 3.2 mW.

### 6.3.4 *Medium conductivity*

The medium conductivity is a relevant property for load modulation based on volume conduction since the model impedances are related to this value. For the case studied here, the conductivity of the medium was uniform. Therefore, for the used geometry, the two-port impedances were inversely proportional to the conductivity (6.19)-(6.21).

Three different saline solutions were assayed ($\text{NaCl}_{0.2\%}$ = 0.28 S/m, $\text{NaCl}_{0.3\%}$ = 0.58 S/m, and $\text{NaCl}_{0.6\%}$ = 1.28 S/m). These conductivities resemble the conductivity of several biological tissues at 6.78 MHz (e.g., $\sigma(\text{NaCl}_{0.2\%}) \approx \sigma_{\text{Gray matter}}$, $\sigma(\text{NaCl}_{0.3\%}) \approx \sigma_{\text{Muscle}}$, and $\sigma(\text{NaCl}_{0.6\%}) \approx \sigma_{\text{Small intestine}}$). The inter-electrode distance was swept from 10 mm to 40 mm in steps of 5 mm. The implant electrodes had a diameter of 1 mm. Furthermore, the external voltage was the same as the previous cases for the three different saline solutions.

For the studied geometry, the results show that the conductivity does not influence the variation of the external impedance (Fig. 6.9). Nevertheless, conductivity increases the BER. For instance, to get a BER below 0.01 for a $\sigma$ = 0.28 S/m an inter-electrode distance of

13 mm is required, while for $\sigma$ = 1.28 S/m, 22 mm is required.

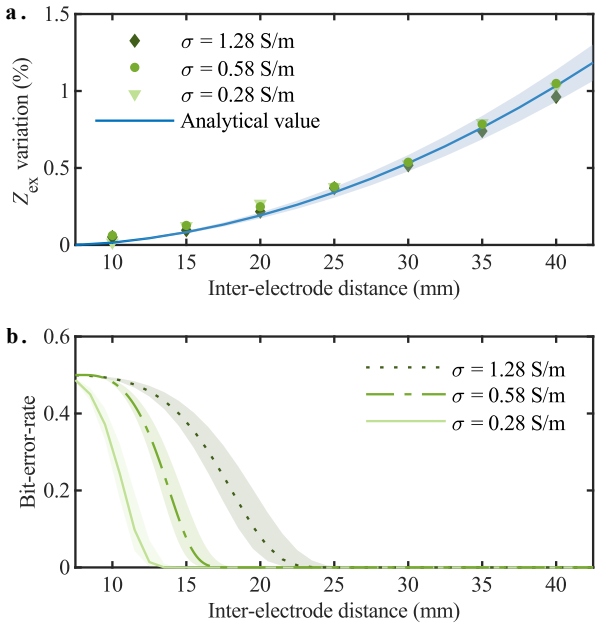


**Fig. 6.9.** Influence of the medium conductivity in (**a)** the impedance variation (shaded blue: ±10%, line: theoretical value, markers: experimental values), and in (**b)** the analytical BER. Three different medium conductivities were considered: 0.28 S/m, 0.58 S/m, and 1.28 S/m (shaded green: ±50%).

This is attributed to the fact that, although the variation in impedance was not related to the medium conductivity, the absolute value of the bit energy reduces with the conductivity.

### 6.3.5 *Communication frequency*

To study the influence of the communication frequency, we have considered three different frequencies ($f_{\mathrm{comm}}$): 125 kbps, 250 kbps, and 1000 kbps. The medium conductivity was 0.58 S/m, and the electrode diameter was 1 mm. The inter-electrode distance was swept from 10 mm to 40 mm in steps of 5 mm (Fig. 6.10).

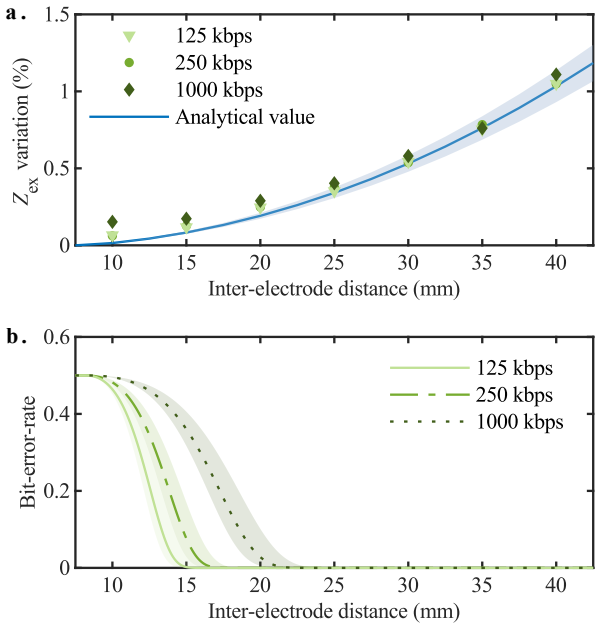


**Fig. 6.10.** Influence of the communication frequency in (**a)** the impedance variation (shaded blue: ±10%, line: theoretical value, markers: experimental values), and in (**b)** the analytical BER. Three different communication frequencies were considered: 125 kbps, 250 kbps, and 1000 kbps (shaded green: ±50%).

The experimental results confirm that the communication frequency does not influence the variation of the external impedance when the BER is below 0.01. However, as equation (6.18) states, the bit energy is directly related to the communication frequency. Therefore, the BER is also dependent on the communication frequency (6.16). For instance, having a frequency of 125 kbps to get a BER below 0.01, an inter-electrode spacing of 14.7 mm is required, while for 1000 kbps, 20.8 mm is required to get the same BER.

### 6.3.6 *Demonstration of demodulation*

Although the design of an efficient demodulation system is beyond the scope of this work, a demodulator based just on threshold comparison has been used for verification purposes. Firstly, the algorithm determined the threshold value as the mean value of the impedance vector. Then, the impedance vector was filtered using a moving average filter with a window length of one communication bit divided by a factor of twenty. Then the averaged vector was iterated, and each element was compared with the threshold value. If the comparison result was equal to or less than the threshold, a binary value of 1 was assigned. Otherwise, a 0 was assigned. Thus, a digitalized signal was obtained.

To illustrate the demodulation, we used a saline solution with $\sigma$ = 0.58 S/m. The device electrodes have a dimeter of 1 mm. Four inter-electrode distances were measured: 10 mm, 20 mm, 30 mm, and 40 mm. The communication frequency was 250 kbps. In this case, instead of transmitting a communication signal that alternates ones and zeros, the signal was the binary codification of the ASCII characters "HELLO" (i.e., 0100 1000 0100 0101 0100 1100 0100 1100 0100 1111 in binary). The results for a complete frame of the transmitted message are shown in Fig. 6.11.

Based on the results obtained in Fig. 6.6, the demodulation for 10 mm separations is expected to have a high randomness component as its BER is close to 0.5. For inter-electrode distances of 30 mm and 40 mm, it is expected that the demodulator will be able to obtain the transmitted message correctly. The demodulation results obtained in Fig. 6.11 coincide with what was expected since, qualitatively, the demodulation for 10 mm has a relevant randomness pattern. In contrast, the 40 mm signal demodulation reproduced the transmitted message correctly.

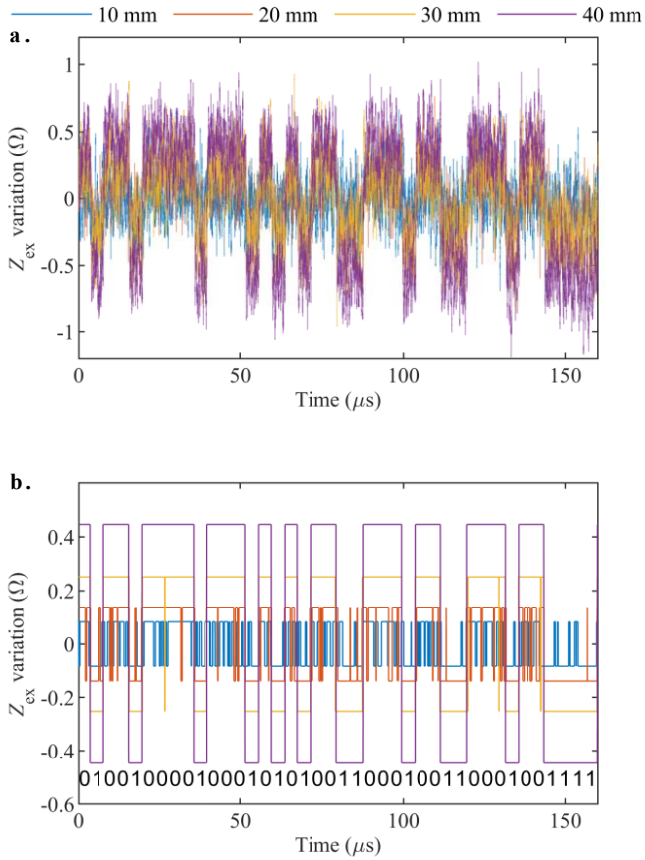


**Fig. 6.11. a.** RMS impedance variation for four different inter-electrode distances: 10 mm, 20 mm, 30 mm, and 40 mm, when the transmitter sent the previous message. The dc component of these signals was intentionally removed to facilitate the data comparison. **b**. Digitalization of the (**a**) signals. The amplitude of each signal was averaged from (**a**) to allow the comparison between them.

## 6.4 Discussion

The results obtained from the analytical model and demonstrated *in vitro* show that the modulation circuit proposed in this chapter can transmit data with a very low error rate if the implant has a separation of a few centimeters between its electrodes. Furthermore, the

analytical model proposed here, based on the two-port model of Chapter 4, allows accurately determining $\Delta Z_{ex}$ (i.e., with an error less than ±10 %) if the BER is lower than approximately $1 \cdot 10^{-4}$. Part of this error is related to having a high BER implies that $E_s$ and $N_0$ are of the same order of magnitude. Consequently, for the experimental results, when $\Delta Z_{ex}$ is calculated, this value includes a non-negligible part of noise that produces part of the divergence with the model. However, the fact of having divergences between the analytical model and the experimental results when the BER is above $1 \cdot 10^{-4}$ is not especially relevant since most of the systems will be designed to get a BER equal to or lower than this value. As the previous chapters stated, to power threadlike AIMDs by using coupling based on volume conduction a length above 20 mm is required. Therefore, a low BER is expected in most of the applications.

The model proposed in this chapter can be used to optimize the design of future threadlike implants. Furthermore, although the demonstration was intentionally done using a simple geometry and a homogeneous medium to determine the two-port parameters analytically, the saline two-port parameters emulate the *in vivo* values obtained in Chapter 5 properly. For instance, the mean of the values of the two-port values of the upper arm considering a perpendicular alignment (Table 5.4) are: $Z_{ex}$ = 81.6-24.6i Ω, $Z_{im}$ = 436-6.4 Ω, and $Z_{exim}$ = 16.8-3.4i Ω. These values are close to the values obtained considering a $\sigma$ = 0.58 S/m, $\emptyset$ = 1 mm, and $|\vec{S}|$ = 30 mm, so $Z_{ex}$ = 82.7 Ω, $Z_{im}$ = 548 Ω, and $Z_{exim}$ = 17 Ω.

Load modulation based on volume conduction has the advantage that it does not require separate pickup elements for communicating and powering purposes [70]. The results in Fig. 6.8 showed that, while the BER was kept low ($2.2 \cdot 10^{-17}$), the implant resistance ($R_1 = 600\ \Omega$) dissipated 3.2 mW when the MOSFET conduced, this is 1.6 mW considering that the communication had a duty cycle of 0.5. This power although is lower than the maximum power that an implant with this dimensions can obtain during the burst (4.4 mW see Chapter 3.2.3) is enough to power most active medical devices [74]. Nevertheless, it is relevant to highlight that the implant just will receive this power when the external burst is applied. If more power

is needed or the implant needs to be fed continuously, the SAR can be increased (for persons in controlled environment, 10 W/kg on head and torso, and 20 W/kg in the limbs [39]) so that the burst can be longer and the implant will obtain more power [136].

Although communications of hundreds of kbps have been used, the total amount of information transmitted is limited because it can only be transmitted when bursts are applied. In this work, the ratio between the duration of the burst ($B$) and the inverse of the repetition frequency of the burst ($F$) was 0.1. This ratio can be increased using two different approaches. The first approach consists of maintaining the same SAR (2 W/kg) while reducing the peak value of $V_{\mathrm{ex}}$. The main drawback of this method is that reducing the peak voltage reduces the performance of the communications. The second approach consists of allowing a higher SAR. The SAR increases linearly with the burst ratio if the $V_{\mathrm{peak}}$ is kept constant. Therefore, for a SAR of 10 W/kg, the burst ratio is 0.5, and for a SAR of 20 W/kg, $V_{\mathrm{ex}}$ can be applied continuously.

The results showed that although the impedance variation was mainly independent of the medium's conductivity, the BER increases as the conductivity increased (Fig. 6.9). We obtained this outcome because, for the described scenario, the noise is mainly related to the quantization noise of the voltage measurement. Furthermore, increasing the conductivity lowers the impedance. Hence, if the analyzed variable is the impedance, the signal-noise ratio is reduced, and the BER is increased. This drawback can be minimized by having a voltage source whose value is not affected by load variations, therefore it is only necessary to analyze the current.

## 6.5 Conclusions

This study supports volume conduction-based load modulation as a passive communication method for implantable medical devices that allows transmission frequencies of hundreds of kbps. Furthermore, in this work, we have introduced and modeled a simple ac modulator

switcher that can be easily implement in most of current biomedical implants. The obtained model allows for determining the estimated BER that the system will have. Moreover, as long as the BER is small, the model accurately predicts the value of the modulated signal.

The results show that using the described method, an implanted device can transfer data to an external system separated by several centimeters with a low BER, provided that the implant electrodes are separated several centimeters (> 20 mm) apart from each other. Furthermore, for the described method, the same pair of electrodes can be used for powering the device and for transmitting data. Hence, the implant does not require extra bulky components and can be shaped like a thin (< 1 mm), elongated (> 20 mm), and flexible body that can be injected percutaneously.

The proposed model can be used to optimize the main features of the implantable medical device (length, diameter, transmission frequency, and the value of the implant modulation load) as a function of the transmission parameters of the channel. Thus, we consider that the model proposed here can set the theoretical framework that describes load modulation communication based on volume conduction and can pave the development of new minimally invasive implants.

# CHAPTER 7

## Conclusions

## 7.1 General conclusions

This thesis contributes to setting the bases of a theoretical framework of coupling based on volume conduction for powering threadlike implants. The obtained models ease the development of new minimally invasive devices powered by volume conduction.

Two main analytical and numerical models to describe coupling based on volume conduction have been developed and validated. These models can be classified into two kinds, as a reception model (Chapter 3), and as a full transmission model (Chapter 4). The receiver models determine the maximum ac and dc power an implant can obtain. It also analytically identifies the main local features involved in coupling based on volume conduction. The full transmission model, besides determining the PDL, allows for determining the PTE of the system. However, in this case, the system's physical parameters cannot be directly related to the model values since they are numerically determined.

The provided models have shown that by applying electric fields, which fulfill the safety standards, powers in the order of milliwatts can be obtained by thin implants (i.e., with sub-millimeter diameters), if their electrodes are separated few centimeters. Besides being minimally invasive *per se*, this threadlike conformation favors the percutaneous deployment of the implants, so surgical issues are minimized.

Although coupling based on volume conduction allows powering of deeply seated implants, the results have shown that this method has exceptionally low PTE (usually below 1%). Nevertheless, this efficiency can be increased when multiple implants are present. That is because, first, implants can be placed close together (i.e., a few millimeters apart) without significant decay in their PDL. And second, multiple implants can be powered by coupling the same external energy into the tissues.

This thesis also presented an in-human validation of coupling based on volume conduction to power digital electronic circuits, showing

that powers of milliwatts can be obtained by thin electrodes. In addition, by using MRI images of the participants and a FEM solver, the parameters of the model presented in Chapter 4 were obtained. The comparison between the model results and the experimental measurements showed that the proposed model could properly estimate the PDL and the PTE. Consequently, it was validated that this modeling process can model intrabody transmission channels.

Additionally, this thesis studied the use of load modulation as a passive communication method, based on volume conduction. A simple modulation circuit consisting of a diode bridge with a variable resistor in series with a MOSFET has been proposed. Furthermore, the analytical expression of the modulation circuit and the transmission link was obtained. This model was demonstrated *in vitro*. The results showed that transferring data from deeply seated implants to an external system is feasible using threadlike implants. Although, like in the power transmission case, to get a low BER considering transmission frequencies of hundreds of kbps, the implant electrodes must be separated a few cm (i.e., > 2 cm). Thus, it has been demonstrated that the proposed system can use volume conduction for communicating and powering the implantable device.

## 7.2 Future perspectives

As stated in the introduction, deploying networks of minimally invasive implants has the potential to revolutionize the treatment and monitoring of several medical pathologies. This thesis has already contributed to smoothing the path of developing minimally invasive implants since the results presented here have allowed the development of a new generation of eAXONs, being the first generation of submillimetric eAXONs (diameter = 0.97 mm, length = 35 mm).

The obtained model presented in Chapter 4 can be adapted for any anatomical position, as we did in Chapter 5, where it was adapted to model coupling based on volume conduction in human upper and lower limbs. However, since most medical implants are placed within the human head and torso, it is necessary to follow a similar

procedure to the one described in Chapter 5 to apply volume conduction for these applications. Besides the anatomic differences, the main difference between the limbs, the head, and the torso is that while the maximum SAR on limbs for persons in controlled environments is 20 W/kg, in the head and torso, this safety threshold is reduced to 10 W/kg. Moreover, since the models presented in this thesis have been developed not only for neuromuscular applications but for generic AIMD applications, to the best of our knowledge, the provided models are also being used to develop minimally invasive implants that monitor physiological parameters and use coupling based on volume conduction for powering and for communicating purposes.

Although the transmission link optimization was out of the scope of this thesis, it is one of the most relevant factors for developing future applications. One of the parameters that have a more significant role in the efficiency optimization is the arrangement of the external electrodes. Here, it is anticipated that using multiple external electrodes will improve the system efficiency. This is due to, on the one hand, in specific scenarios, having multiple external electrodes can allow focalizing the electric field in a region. And, on the other hand, for scenarios that include multiple distributed implants, the system can be optimized by selecting the proper external electrodes based on the implants power requirements for each time.

# References

[1] V. S. Mallela, V. Ilankumaran, and S. N. Rao, “Trends in cardiac pacemaker batteries,” *Indian Pacing Electrophysiol. J.*, vol. 4, no. 4, pp. 201–212, 2004.

[2] J. S. Ho *et al.*, “Wireless power transfer to deep-tissue microimplants.,” *Proc. Natl. Acad. Sci. U. S. A.*, vol. 111, no. 22, pp. 7974–9, 2014, doi: 10.1073/pnas.1403002111.

[3] M. S. Okun, “Deep-Brain Stimulation for Parkinson’s Disease,” *N. Engl. J. Med.*, vol. 367, no. 16, pp. 1529–1538, Oct. 2012, doi: 10.1056/NEJMct1208070.

[4] B. S. Wilson and M. F. Dorman, “Cochlear implants: A remarkable past and a brilliant future,” *Hear. Res.*, vol. 242, no. 1–3, pp. 3–21, 2008, doi: 10.1016/j.heares.2008.06.005.

[5] J. D. Weiland, A. K. Cho, and M. S. Humayun, “Retinal prostheses: Current clinical results and future needs,” *Ophthalmology*, vol. 118, no. 11, pp. 2227–2237, 2011, doi: 10.1016/j.ophtha.2011.08.042.

[6] L. W. Kleiner, J. C. Wright, and Y. Wang, “Evolution of implantable and insertable drug delivery systems,” *J. Controlled Release*, vol. 181, pp. 1–10, 2014, doi: 10.1016/j.jconrel.2014.02.006.

[7] L. Yu, B. J. Kim, and E. Meng, “Chronically implanted pressure sensors: Challenges and state of the field,” *Sens. Switz.*, vol. 14, no. 11, pp. 20620–20644, 2014, doi: 10.3390/s141120620.

[8] X. Navarro, T. B. Krueger, N. Lago, S. Micera, T. Stieglitz, and P. Dario, “A critical review of interfaces with the peripheral nervous system for the control of neuroprostheses and hybrid bionic systems,” *J. Peripher. Nerv. Syst.*, vol. 10, no. 3, pp. 229–258, 2005, doi: 10.1111/j.1085-9489.2005.10303.x.

[9] X. Li, W. A. Serdijn, W. Zheng, Y. Tian, and B. Zhang, “The injectable neurostimulator: An emerging therapeutic device,” *Trends Biotechnol.*, vol. 33, no. 7, pp. 388–394, 2015, doi: 10.1016/j.tibtech.2015.04.001.

[10] W. M. Grill, S. E. Norman, and R. V. Bellamkonda, "Implanted neural interfaces: biochallenges and engineered solutions.," *Annu. Rev. Biomed. Eng.*, vol. 11, pp. 1–24, 2009, doi: 10.1146/annurev-bioeng-061008-124927.

[11] J. L. Skousen, S. M. E. Merriam, O. Srivannavit, G. Perlin, K. D. Wise, and P. A. Tresco, "Reducing surface area while maintaining implant penetrating profile lowers the brain foreign body response to chronically implanted planar silicon microelectrode arrays," *Prog. Brain Res.*, vol. 194, pp. 167–180, 2011, doi: 10.1016/B978-0-444-53815-4.00009-1.

[12] A. Kiourti and K. S. Nikita, "A review of in-body biotelemetry devices: Implantables, ingestibles, and injectables," *IEEE Trans. Biomed. Eng.*, vol. 64, no. 7, pp. 1422–1430, 2017, doi: 10.1109/TBME.2017.2668612.

[13] G. E. Loeb, R. A. Peck, W. H. Moore, and K. Hood, "BION™ system for distributed neural prosthetic interfaces," *Med. Eng. Phys.*, vol. 23, no. 1, pp. 9–18, Jan. 2001, doi: 10.1016/S1350-4533(01)00011-X.

[14] P. M. Lee, Z. Xiong, and J. Ho, "Methods for powering bioelectronic microdevices," *Bioelectron. Med.*, vol. 1, no. 3, 2018, doi: 10.2217/bem-2018-0005.

[15] L. S. Y. Wong, S. Hossain, A. Ta, J. Edvinsson, D. H. Rivas, and H. Nääs, "A very low-power CMOS mixed-signal IC for implantable pacemaker applications," *IEEE J. Solid-State Circuits*, vol. 39, no. 12, pp. 2446–2456, 2004, doi: 10.1109/JSSC.2004.837027.

[16] D. C. Ng, S. Bai, J. Yang, N. Tran, and E. Skafidas, "Wireless technologies for closed-loop retinal prostheses," *J. Neural Eng.*, vol. 6, no. 6, 2009, doi: 10.1088/1741-2560/6/6/065004.

[17] J. R. Buckett, P. H. Peckham, G. B. Thrope, S. D. Braswell, and M. W. Keith, "A Flexible, Portable System for Neuromuscular Stimulation in the Paralyzed Upper Extremity," *IEEE Trans. Biomed. Eng.*, vol. 35, no. 11, pp. 897–904, 1988, doi: 10.1109/10.8669.

[18] M. Armand and J.-M. Tarascon, "Building better batteries," *Nature*, 2008, doi: 10.1038/451652a.

[19] W. J. Heetderks, “RF Powering of Millimeter- and Submillimeter-Sized Neural Prosthetic Implants,” *IEEE Trans. Biomed. Eng.*, vol. 35, no. 5, pp. 323–327, 1988, doi: 10.1109/10.1388.

[20] L. Becerra-Fajardo, M. Schmidbauer, and A. Ivorra, “Demonstration of 2 mm Thick Microcontrolled Injectable Stimulators Based on Rectification of High Frequency Current Bursts,” *IEEE Trans. Neural Syst. Rehabil. Eng.*, vol. 25, no. 8, pp. 1343–1352, 2017, doi: 10.1109/TNSRE.2016.2623483.

[21] C. Chakkaravarthy, A. K. A. Waheed, and H. V. K. Udupa, “Zinc-air alkaline batteries - A review,” *J. Power Sources*, 1981, doi: 10.1016/0378-7753(81)80027-4.

[22] W. H. Ko and J. Hynecek, “Implant Evaluation of a Nuclear Power Source– Betacel® Battery,” *IEEE Trans. Biomed. Eng.*, vol. 21, no. 3, pp. 238–241, 1974, doi: 10.1109/TBME.1974.324388.

[23] V. Parsonnet, A. Villanueva, J. Driller, and A. D. Bernistein, “Corrosion of Pacemaker Electrodes,” *Pacing Clin. Electrophysiol.*, vol. 4, no. 3, pp. 289–296, 1981, doi: 10.1111/j.1540-8159.1981.tb03697.x.

[24] W. Greatbatch, “Lithium-iodine battery,” US3874929A, Apr. 01, 1975 Accessed: Jul. 06, 2022. [Online]. Available: https://patents.google.com/patent/US3874929A/en

[25] A. B. Amar, A. B. Kouki, and H. Cao, “Power approaches for implantable medical devices,” *Sens. Switz.*, vol. 15, no. 11, pp. 28889–28914, 2015, doi: 10.3390/s151128889.

[26] D. C. Bock, A. C. Marschilok, K. J. Takeuchi, and E. S. Takeuchi, “Batteries used to power implantable biomedical devices,” *Electrochimica Acta*, vol. 84, pp. 155–164, 2012, doi: 10.1016/j.electacta.2012.03.057.

[27] E. S. Takeuchi and R. A. Leising, “Lithium Batteries for Biomedical Applications,” *MRS Bull.*, vol. 27, no. 8, pp. 624–627, 2002, doi: 10.1557/mrs2002.199.

[28] M. Strasser, R. Aigner, C. Lauterbach, and T. Sturm, “Micromachined CMOS thermoelectric generators as on-chip power supply,” *Sens. Actuators Phys.*, vol. 114, no. 2–3, pp. 362–370, 2004.

[29] R. J. M. Vullers, R. van Schaijk, I. Doms, C. V. Hoof, and R. Mertens, "Micropower energy harvesting," *Solid-State Electron.*, vol. 53, no. 7, pp. 684–693, 2009, doi: 10.1016/j.sse.2008.12.011.

[30] J. Zhao and Z. You, "A shoe-embedded piezoelectric energy harvester for wearable sensors," *Sens. Switz.*, vol. 14, no. 7, pp. 12497–12510, 2014, doi: 10.3390/s140712497.

[31] C. Dagdeviren *et al.*, "Conformal piezoelectric energy harvesting and storage from motions of the heart, lung, and diaphragm," *Proc. Natl. Acad. Sci.*, vol. 111, no. 5, pp. 1927–1932, 2014, doi: 10.1073/pnas.1317233111.

[32] L. Dong *et al.*, "Flexible Porous Piezoelectric Cantilever on a Pacemaker Lead for Compact Energy Harvesting," *Adv. Mater. Technol.*, vol. 4, no. 1, 2019, doi: 10.1002/admt.201800148.

[33] B. I. Rapoport, J. T. Kedzierski, and R. Sarpeshkar, "A glucose fuel cell for implantable brain-machine interfaces," *PLoS ONE*, 2012, doi: 10.1371/journal.pone.0038436.

[34] A. Zebda *et al.*, "Single glucose biofuel cells implanted in rats power electronic devices," *Sci. Rep.*, vol. 3, 2013, doi: 10.1038/srep01516.

[35] J. C. Schuder, "Powering an artificial heart: Birth of the inductively coupled-radio frequency system in 1960," *Artif. Organs*, vol. 26, no. 11, pp. 909–915, 2002, doi: 10.1046/j.1525-1594.2002.07130.x.

[36] I. Bioelectronics, K. Agarwal, S. Member, and R. Jegadeesan, "Wireless Power Transfer Strategies for Implantable Bioelectronics," *IEEE Rev. Biomed. Eng.*, vol. 10, pp. 136–161, 2017.

[37] I. Hochmair *et al.*, "MED-EL Cochlear Implants: State of the Art and a Glimpse Into the Future," *Trends Amplif.*, vol. 10, no. 4, pp. 201–219, 2006, doi: 10.1177/1084713806296720.

[38] D. J. Griffiths, "Introduction to Electrodynamics," in *Introduction to Electrodynamics*, Harlow: Pearson Education Limited, 2014, pp. 299–359. doi: 10.1017/9781108333511.

[39] IEEE, *IEEE Standard for Safety Levels With Respect to Human Exposure to Radio Frequency Electromagnetic Fields, 3 kHz to 300 GHz*. 2019.

[40] A. K. RamRakhyani, S. Mirabbasi, and M. Chiao, "Design and optimization of resonance-based efficient wireless power delivery systems for biomedical implants," *IEEE Trans. Biomed. Circuits Syst.*, vol. 5, no. 1, pp. 48–63, 2011, doi: 10.1109/TBCAS.2010.2072782.

[41] P. Feng, P. Yeon, Y. Cheng, M. Ghovanloo, and T. G. Constandinou, "Chip-Scale Coils for Millimeter-Sized Bio-Implants," *IEEE Trans. Biomed. Circuits Syst.*, vol. 12, no. 5, pp. 1088–1099, Oct. 2018, doi: 10.1109/TBCAS.2018.2853670.

[42] D. Ahn and M. Ghovanloo, "Optimal Design of Wireless Power Transmission Links for Millimeter-Sized Biomedical Implants," *IEEE Trans. Biomed. Circuits Syst.*, vol. 10, no. 1, pp. 125–137, 2016, doi: 10.1109/TBCAS.2014.2370794.

[43] A. Ibrahim, M. Meng, and M. Kiani, "A Comprehensive Comparative Study on Inductive and Ultrasonic Wireless Power Transmission to Biomedical Implants," *IEEE Sens. J.*, vol. 18, no. 9, pp. 3813–3826, 2018, doi: 10.1109/JSEN.2018.2812420.

[44] A. S. Y. Poon, S. O'driscoll, and T. H. Meng, "Optimal frequency for wireless power transmission into dispersive tissue," *IEEE Trans. Antennas Propag.*, vol. 58, no. 5, pp. 1739–1750, 2010, doi: 10.1109/TAP.2010.2044310.

[45] M. Machnoor, E. S. Gamez Rodriguez, P. Kosta, J. Stang, and G. Lazzi, "Analysis and design of a 3-coil wireless power transmission system for biomedical applications," *IEEE Trans. Antennas Propag.*, vol. 67, no. 8, pp. 5012–5024, 2019, doi: 10.1109/TAP.2018.2883687.

[46] T. Campi, S. Cruciani, V. De Santis, F. Maradei, and M. Feliziani, "Near Field Wireless Powering of Deep Medical Implants," *Energies*, vol. 12, no. 14, 2019, doi: 10.3390/en12142720.

[47] S. Kim, J. S. Ho, and A. S. Y. Poon, "Midfield wireless powering of subwavelength autonomous devices," *Phys. Rev. Lett.*, vol. 110, 2013, doi: 10.1103/PhysRevLett.110.203905.

[48] D. R. Agrawal *et al.*, "Conformal phased surfaces for wireless powering of bioelectronic microdevices," *Nat. Biomed. Eng.*, vol. 1, 2017, doi: 10.1038/s41551-017-0043.

[49] C. A. Rosen, K. A. Fish, and H. C. Rothenberg, "Electromechanical transducer," 1958

[50] S. Ozeri and D. Shmilovitz, "Ultrasonic transcutaneous energy transfer for powering implanted devices," *Ultrasonics*, vol. 50, no. 6, pp. 556–566, 2010, doi: 10.1016/j.ultras.2009.11.004.

[51] F. Mazzilli, C. Lafon, and C. Dehollain, "A 10.5 cm ultrasound link for deep implanted medical devices," *IEEE Trans. Biomed. Circuits Syst.*, vol. 8, no. 5, pp. 738–750, 2014, doi: 10.1109/TBCAS.2013.2295403.

[52] Z. Kashani, S. J. Ilham, and M. Kiani, "Design and Optimization of Ultrasonic Links With Phased Arrays for Wireless Power Transmission to Biomedical Implants," *IEEE Trans. Biomed. Circuits Syst.*, vol. 16, no. 1, pp. 64–78, Feb. 2022, doi: 10.1109/TBCAS.2022.3140591.

[53] US Food and Drug Administration, "Information for Manufacturers Seeking Marketing Clearance of Diagnostic Ultrasound Systems and Transducers." Rockville, MD: US Food and Drug Administration, 1997.

[54] O. G. M. S. Grimnes, *Bioimpedance and Bioelectricity Basics*, 3rd ed. Academic, 2015.

[55] K. A. Sluka and D. Walsh, "Transcutaneous electrical nerve stimulation: Basic science mechanisms and clinical effectiveness," *J. Pain*, vol. 4, no. 3, pp. 109–121, 2003, doi: 10.1054/jpai.2003.434.

[56] N. Shields, J. Gormley, and N. O'Hare, "Short-wave diathermy: current clinical and safety practices.," *Physiother. Res. Int. J. Res. Clin. Phys. Ther.*, vol. 7, no. 4, pp. 191–202, 2002.

[57] M. Seyedi, B. Kibret, D. T. H. Lai, and M. Faulkner, "A survey on intrabody communications for body area network applications," *IEEE Trans. Biomed. Eng.*, 2013, doi: 10.1109/TBME.2013.2254714.

[58] W. J. Tomlinson, S. Banou, S. Blechinger-Slocum, C. Yu, and K. R. Chowdhury, "Body-guided galvanic coupling communication for secure biometric data," *IEEE Trans. Wirel. Commun.*, vol. 18, no. 8, pp. 4143–4156, 2019, doi: 10.1109/TWC.2019.2921964.

[59] D. P. Lindsey, E. L. McKee, M. L. Hull, and S. M. Howell, "A new technique for transmission of signals from implantable transducers," *IEEE Trans. Biomed. Eng.*, vol. 45, no. 5, pp. 605–613, 1998, doi: 10.1109/10.668751.

[60] T. Zhide *et al.*, "Transcutaneous battery recharging by volume conduction and its circuit modeling," *Annu. Int. Conf. IEEE Eng. Med. Biol. - Proc.*, vol. C, pp. 644–647, 2006, doi: 10.1109/IEMBS.2006.259702.

[61] A. M. Sodagar and P. Amiri, "Capacitive coupling for power and data telemetry to implantable biomedical microsystems," *2009 4th Int. IEEEEMBS Conf. Neural Eng. NER 09*, pp. 411–414, 2009, doi: 10.1109/NER.2009.5109320.

[62] A. Ivorra, "Remote electrical stimulation by means of implanted rectifiers," *PLoS ONE*, 2011, doi: 10.1371/journal.pone.0023456.

[63] A. Ivorra Cano, J. Sacristán, and A. Baldi, "Injectable rectifiers as microdevices for remote electrical stimulation: an alternative to inductive coupling," 2013, doi: 10.1007/978-3-642-29305-4_415.

[64] A. García-Moreno, A. Comerma-Montells, M. Tudela-Pi, J. Minguillon, L. Becerra-Fajardo, and A. Ivorra, "Wireless networks of injectable microelectronic stimulators based on rectification of volume conducted high frequency currents." bioRxiv, p. 2022.03.11.483920, Mar. 14, 2022. doi: 10.1101/2022.03.11.483920.

[65] P. Chen, H. Yang, R. Luo, and B. Zhao, "A Tissue-Channel Transcutaneous Power Transfer Technique for Implantable Devices," *IEEE Trans. Power Electron.*, vol. 33, no. 11, pp. 9753–9761, 2018, doi: 10.1109/TPEL.2018.2791966.

[66] R. Jegadeesan, K. Agarwal, Y. X. Guo, S. C. Yen, and N. V. Thakor, "Wireless Power Delivery to Flexible Subcutaneous Implants Using Capacitive Coupling," *IEEE Trans. Microw. Theory Tech.*, vol. 65, no. 1, pp. 280–292, 2017, doi: 10.1109/TMTT.2016.2615623.

[67] A. Ivorra and L. Becerra-Fajardo, "Wireless Microstimulators Based on Electronic Rectification of Epidermically Applied Currents: Safety and Portability Analysis," in *18th IFESS Annual Conference*, 2013, pp. 213–216.

[68] L. Becerra-Fajardo and A. Ivorra, "*In vivo* demonstration of addressable microstimulators powered by rectification of epidermically applied currents for miniaturized neuroprostheses," *PLoS ONE*, 2015, doi: 10.1371/journal.pone.0131666.

[69] A. Ivorra, L. Becerra-Fajardo, and Q. Castellví, "*In vivo* demonstration of injectable microstimulators based on charge-balanced rectification of epidermically applied currents," *J. Neural Eng.*, vol. 12, no. 6, 2015, doi: 10.1088/1741-2560/12/6/066010.

[70] L. Becerra-Fajardo *et al.*, "Floating EMG sensors and stimulators wirelessly powered and operated by volume conduction for networked neuroprosthetics," *J. NeuroEngineering Rehabil.*, vol. 19, no. 1, p. 57, Jun. 2022, doi: 10.1186/s12984-022-01033-3.

[71] M. Tudela-Pi, L. Becerra-Fajardo, and A. Ivorra, "Powering Implants by Galvanic Coupling: A Validated Analytical Model Predicts Powers Above 1 mW in Injectable Implants," *IFMBE Proc.*, vol. 68, no. 3, 2019, doi: 10.1007/978-981-10-9023-3_5.

[72] R. Sedehi *et al.*, "A Wireless Power Method for Deeply Implanted Biomedical Devices via Capacitively Coupled Conductive Power Transfer," *IEEE Trans. Power Electron.*, vol. 36, no. 2, pp. 1870–1882, 2021, doi: 10.1109/TPEL.2020.3009048.

[73] B. C. Johnson *et al.*, "StimDust: A 6.5mm3, wireless ultrasonic peripheral nerve stimulator with 82% peak chip efficiency," 2018. doi: 10.1109/CICC.2018.8357047.

[74] J. S. Ho *et al.*, "Wireless power transfer to deep-tissue microimplants.," *Proc. Natl. Acad. Sci. U. S. A.*, vol. 111, no. 22, pp. 7974–9, 2014, doi: 10.1073/pnas.1403002111.

[75] A. Basir and H. Yoo, "Efficient Wireless Power Transfer System With a Miniaturized Quad-Band Implantable Antenna for Deep-Body Multitasking Implants," *IEEE Trans. Microw. Theory Tech.*, vol. 68, no. 5, pp. 1943–1953, May 2020, doi: 10.1109/TMTT.2020.2965938.

[76] D. K. Freeman *et al.*, "A sub-millimeter, inductively powered neural stimulator," *Front. Neurosci.*, vol. 11, no. NOV, pp. 1–12, 2017, doi: 10.3389/fnins.2017.00659.

[77] G. Jiang and D. D. Zhou, "Technology Advances and Challenges in Hermetic Packaging for Implantable Medical Devices," in *Implantable Neural Prostheses 2: Techniques and Engineering Approaches*, D. Zhou and E. Greenbaum, Eds. New York, NY: Springer, 2010, pp. 27–61. doi: 10.1007/978-0-387-98120-8_2.

[78] Y.-H. Joung, “Development of implantable medical devices: from an engineering perspective,” *Int. Neurourol. J.*, vol. 17, no. 3, pp. 98–106, Sep. 2013, doi: 10.5213/inj.2013.17.3.98.

[79] International Commission on Non-Ionizing Radiation Protection, “Guidelines for limiting exposure to electromagnetic fields (100 kHz to 300 GHz),” *Health Phys.*, vol. 118, no. 5, pp. 483–524, 2020, doi: 10.1097/HP.0000000000001210.

[80] WHO, “WHO Workshop 2002: Adverse temperature levels in humans,” *Int. J. Hyperthermia*, vol. 19, pp. 215–390, 2003.

[81] R. Narayanamoorthi, A. V. Juliet, C. Bharatiraja, S. Padmanaban, and Z. M. Leonowicz, “Class E power amplifier design and optimization for the capacitive coupled wireless power transfer system in biomedical implants,” *Energies*, vol. 10, no. 9, 2017, doi: 10.3390/en10091409.

[82] R. Erfani, F. Marefat, A. M. Sodagar, and P. Mohseni, “Transcutaneous capacitive wireless power transfer (C-WPT) for biomedical implants,” *Proc. - IEEE Int. Symp. Circuits Syst.*, pp. 4–7, 2017, doi: 10.1109/ISCAS.2017.8050940.

[83] R. Erfani, F. Marefat, A. M. Sodagar, and P. Mohseni, “Modeling and Experimental Validation of a Capacitive Link for Wireless Power Transfer to Biomedical Implants,” *IEEE Trans. Circuits Syst. II Express Briefs*, vol. 65, no. 7, pp. 923–927, 2018, doi: 10.1109/TCSII.2017.2737140.

[84] M. S. Wegmueller, M. Oberle, N. Felber, N. Kuster, and W. Fichtner, “Signal Transmission by Galvanic Coupling Through the Human Body,” *IEEE Trans. Instrum. Meas.*, vol. 59, no. 4, pp. 963–969, 2010.

[85] Y. Song, Q. Hao, K. Zhang, M. Wang, Y. Chu, and B. Kang, “The simulation method of the galvanic coupling intrabody communication with different signal transmission paths,” *IEEE Trans. Instrum. Meas.*, vol. 60, no. 4, pp. 1257–1266, 2011, doi: 10.1109/TIM.2010.2087870.

[86] M. Swaminathan, F. S. Cabrera, J. S. Pujol, U. Muncuk, G. Schirner, and K. R. Chowdhury, “Multi-Path Model and Sensitivity Analysis for Galvanic Coupled Intra-Body Communication Through Layered Tissue,” *IEEE Trans. Biomed. Circuits Syst.*, vol. 10, no. 2, pp. 339–351, 2016, doi: 10.1109/TBCAS.2015.2412548.

[87] D. Farina, L. Mesin, S. Martina, and R. Merletti, “A Surface EMG Generation Model with Multilayer Cylindrical Description of the Volume Conductor,” *IEEE Trans. Biomed. Eng.*, vol. 51, no. 3, pp. 415–426, 2004, doi: 10.1109/TBME.2003.820998.

[88] A. K. Teshome, B. Kibret, and D. T. H. Lai, “Galvanically Coupled Intrabody Communications for Medical Implants: A Unified Analytic Model,” *IEEE Trans. Antennas Propag.*, vol. 64, no. 7, pp. 2989–3002, 2016, doi: 10.1109/TAP.2016.2559519.

[89] S. H. Pun, Y. M. Gao, P. Mak, M. I. Vai, and M. Du, “Quasi-static modeling of human limb for intra-body communications with experiments,” *IEEE Trans. Inf. Technol. Biomed.*, vol. 15, no. 6, pp. 870–876, 2011, doi: 10.1109/TITB.2011.2161093.

[90] J. A. Ruiz, J. Xu, and S. Shimamoto, “Propagation characteristics of intra-body communications for body area networks,” *2006 3rd IEEE Consum. Commun. Netw. Conf. CCNC 2006*, vol. 1, pp. 509–513, 2006, doi: 10.1109/CCNC.2006.1593076.

[91] M. A. Callejon, J. Reina-Tosina, D. Naranjo-Hernandez, and L. M. Roa, “Galvanic coupling transmission in intrabody communication: A finite element approach,” *IEEE Trans. Biomed. Eng.*, vol. 61, no. 3, pp. 775–783, 2014, doi: 10.1109/TBME.2013.2289946.

[92] M. A. Callejon, L. Fernandez-Jimenez, J. Reina-Tosina, and L. M. Roa, “Galvanic intrabody communication for brain stimulation: A finite-element simulation study,” *2017 IEEE MTT- Int. Conf. Numer. Electromagn. Multiphysics Model. Optim. RF Microw. Terahertz Appl. NEMO 2017*, pp. 19–21, 2017, doi: 10.1109/NEMO.2017.7964173.

[93] J. P. Reilly, “Impedance and Current Distribution,” in *Applied Bioelectricity: from Electrical Stimulation to Electropathology*, New York: Springer-Verlag, 1998, pp. 12–68. doi: 10.1007/978-1-4612-1664-3_1.

[94] D. Andreuccetti, R. Fossi, and C. Petrucci, “An Internet resource for the calculation of the dielectric properties of body tissues in the frequency range 10 Hz - 100 GHz,” *IFAC-CNR, Florence (Italy)*, 1997.

[95] S. Grimnes and Ø. G. Martinsen, “Passive Tissue Electrical Properties,” in *Bioimpedance and Bioelectricity Basics*, 3 rd., Elsevier Ltd, 2015, pp. 77–118. doi: 10.1016/B978-0-12-374004-5.X0001-3.

[96] K. R. Foster and R. P. Schwan, “Dielectric properties of tissue,” in *CRC Handbook of Biological Effects of Electromagnetic Fields*, C. Polk and E. Postow, Eds. FL: Boca Raton: CRC Press, 1996, pp. 25–102.

[97] A. Vander Vorst, A. Rosen, and Y. Kotsuka, *RF/Microwave Interaction with Biological Tissues*. New Jersey: John Wiley & Sons, Inc., 2006, p. 44.

[98] S. Grimnes and Ø. G. Martinsen, “Electrolytics,” in *Bioimpedance and Bioelectricity Basics*, 3rd ed., Elsevier Ltd, 2015, pp. 9–36.

[99] S. R. Ward and R. L. Lieber, “Density and hydration of fresh and fixed human skeletal muscle,” *J. Biomech.*, vol. 38, no. 11, pp. 2317–2320, Nov. 2005, doi: http://dx.doi.org/10.1016/j.jbiomech.2004.10.001.

[100] D. J. Griffiths, “Special Techniques,” in *Introduction to Electrodynamics*, 3rd editio., Upper Saddle River: Prentice Hall, 1999, pp. 119–153.

[101] S. Grimnes and Ø. G. Martinsen, “Geometrical Analysis,” in *Bioimpedance and Bioelectricity Basics*, 3rd ed., Elsevier Ltd, 2015, pp. 141–178.

[102] T. Ohira, “Power efficiency and optimum load formulas on RF rectifiers featuring flow-angle equations,” *IEICE Electron. Express*, vol. 10, no. 11, pp. 1–9, 2013, doi: 10.1587/elex.10.20130230.

[103] L. Becerra-Fajardo, M. Schmidbauer, and A. Ivorra, “Demonstration of 2 mm Thick Microcontrolled Injectable Stimulators Based on Rectification of High Frequency Current Bursts,” *IEEE Trans. Neural Syst. Rehabil. Eng.*, vol. 25, no. 8, pp. 1343–1352, 2017, doi: 10.1109/TNSRE.2016.2623483.

[104] L. Becerra-Fajardo, R. Garcia-Arnau, and A. Ivorra, “Injectable Stimulators Based on Rectification of High Frequency Current Bursts: Power Efficiency of 2, mm Thick Prototypes,” *Converging Clin. Eng. Res. Neurorehabilitation II Springer Cham*, pp. 667–671, 2017, doi: 10.1007/978-3-319-46669-9_110.

[105] A. D. Dehennis, M. Mailand, D. Grice, S. Getzlaff, and A. E. Colvin, "A near-field-communication (NFC) enabled wireless fluorimeter for fully implantable biosensing applications," 2013. doi: 10.1109/ISSCC.2013.6487743.

[106] K. Birmingham *et al.*, "Bioelectronic medicines: A research roadmap," *Nat. Rev. Drug Discov.*, vol. 13, no. 6, pp. 399–400, 2014, doi: 10.1038/nrd4351.

[107] J. Andreu-Perez, D. R. Leff, H. M. D. Ip, and G. Z. Yang, "From Wearable Sensors to Smart Implants-Toward Pervasive and Personalized Healthcare," *IEEE Trans. Biomed. Eng.*, vol. 62, no. 12, pp. 2750–2762, 2015, doi: 10.1109/TBME.2015.2422751.

[108] A. Vander Vorst, A. Rosen, and Y. Kotsuka, *RF/Microwave Interaction with Biological Tissues*. New Jersey: John Wiley & Sons, Inc., 2006.

[109] M. S. Wegmueller *et al.*, "An Attempt to Model the Human Body as a Communication Channel," *IEEE Trans. Biomed. Eng.*, vol. 54, no. 11, pp. 2057–2063, 2007, doi: 10.1109/TBME.2007.895111.

[110] B. Kibret, M. H. Seyedi, D. T. H. Lai, and M. Faulkner, "Investigation of galvanic-coupled intrabody communication using the human body circuit model," *IEEE J. Biomed. Health Inform.*, vol. 18, no. 4, pp. 1196–1206, 2014, doi: 10.1109/JBHI.2014.2301165.

[111] P. Hasgall *et al.*, "IT'IS Database for thermal and electromagnetic parameters of biological tissues, Version 4.0," *IT'IS*, 2018.

[112] M. Brian S., *An introduction to materials engineering and science for chemical and materials engineers*. 2004. doi: 10.5860/choice.41-5327.

[113] L. Becerra-Fajardo, M. Tudela-Pi, and A. Ivorra, "Two-Port Networks to Model Galvanic Coupling for Intrabody Communications and Power Transfer to Implants," *2018 IEEE Biomed. Circuits Syst. Conf. BioCAS*, pp. 1–4, 2018, doi: 10.1109/BIOCAS.2018.8584691.

[114] W. H. Hayt, J. Kemmerly, and S. M. Durbin, "Two-port networks," in *Engineering Circuit Analysis*, 8th ed., New York: McGraw-Hill, 2012, pp. 687–732.

[115] IEC/IEEE International, "Determining the peak spatial-average specific absorption rate (SAR) in the human body from wireless communications devices, 30 MHz to 6 GHz - Part 1: General requirements for using the finite-difference time-domain (FDTD) method for SAR calculations," *IECIEEE 62704-1*, pp. 1–86, 2017, doi: 10.1109/IEEESTD.2017.8088404.

[116] M. Tudela-Pi, L. Becerra-Fajardo, A. Garcia-Moreno, J. Minguillon, and A. Ivorra, "Power Transfer by Volume Conduction: *In Vitro* Validated Analytical Models Predict DC Powers above 1 mW in Injectable Implants," *IEEE Access*, 2020, doi: 10.1109/ACCESS.2020.2975597.

[117] J. Minguillon *et al.*, "Powering electronic implants by high frequency volume conduction: in human validation," *bioRxiv*, p. 2021.03.15.435404, Jan. 2021, doi: 10.1101/2021.03.15.435404.

[118] H. Kanehisa, M. Miyatani, K. Azuma, S. Kuno, and T. Fukunaga, "Influences of age and sex on abdominal muscle and subcutaneous fat thickness," *Eur. J. Appl. Physiol.*, 2004, doi: 10.1007/s00421-003-1034-9.

[119] W. Murphy, J. Black, and G. Hastings, *Handbook of biomaterial properties*, 2 nd. New York: Springer Science, 2016. doi: 10.1007/978-1-4939-3305-1.

[120] W. M. Grill and J. Thomas Mortimer, "Electrical properties of implant encapsulation tissue," *Ann. Biomed. Eng.*, 1994, doi: 10.1007/BF02368219.

[121] N. Benítez Brito *et al.*, "Relationship between mid-upper arm circumference and body mass index in inpatients," *PLoS ONE*, 2016, doi: 10.1371/journal.pone.0160480.

[122] J. S. Ho *et al.*, "Wireless power transfer to deep-tissue microimplants.," *Proc. Natl. Acad. Sci. U. S. A.*, 2014, doi: 10.1073/pnas.1403002111.

[123] IEEE International Committee on Electromagnetic Safety, "IEEE Standard for Safety Levels with Respect to Human Exposure to Radio Frequency Electromagnetic Fields , 3 kHz to 300 GHz," *Inc N. Y. NY*, 2006, doi: 10.1109/IEEESTD.2006.99501.

[124] M. M. Lowery, R. F. F. Weir, and T. A. Kuiken, "Simulation of intramuscular EMG signals detected using implantable myoelectric

sensors (IMES)," *IEEE Trans. Biomed. Eng.*, 2006, doi: 10.1109/TBME.2006.881774.

[125] F. Suska, L. Emanuelsson, A. Johansson, P. Tengvall, and P. Thomsen, "Fibrous capsule formation around titanium and copper," *J. Biomed. Mater. Res. - Part A*, 2008, doi: 10.1002/jbm.a.31575.

[126] A. Ivorra, L. Becerra-Fajardo, and Q. Castellví, "*In vivo* demonstration of injectable microstimulators based on charge-balanced rectification of epidermically applied currents," *J. Neural Eng.*, vol. 12, no. 6, 2015, doi: 10.1088/1741-2560/12/6/066010.

[127] W. J. Zhang and C. A. van Luttervelt, "Toward a resilient manufacturing system," *CIRP Ann.*, vol. 60, no. 1, pp. 469–472, 2011, doi: https://doi.org/10.1016/j.cirp.2011.03.041.

[128] K. Zhang *et al.*, "Near-Field Wireless Power Transfer to Deep-Tissue Implants for Biomedical Applications," *IEEE Trans. Antennas Propag.*, vol. 68, no. 2, pp. 1098–1106, 2020, doi: 10.1109/TAP.2019.2943424.

[129] M. Zada and H. Yoo, "A Miniaturized Triple-Band Implantable Antenna System for Bio-Telemetry Applications," *IEEE Trans. Antennas Propag.*, vol. 66, no. 12, pp. 7378–7382, 2018, doi: 10.1109/TAP.2018.2874681.

[130] M. Meng and M. Kiani, "Design and Optimization of Ultrasonic Wireless Power Transmission Links for Millimeter-Sized Biomedical Implants," *IEEE Trans. Biomed. Circuits Syst.*, vol. 11, no. 1, pp. 98–107, 2017, doi: 10.1109/TBCAS.2016.2583783.

[131] I. of Electrical and E. Engineers, *IEEE Std C95.1™-2019: IEEE Standard for Safety Levels with Respect to Human Exposure to Electric, Magnetic, and Electromagnetic Fields, 0 Hz to 300 GHz*. Institute of Electrical and Electronics Engineers, 2019. doi: 10.1109/IEEESTD.2019.8859679.

[132] Bureau Radiocommunication - International Telecommunication Union, "Radio Regulations Articles Edition of 2020," 2020.

[133] D. J. Weber *et al.*, "BIONic WalkAide for correcting foot drop," *IEEE Trans. Neural Syst. Rehabil. Eng.*, vol. 13, no. 2, pp. 242–246, 2005, doi: 10.1109/TNSRE.2005.847385.

[134] J. Ausra *et al.*, "Wireless battery free fully implantable multimodal recording and neuromodulation tools for songbirds," *Nat. Commun.*, vol. 12, no. 1968, pp. 1–12, 2021, doi: 10.1038/s41467-021-22138-8.

[135] M. Tudela-Pi, J. Minguillon, L. Becerra-Fajardo, and A. Ivorra, "Volume Conduction for Powering Deeply Implanted Networks of Wireless Injectable Medical Devices: A Numerical Parametric Analysis," *IEEE Access*, vol. 9, pp. 100594–100605, 2021, doi: 10.1109/ACCESS.2021.3096729.

[136] M. Tudela-Pi, L. Becerra-Fajardo, A. Garcia-Moreno, J. Minguillon, and A. Ivorra, "Power Transfer by Volume Conduction: *In Vitro* Validated Analytical Models Predict DC Powers above 1 mW in Injectable Implants," *IEEE Access*, 2020, doi: 10.1109/ACCESS.2020.2975597.

[137] P. Hasgall *et al.*, "IT'IS Database for thermal and electromagnetic parameters of biological tissues, Version 4.0," *IT'IS*, 2018.

[138] J. Olivo, S. Carrara, and G. De Micheli, "Biofuel cells and inductive powering as energy harvesting techniques for implantable sensors," *Sci. Adv. Mater.*, vol. 3, no. 3, pp. 420–425, Jun. 2011, doi: 10.1166/sam.2011.1175.

[139] D. U. Furrer and S. L. Semiatin, Eds., "Physical Data on the Elements and Alloys," in *Fundamentals of Modeling for Metals Processing*, vol. 22A, ASM International, 2009, pp. 0–0. doi: 10.31399/asm.hb.v22a.a0005445.

[140] A. U. M, E. Anthony, and E. Godspower, "Electrical Properties of Enamel Wire Insulation," *Int. J. Trend Sci. Res. Dev.*, vol. Volume-3, no. Issue-2, pp. 803–806, 2019, doi: 10.31142/ijtsrd21450.

[141] S. Banou *et al.*, "Beamforming Galvanic Coupling Signals for IoMT Implant-to-Relay Communication," *IEEE Sens. J.*, vol. 19, no. 19, pp. 8487–8501, 2019, doi: 10.1109/JSEN.2018.2886561.

[142] A. K. Teshome, B. Kibret, and D. T. H. Lai, "A Review of Implant Communication Technology in WBAN: Progress and Challenges," *IEEE Rev. Biomed. Eng.*, vol. 12, pp. 88–99, 2018, doi: 10.1109/RBME.2018.2848228.

[143] M. J. Karimi, A. Schmid, and C. Dehollain, “Wireless Power and Data Transmission for Implanted Devices via Inductive Links: A Systematic Review,” *IEEE Sens. J.*, vol. 21, no. 6, pp. 7145–7161, 2021, doi: 10.1109/JSEN.2021.3049918.

[144] M. Ghovanloo and K. Najafi, “A wideband frequency-shift keying wireless link for inductively powered biomedical implants,” *IEEE Trans. Circuits Syst. Regul. Pap.*, vol. 51, no. 12, pp. 2374–2383, 2004, doi: 10.1109/TCSI.2004.838144.

[145] R. Jegadeesan, S. Nag, K. Agarwal, N. V. Thakor, and Y.-X. Guo, “Enabling Wireless Powering and Telemetry for Peripheral Nerve Implants,” *IEEE J. Biomed. Health Inform.*, vol. 19, no. 3, pp. 958–970, 2015, doi: 10.1109/JBHI.2015.2424985.

[146] K. Agarwal, N. V. Thakor, R. Jegadeesan, Y.-X. Guo, and N. V. Thakor, “Wireless Power Transfer Strategies for Implantable Bioelectronics.,” *IEEE Rev. Biomed. Eng.*, vol. 10, pp. 136–161, 2017, doi: 10.1109/RBME.2017.2683520.

[147] A. D. Rush and P. R. Troyk, “A Power and Data Link for a Wireless-Implanted Neural Recording System,” *IEEE Trans. Biomed. Eng.*, vol. 59, no. 11, pp. 3255–3262, 2012, doi: 10.1109/TBME.2012.2214385.

[148] G. Simard, M. Sawan, and D. Massicotte, “High-Speed OQPSK and Efficient Power Transfer Through Inductive Link for Biomedical Implants,” *IEEE Trans. Biomed. Circuits Syst.*, vol. 4, no. 3, pp. 192–200, 2010, doi: 10.1109/TBCAS.2009.2039212.

[149] R. Noormohammadi, A. Khaleghi, J. Bergsland, and I. Balasingham, “Conductive Backscatter Communication for Dual-Chamber Leadless Pacemakers,” *IEEE Trans. Microw. Theory Tech.*, vol. 70, no. 4, pp. 2442–2450, 2022, doi: 10.1109/TMTT.2022.3147978.

[150] M. A. Callejon, J. Reina-Tosina, D. Naranjo-Hernandez, and L. M. Roa, “Galvanic coupling transmission in intrabody communication: A finite element approach,” *IEEE Trans. Biomed. Eng.*, vol. 61, no. 3, pp. 775–783, 2014, doi: 10.1109/TBME.2013.2289946.

[151] M. Li *et al.*, "Comparable Investigation of Characteristics for I mplant Intra-Body Communication Based on Galvanic and Capacitive Coupling," *IEEE Trans. Biomed. Circuits Syst.*, vol. 13, no. 6, pp. 1747–1758, 2019, doi: 10.1109/TBCAS.2019.2940827.

[152] T. Handa, S. Shoji, S. Ike, S. Takeda, and T. Sekiguchi, "A very low-power consumption wireless ECG monitoring system using body as a signal transmission medium," in *Proceedings of International Solid State Sensors and Actuators Conference (Transducers '97)*, 1997, vol. 2, pp. 1003–1006 vol.2. doi: 10.1109/SENSOR.1997.635344.

[153] M. Amparo Callejón, D. Naranjo-Hernández, J. Reina-Tosina, and L. M. Roa, "Distributed circuit modeling of galvanic and capacitive coupling for intrabody communication," *IEEE Trans. Biomed. Eng.*, vol. 59, no. 12 PART2, pp. 3263–3269, 2012, doi: 10.1109/TBME.2012.2205382.

[154] A. Makdissi, K. Amara, and A. Ghildiyal, "System, methods and apparatus for waking an autonomous active implantable medical device communicating by pulses transmitted through the interstitial tissues of the body," US8923795B2, Dec. 30, 2014 Accessed: Jul. 12, 2022. [Online]. Available: https://patents.google.com/patent/US8923795/en

[155] L. Becerra-Fajardo and A. Ivorra, "Bidirectional communications in wireless microstimulators based on electronic rectification of epidermically applied currents," 2015. doi: 10.1109/NER.2015.7146680.

[156] J.-P. Niu and G. Y. Li, "An Overview on Backscatter Communications," *J. Commun. Inf. Netw.*, vol. 4, no. 2, pp. 1–14, 2019, doi: 10.23919/JCIN.2019.8917868.

[157] X. Li, C.-Y. Tsui, and W.-H. Ki, "A 13.56 MHz Wireless Power Transfer System With Reconfigurable Resonant Regulating Rectifier and Wireless Power Control for Implantable Medical Devices," *IEEE J. Solid-State Circuits*, vol. 50, no. 4, pp. 978–989, 2015, doi: 10.1109/JSSC.2014.2387832.

[158] A. Khaleghi, A. Hasanvand, and I. Balasingham, "Radio Frequency Backscatter Communication for High Data Rate Deep Implants," *IEEE Trans. Microw. Theory Tech.*, vol. 67, no. 3, pp. 1093–1106, 2019, doi: 10.1109/TMTT.2018.2886844.

[159] S. Mandal and R. Sarpeshkar, "Power-Efficient Impedance-Modulation Wireless Data Links for Biomedical Implants," *IEEE Trans. Biomed. Circuits Syst.*, vol. 2, no. 4, pp. 301–315, 2008, doi: 10.1109/TBCAS.2008.2005295.

[160] J. R. Barry, E. A. Lee, and D. G. Messerschmitt, "Stochastic Signal Processing," in *Digital Communication*, 3rd ed., vol. 1, New York: Springer Science, 2004, pp. 57–111.

[161] R. M. Gray and D. L. Neuhoff, "Quantization," *IEEE Trans. Inf. Theory*, vol. 44, no. 6, pp. 2325–2383, 1998, doi: 10.1109/18.720541.

[162] Smith, David R., "Digital Modulation Techniques," in *Digital Transmission Systems*, 3 rd., New York: Springer, 2004, pp. 363–436.

# List of publications

## International journal articles

1. **M. Tudela-Pi**, L. Becerra-Fajardo, A. García-Moreno, J. Minguillon and A. Ivorra, "Power Transfer by Volume Conduction: *In Vitro* Validated Analytical Models Predict DC Powers Above 1 mW in Injectable Implants," in IEEE Access, vol. 8, pp. 37808-37820, 2020.

2. S. Malik, Q. Castellví, L. Becerra-Fajardo, **M. Tudela-Pi**, A. García-Moreno, M. Shojaei Baghini, A. Ivorra, "Injectable Sensors Based on Passive Rectification of Volume-Conducted Currents," in IEEE Transactions on Biomedical Circuits and Systems, vol. 14, no. 4, pp. 867-878, Aug. 2020.

3. **M. Tudela-Pi,** J. Minguillon, L. Becerra-Fajardo and A. Ivorra, "Volume Conduction for Powering Deeply Implanted Networks of Wireless Injectable Medical Devices: A Numerical Parametric Analysis," in IEEE Access, vol. 9, pp. 100594-100605, 2021.

4. J. Minguillon, **M. Tudela-Pi**, L. Becerra-Fajardo, E. Perera-Bel, A. J. del-Ama, A. Gil-Aguado, A. Megía-García, A. García-Moreno, A. Ivorra, "Powering electronic implants by high frequency volume conduction: in human validation," in *bioRxiv*, 2021.03.15.435404, 2021 [under review]

5. L. Becerra-Fajardo, M.O. Krob, J. Minguillon, C. Rodrigues, C. Welsch, **M. Tudela-Pi**, A. Comerma, F.O. Barroso, A. Schneider, A. Ivorra, "Floating EMG sensors and stimulators wirelessly powered and operated by volume conduction for networked neuroprosthetics," in Journal of NeuroEngineering and Rehabilitation, vol. 19, no. 57 (2022).

6. A. García-Moreno, A. Comerma-Montells, **M. Tudela-Pi**, J. Minguillon, L. Becerra-Fajardo, A. Ivorra, “Wireless networks of injectable microelectronic stimulators based on rectification of volume conducted high frequency currents,” in ***bioRxiv*** 2022.03.11.483290, 2022, [under review].

7. **M. Tudela-Pi**, J. Minguillon, L. Becerra-Fajardo, A. García-Moreno, A. Comerma, N. Álvarez, A. Ivorra, “Force control using injectable microstimulators based on volume conduction: an *in vivo* study”, 2022, [under preparation].

## Conference proceeding

1. L. Becerra-Fajardo, **M. Tudela-Pi,** and A. Ivorra, "Two-Port Networks to Model Galvanic Coupling for Intrabody Communications and Power Transfer to Implants," 2018 IEEE Biomedical Circuits and Systems Conference (BioCAS), 2018, pp. 1-4.

2. **M. Tudela-Pi,** L. Becerra-Fajardo, A. Ivorra, “Analysis of volume conduction as a wireless power transfer method for millimetric active implantable medical devices,” 2019 International Conference on Electrical Bioimpedance (ICEBI), 2019.